



Review

A method to improve tracking and particle identification in TPCs and silicon detectors

Hans Bichsel*

Center for Experimental Nuclear Physics and Astrophysics, University of Washington, Box 354290, Seattle, WA 98195-4290, USA

Received 9 March 2006; received in revised form 13 March 2006; accepted 13 March 2006

Available online 7 April 2006

Abstract

The measurement of the ionization by charged particles in a medium (gas or condensed) together with the measurement of their momentum or energy is used for tracking the particles and to determine their identity. For tracking the lateral extent of the ionization cloud should be known. For tracking and for charged particle identification (PID), one must understand that energy loss of particles, ionization and detector output are related, but not identical. In this paper, I discuss the relevant physics processes involved in PID and tracking and the stochastic nature of the energy loss mechanism. These calculations can be made with analytic and Monte Carlo methods. The expression dE/dx should be abandoned; it is never relevant to the signals in a particle-by-particle analysis. Specific terms such as energy loss, energy deposition, ionization and pulse height should be used instead. It is important that an accurate data analysis requires attention to track segmentation. I will show that properties of straggling functions for gases and thin silicon detectors are similar for equivalent absorber thicknesses and general conclusions given for one absorber will be valid for others. Thus, these techniques can be used in Time Projection Chambers (TPCs) and Silicon Drift Detectors. I will show how to use this formalism in the STAR and ALICE TPCs and describe how its use has improved the performance of the detector.

© 2006 Elsevier B.V. All rights reserved.

PACS: 02.70.Uu; 06.20.fb; 07.05.Kf; 07.77.-n; 34.50.Bw

Keywords: Energy loss; Ionization; Particle identification; Tracking

Contents

1. Introduction	158
1.1. General concepts	158
1.2. Interaction of radiation with matter	159
1.3. Straggling functions and particle identification	160
1.4. Measurements with time projection chambers	160
2. Models of collision cross-sections (CCS)	161
2.1. Rutherford cross-section $\sigma_R(E; \beta)$ and modifications	161
2.2. Bethe–Fano (B–F) cross-section	161
2.3. Fermi virtual photon (FVP) cross-section	162
2.4. Calculation and comparison of cross-sections	162

*Tel.: +1 206 329 2792; fax: +1 206 685 4634.

E-mail address: bichsel@npl.washington.edu.

3. Integral functions of collision cross-sections (CCS)	164
3.1. Total cross-sections and mean free paths	164
3.2. Cumulative probability density function $\Phi(E)$	164
3.3. Moments of collision cross-sections, stopping power and sum rules	165
4. Calculation of straggling (“Landau”) functions	166
4.1. Poisson distribution	166
4.2. Energy loss spectra for multiple collisions.	166
4.3. Analytic calculation of straggling functions $f(\Delta; x, \beta\gamma)$ for segments	166
4.4. Monte Carlo calculation of straggling functions	167
4.5. Landau–Vavilov calculation of straggling functions and modifications	167
5. Examples of straggling functions for segments	168
5.1. Properties of straggling functions.	168
5.2. Cumulative straggling functions $F(\Delta; x, \beta\gamma)$	169
6. Straggling functions for particle tracks.	170
6.1. Calculations of specific energy losses Δ/x and descriptors C for tracks	170
6.2. Dependence of truncated mean values on track lengths and number of segments.	171
7. Dependences of Δ_p , $\langle C \rangle$, σ_t and w on $\beta\gamma$ and gas pressure	172
7.1. Landau and Bethe–Bloch functions	172
7.2. Bichsel functions	173
8. Scaling of straggling functions	173
8.1. One-parameter scaling	174
8.2. Two-parameter scaling for segments.	175
8.3. Two-parameter scaling for tracks.	176
8.4. Practical implementation.	177
9. Energy loss, energy deposition and ionization.	179
10. Conversion of ionization into pulse-height	181
11. Calibration and diagnostics of detectors.	181
12. Compounded spectra in TPC	182
13. Particle identification PID with TPC measurements	183
13.1. Principles.	183
13.2. Resolution, separation power and overlap	183
13.3. Particle identification	185
13.4. PID with cumulative straggling functions	185
13.5. Exclusive assignment of particle masses	186
14. Comparison of experiments and theory	186
14.1. Comparisons for segments	186
14.2. Comparisons for tracks.	188
15. Conclusions and recommendations	189
Acknowledgements.	189
Appendix A. Comparison of B–F and FVP theories	190
Appendix B. Comparisons of straggling functions for Ar and P10	190
Appendix C. Sources of optical absorption data for Ne, Ar, CH ₄ , P10 and solids	190
Appendix D. Corrections to calculations and data analysis	191
Appendix E. Electron ranges and energy deposition in Ar, P10 and Si	192
Appendix F. Collision cross-sections for electrons and heavy ions	193
Appendix G. Straggling functions for very thin absorbers	193
Appendix H. Gas multiplication	194
Appendix I. Bremsstrahlung	194
Appendix J. ALICE TPC Monte Carlo method	194
References	195

Nomenclature*List of abbreviations*

symbol Meaning

ADC Analog to Digital Converter

BB Bethe–Bloch

B–F Bethe–Fano algorithm

CCS Collision Cross Section

DOS Dipole Oscillator Strength

FWHM Full-Width-at-Half-Maximum

FVP Fermi Virtual Photon approximation

GOS Generalized Oscillator Strength

PAI Photo Absorption Ionization

pdf probability density function

PID “Particle IDentification”

P10 gas used in STAR TPC, 90% Ar, 10% methane

RMS “Root-Mean-Square” deviation

STAR Solenoidal Tracker at RHIC

SVT “Silicon Vertex Tracker”

TPC “Time Projection Chamber”

List of symbols. For locations: *E* = equation, *F* = figure, *S* = section, *T* = table.

Symbol	Location	Description
a, b	S8.2, E38	parameters for linear scaling
A	E1	atomic weight, g/mol
B	E43	magnetic field
c		speed of light
C	S1.1, 1.4, 6.1, 13, E28	a “track descriptor”
D	S1.1, 9	energy deposition in absorber
D	E42	“separation power”
dE/dx	S1.1, 3.3	Bethe stopping power (properly dT/dx)
dT/dx	S1.1	Bethe stopping power
e	E1	electron charge
E	S1.2	energy loss in a single collision
E_{\max}	S2.1	maximum energy loss in a single collision, $E_{\max} = 2mc^2\beta^2\gamma^2$
E_{\min}	E22	minimum energy loss in Bethe stopping power
E_I	S9	atomic ionization energy
$f(C)$	S1.1, 6.1	straggling function for track descriptor
$f(\Delta)$	F1, S1.1, E20	energy loss straggling function
$F(\Delta)$	E26, F13, 18, 19	cumulative of energy loss straggling function
$f(E, 0)$	E6	dipole oscillator strength DOS
$f(E, K)$	E3	generalized oscillator strength GOS, $f(E, K) = (E/Q)F(E, K)$
$F(E, K)$	E2	matrix element for energy transfer E with momentum change K
f_r	F21–23	truncation fraction
$g(D)$	S1.1, 9	straggling function for energy deposition D
$G(J)$	S1.1	straggling function for ionization J
$h(Q)$	S1.1, F54	pulse height or ADC function
I	E17, 22	logarithmic mean excitation energy of an absorber
J	S1.1, 9	number of ion pairs created by an energy deposition D in segment x
k_R	E1	coefficient for Rutherford cross-section $k_R = 2\pi e^4/mc^2 = 2.54955 \text{ eV cm}^2$
k	E1, 22	coefficient for collision cross-section $k = k_R N_a Z/(A\beta^2) = 153.45 \text{ keV cm}^2$
$L(\zeta)$	E29	likelihood function
m	E1	electron mass
M	S1.2	mass of particles heavier than e
m_c	E18, 20	average number of collisions in a segment x , $m_c = x\Sigma_t$
M_v	E13, 27, 32	moments of a distribution function
n	F3	actual number of collisions in a segment x by one particle
N	E8	number of atoms or molecules per unit volume
N_A	E1	Avogadro’s number = 6.022×10^{23} molecules/mole
n_s	S6.1	number of segments in a track
p	S1.2	momentum of a particle; also gas pressure
$P(n)$	E18	Poisson distribution

q	S2.1	$q = \hbar K$
Q	S2.2	$Q = K^2/2m$
Q	S1.1	ADC value corresponding to J (List of abbreviations and Figs. 18, 19)
r	TB	a ratio of two quantities
r_r	E21	a random number
r_s	E41	“resolution”
R	TE	range of electrons
R_y	F4	Rydberg constant, 13.6 eV
S		stopping power (equivalent to dE/dx)
S_0	E16	sum rule result
S_r	E14	restricted stopping power
t	S1.1	length of a track in gas or solid, $t = \sum x$
T	S1.4	kinetic energy of a particle with speed v
v	E2	speed of a particle
V	S1,9	volume of a “cell” for a segment
w	F1, 13, 15	FWHM of a straggling function
$W(T)$	S1.4, 9	average energy needed to produce one electron ion pair
x	S1.1	length of a segment along a track
y	E12	a parameter
z	E1	charge number of particle (mostly 1)
Z	E1	atomic number of atom or molecule
α	E7	fine structure constant
β	S1.1	v/c ; “speed of a particle”
$\gamma = 1/\sqrt{1 - \beta^2}$	S1.1	
δ	S9	delta ray = secondary electron
$\delta(\beta)$	E36	“density effect”
Δ	S1.1	energy loss by a fast particle in a segment of length x
Δ_p	F1	most probable energy loss for a straggling function $f(\Delta)$
Δ_ℓ, Δ_u	F13	values for FWHM of $f(\Delta)$: $f(\Delta_\ell) = f(\Delta_u) = 0.5f(\Delta_p)$
ε	E7	complex dielectric constant of absorber $\varepsilon = \varepsilon_1 + i\varepsilon_2$
ε'	E35, 37	minimum energy loss in Landau theory, $\cong E_{\min}$
λ	S1.2, E7, F7	mean free path between collisions
λ	E37	Landau parameter
$\phi(\lambda)$	S8	universal Landau function
$\Phi(E; v)$	S3.1, F6	collision cross-section cumulative in energy loss E
ρ	E12, 23	density of an absorber
σ	E5, 7, F5, 6, J.1	collision cross-section (CCS)
	E33, T8.2, F21–23	also RMS for tracks
σ_R	E1, F6	Rutherford (or Coulomb) collision cross-section
$\sigma(E; v)$	E5–7	collision cross-section differential in energy loss E for single collisions of a particle with speed v
σ_γ	E7	photo absorption cross-section for photon energy hf
$\Sigma_t(v)$	S1.2, E12, F24, 25, J.1	total collision cross-section per unit absorber length
Θ	E7	coefficient in FVP theory
ξ	E25, 35	parameter of Landau theory, $\xi = xk/\beta^2$
$\Upsilon(E)$	S3.2, F10	complementary function to $\Phi(E)$
ζ	E29	parameter for likelihood method

1. Introduction

1.1. General concepts

The concept dE/dx [1] representing the mean rate of energy loss in an absorber (Section 3.3) is used inappropriately in the description of the physics of most high energy particle detectors. Consider Fig. 1 which gives the probability density function (pdf) $f(\Delta)$ for energy losses Δ of particles¹ with $\beta\gamma = 3.6$ traversing $x = 12$ mm of Ar gas. The most probable energy loss Δ_p and the width w of $f(\Delta)$ are more representative of $f(\Delta)$ than the mean energy loss $\langle\Delta\rangle = x dE/dx$. Details are given in Section 5.1, in particular it will be seen that Δ_p/x depends on x . Correspondingly, the energy loss quantities ($\langle C$) and σ) per unit length derived for tracks depend on track length (see Table 5).

The functions $f(\Delta)$ customarily are called “straggling functions” [4] or straggling spectra, except in high energy physics where they are called “Landau functions” in a generic sense. Here, “Landau function” is used only to designate the function described in Ref. [2] and shown in Fig. 1 by the dotted line. For very thin absorbers the energy loss spectra are more complex. An example for particles with $\beta\gamma = 2.1$ traversing $x = 1 \mu\text{m}$ of Si is given in Fig. 2 (also see Appendix G). Such spectra have been described earlier [5] and have been measured [6]. Structures of this type are also observed in measurements of straggling effects on resonant yields of nuclear reactions, called the “Lewis effect” [7].

This study describes the theory of the electronic interactions of fast charged particles with matter. Collision and energy loss cross-sections are derived and straggling functions and their properties are calculated. The use of these functions for tracking and for particle identification (PID) in time projection chambers, TPC, or silicon vertex trackers, SVT, is described. The aim is to achieve an uncertainty of 1% or less in the calculations.

The trajectory of a fast particle through an absorber is called a track with length t . It is subdivided into segments of length x . One method of PID consists of measuring the ionization by a particle in several thin detectors and either its energy [8,9] or its momentum [10,11]. Much of the past work on PID [12,13] has been based on empirical information without consideration of problems that will be described here.

Various analytic expressions have been used to describe and correlate experimental data. In particular, straggling functions have been approximated by Gaussians, and mean values and variances of straggling functions have been used for the data analysis. Such data are given for calculated straggling functions in Sections 3–5. It will be seen that mean values and variances for segments of tracks should be

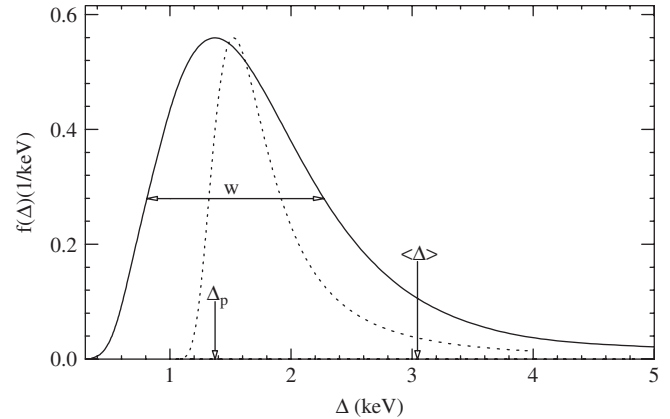


Fig. 1. The straggling function $f(\Delta)$ for particles with $\beta\gamma = 3.6$ traversing 1.2 cm of Ar gas is given by the solid line. It extends beyond $E_{\text{max}} \sim 2mc^2\beta^2\gamma^2 = 13$ MeV. The original Landau function [2,3] is given by the dotted line. Parameters describing $f(\Delta)$ are the most probable energy loss $\Delta_p(x; \beta\gamma)$, i.e. the position of the maximum of the straggling function, at 1371 eV, and the full-width-at-half-maximum (FWHM) $w(x; \beta\gamma) = 1463$ eV. The mean energy loss is $\langle\Delta\rangle = 3044$ eV.

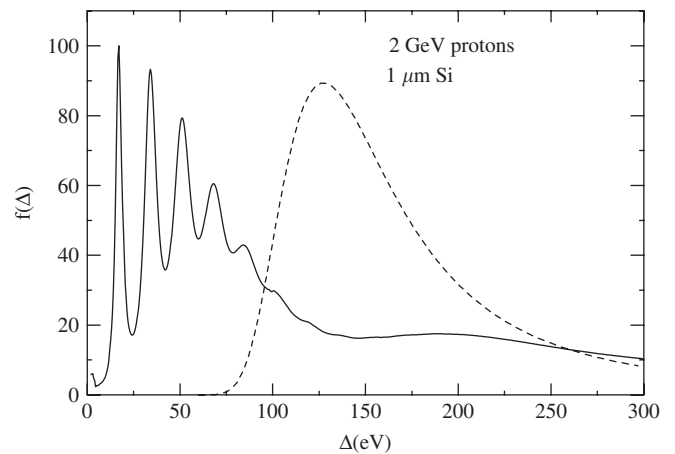


Fig. 2. Straggling in $1 \mu\text{m}$ of Si, compared to the Landau function. The Bethe–Bloch mean energy loss is $\langle\Delta\rangle = 400$ eV.

replaced by *most probable values* and *full-width-at-half-maximum* (FWHM).

The main concern here is with TPCs, but the term “detector” will be used to indicate that the principles described also apply to other systems, e.g. SVTs and thin absorbers in general. An extensive review of the use of Si detectors can be found in Ref. [14].

In any detector there are several stages which lead from the interactions of fast charged particles in the detector to a digital output signal used for tracking and PID [15]. The first stage is the energy loss Δ in segments due to the interactions of the particles with the matter in the detector. For small detector volumes, called pixels or cells [16], the next stage is the determination of the energy D deposited in the volume V under observation. The third stage is the conversion of D into ionization J which is defined as the

¹The charge of the particles is assumed to be $z = \pm 1e$ throughout and it is usually not included in the equations.

number of ion pairs produced.² In a TPC [11] the fourth stage is the transport of the electrons (as an “electron cloud” or an “electron cluster”) to the proportional counters located in the “end caps” [11]. The fifth stage is the amplification and collection of ions on “pads” (for the STAR TPC “inner” pads are 3×12 mm, “outer” are 4×20 mm in area) resulting in an analog electronic signal J' , and finally the conversion into a digital signal Q with an analog to digital converter (ADC). The processes occurring during these stages are discussed in Sections 9–11. For Si detectors corresponding details are described in Ref. [14].

In each stage the quantity from the previous stage is modified and we must determine this modification. For the stages from the traversal of a particle through the detector ending in the ADC output we must distinguish the following quantities. For track segments I am using symbols which have been defined in various publications:

- energy loss Δ and its pdf $f(\Delta)$ [17,18],
- energy deposition D with the pdf $g(D)$ [19,20],
- ionization J with the pdf $G(J)$ [16,21],
- transport of electrons to proportional counters [11] or amplifiers [14],
- proportional counter output J' with the pdf $H(J')$ [11],
- pulse-height or ADC output Q with the pdf $h(Q)$ [11,22].

For tracks, Section 6, the calculated truncated mean value of the energy losses per segment, Δ/x , is called C and modified quantities and pdfs for each stage corresponding to those for segments must be defined. Experimentally measured values are used with a suffix x .

In order to clearly understand the stages outlined above the replacement of the universal use of the expression “ dE/dx ” for *all* of the above quantities by the specific concepts Δ, D, J, J', Q and C defined here is proposed.³

The pdfs defined above will be calculated and described. It will be seen in Sections 9 and 10 that the differences between $f(\Delta)$, $g(D)$ and $G(J)$ for the STAR TPC are not large. In most reports so far they have been disregarded. For the ALICE TPC they are explored in Ref. [23].

This study is mainly about the calculation of the energy loss functions $f(\Delta)$ and $f(C)$ and their dependence on particle speed and absorber thickness, Sections 2–7. The functions for the other stages depend on the geometry of the elements of the TPC and are explored in less detail in Sections 9 and 10. It will be seen that the moments of $f(\Delta)$, e.g. *mean value* and *standard deviation*, are not appropriate for a description of the functions for segments, especially for thin absorbers. Instead, most probable energy loss Δ_p

and FWHM w should be used. Truncated mean values and standard deviations for tracks will be useful for some applications.

A brief description of the physics of the interactions of fast particles with matter is given in Section 1.2. A full theoretical foundation is given in Sections 2 and 3. The absorbers considered are Ne, Ar, P10 gas (a mixture of 10% CH₄ and 90% Ar) and Si. Calculations, measurements and applications given here are mainly for the STAR TPC. The concepts presented can readily be applied to most other detectors such as ALICE [23,24]. In order to approximate the gas mixture used in the ALICE TPC in 2005, (85% Ne, 10% CO₂, 5% N₂) a density $\rho = 0.91$ mg/cm³ is used for Ne. It is important to always be aware of the fundamental microscopic interaction processes which are described in Section 1.2.

Calculations of straggling functions are described in Sections 1.3 and 3–5. It will be shown that the parameters describing the straggling functions do not have simple relations to particle speed β , segment lengths x , and track lengths t . In particular, conclusions based on the central limit theorem are coarse approximations. Since the “resolution” for experimental data [25] can be as low as 2% or 3%, calculations should be made with an uncertainty of 1% or less. Therefore, few analytic functions can be given for results, and functions are presented in the form of tables and graphs [26]. Scaling procedures can greatly reduce the flood of calculated data (Section 8). For a detailed study of the measurements in a detector we must clearly distinguish measurements for single segments (pads, rows or pixels) and for tracks. Data about the lateral extent of tracks can be derived and may be needed for tracking measurements (Sections 3.2 and 9).

An introduction to the subject was given by Allison and Cobb [10]. An extensive review of “Particle Detection with Drift Chambers” has been written by Blum and Rolandi [16]. Calculated straggling functions for solid state detectors are compared with experimental data in Refs. [18,27]. Other aspects of the subject may be found in “Radiation Detection and Measurement” by Knoll [22]. A general survey of the “electronic” interactions of charged particles with matter including a derivation of the Bethe dE/dx can be found in Ref. [28].

1.2. Interaction of radiation with matter

The interactions of a fast charged particle with speed $\beta = v/c$ or momentum $p = Mc\beta\gamma$ can be described as the occurrence of random individual collisions in each of which the particle loses a random amount of energy E . The particle can be considered to produce a track in matter [28]. The average probability of collisions is given by the macroscopic (or total) collision cross-section $\Sigma_t(\beta\gamma)$, or, equivalently, by the mean free path $\lambda(\beta\gamma) = 1/\Sigma_t(\beta\gamma)$ between collisions. The pdf for single energy losses E is described by the differential collision spectrum $\sigma(E; \beta\gamma)$. These functions are discussed in Sections 2 and 3.

²“Ion pairs” is used generically to also mean electron hole pairs, scintillator photons etc.

³Other expressions currently in use in the high energy field should be replaced by words describing the specific process or observation made. Examples are the expressions “hit” which should be replaced by “segment,” or, to be more specific, “ionization in a segment,” or by “one collision of Au ions”; “event” which might be “collision of two heavy ions” (or whatever else it might be); “cluster,” footnote 40.

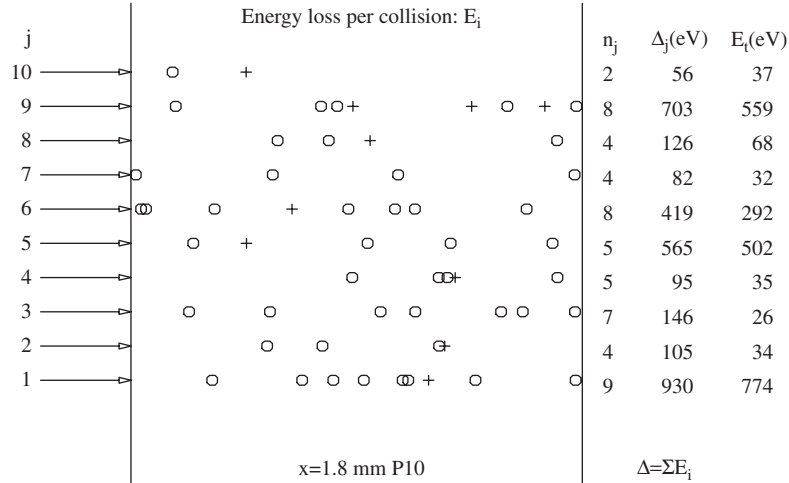


Fig. 3. Monte Carlo simulation of the passage of 10 particles (index j) with $\beta\gamma = 3.6$ through segments of P10 gas. The thickness of the gas layer (at 1 atm and 25 °C) is $x = 1.8$ mm. The direction of travel is given by the arrows. Inside the gas, the tracks are defined by the symbols showing the location of a collision. The mean free path between collisions is $\lambda = 0.3$ mm (see Fig. 7 or Table 2), thus the average number of collisions per track is six. At each collision point a random energy loss E_i is selected from the distribution function $\Phi(E; \beta\gamma)$, Fig. 9. Two symbols are used to represent energy losses: \circ for $E_i < 33$ eV, $+$ for $E_i > 33$ eV; the mean free path between collisions with $E_i > 33$ eV is 2 mm. Segment statistics are shown to the right: the total number of collisions for each track is given by n_j , with a nominal mean value $\langle n \rangle = x/\lambda = 6$ and the total energy loss is $\Delta_j = \sum E_i$, with the nominal mean value $\langle \Delta \rangle = x dE/dx = 440$ eV, where dE/dx is the Bethe–Bloch stopping power, M_1 in Table 2. The largest energy loss E_i on each track is also given. The mean value of the Δ_j is 325 ± 314 eV, much less than $\langle \Delta \rangle$. Note that the largest possible energy loss in a single collision is $E_{\max} = 13$ MeV, while the probability for $E > 50,000$ eV is 0.002 per cm, Eq. (12) or Figs. 9 and 10.

The energy loss interactions along a particle track can be simulated with a Monte Carlo calculation [26,29]; see Section 4.4. A simple picture of this process for short segments is shown in Fig. 3. The total energy loss in a segment j is $\Delta_j = \sum E_i$. Other details are given in the caption. All understanding of the rest of this paper follows from this model.

1.3. Straggling functions and particle identification

From theoretical simulations of the processes in the TPC we can obtain a better understanding of PID than from the data we can get from experimental measurements. Studies describing calculated straggling functions relevant to PID have been presented over several years by the author [30]. It is useful to understand that the width w of straggling functions is caused by two effects: the spread in the number of collisions appearing in the Poisson distribution described in Section 4.1 and the spread of the pdfs for multiple collisions described in Section 4.2. This distinction cannot be discerned in the Landau–Vavilov or the Bohr calculations.

Several methods to calculate straggling functions are described in Section 4, examples are given in Sections 5 and 6. The dependence of the properties of straggling functions on segment or track length and $\beta\gamma$ are given in Section 7. In Section 8 it will be shown that a two-parameter scaling procedure implicit in Landau’s formulation [5,17] is useful in reducing the amount of numerical calculation.

The calculations for tracks given here were obtained with Monte Carlo simulations [29] for individual tracks and the subsequent binning into distributions for many tracks. All

calculations in Sections 4–8 are made only for energy losses. The other stages from energy loss to final ADC output are considered in Sections 9 and 10. By comparing experimental functions to calculated ones it is possible to understand the operation and processes of the TPC and to diagnose errors in parameters currently used for the TPC, Section 11. As an introduction to PID spectra produced by different particles with the same momentum are shown in Section 12.

PID analysis is discussed in Section 13. The use of truncated mean values as “descriptors” C for track properties has certain advantages, but likelihood methods are also considered. The “resolution” in PID can be defined plausibly by “overlap numbers.” They depend strongly on the total length of the track measured, the number of segments in the tracks, the particle speed and the number of tracks for each particle type (Section 13.2). In this study it is suggested that the use of analytic approximation functions (e.g. Gaussians) be replaced by the use of tabulated straggling functions [26].

1.4. Measurements with time projection chambers

An example of experimental values C for individual tracks, each with momentum p , can be seen in Ref. [1, Fig. 28.5, p. 262] and in Ref. [11, Fig. 11, p. 676]. The sequence of experimental observations in a detector is outlined in Sections 1.1, 9, 10, Appendix D. It is assumed that $J = D/W(T)$, where $W(T)$ is the energy required to produce an ion pair by particles with kinetic energy T [31]. The output from the TPC is the pulse-height Q for

each segment. For Si a detailed description of these steps is given in Ref. [14].

For tracks the measured Q/x are combined into the descriptor quantity C (which, so far, usually is called dE/dx [11]), see Sections 6 and 13.1, and a experimental straggling function $f(C)$ for tracks is generated. Comparisons of experimental data with calculations are given in Section 14. The achievement of a 1% uncertainty of the calculations of Δ_p and C seems to be possible for TPCs as it has been for Si detectors [18]. A larger uncertainty of FWHM w should be expected due to the diffusion correction (Section 10). Methods for PID are described in Section 13.

2. Models of collision cross-sections (CCS)

The collision cross-sections (CCS) differential in energy loss give the probabilities for the energy losses in single collisions. A reliable calculation of CCS is needed to obtain straggling functions for thin or very thin absorbers used for PID (Figs. G.1 and G.2). Several models are given and their differences are assessed. The first one is the Rutherford cross-section, which is the cross-section for the collision of two free charged particles. It has been used extensively [17] (Appendix J). If charged particles collide with electrons *bound* in atoms, molecules or solids, the cross-section can be written as a modified Rutherford cross-section.

An approximate but plausible way of describing these interactions is to consider the emission of virtual photons by the fast particle, which then are absorbed by the material. Here this is called the Fermi virtual photon (FVP) method [32]. The differential CCS then is closely related to the photo absorption cross-section of the molecules. Bohr [33] described this as a “resonance” effect.

A more comprehensive approach is given by the Bethe–Fano (B–F) method [18,28,34]. These models are described here. Binary encounter methods have been used [35,36], but are not discussed. Comparison of the models are made in Section 2.4 and in Appendix A. Most of the calculations have been made with double precision arithmetic (i.e. 64 bits).

2.1. Rutherford cross-section $\sigma_R(E; \beta)$ and modifications

Much work on straggling functions has been based on the use of the Rutherford cross-section [4,17,33,37]; see Section 4.5. For the interaction of a particle with charge ze and speed $\beta = v/c$ colliding with an electron at rest it can be written in an approximation adequate for present purposes as Ref. [3]

$$\begin{aligned} \sigma_R(E; \beta) &= \frac{k_R}{\beta^2} \frac{(1 - \beta^2 E/E_{\max})}{E^2}, \\ k_R &= \frac{2\pi e^4}{mc^2} z^2 = 2.54955 \times 10^{-19} z^2 \text{ eV cm}^2, \\ k &= k_R \frac{N_A}{\beta^2} \frac{Z}{A} = 0.15354 \frac{Z}{A\beta^2} \text{ MeV cm}^2 \end{aligned} \quad (1)$$

where m is the mass of an electron, A the atomic mass of the absorber in g/mol and $E_{\max} \sim 2mc^2\beta^2\gamma^2$ is the maximum energy loss⁴ for heavy particles. For electrons a value $E_{\max} = T/2$ is usually used. Note that the mass of the particle does not appear in Eq. (1).

Various attempts have been made to take into account that electrons are bound in matter [18,27,41–43]. They are discussed briefly in Section 4.5. In the ALICE Technical Design Report of the TPC [23] the cross-section for a gas consisting of 90% Ne and 10% CO₂ is represented by Eq. (1) with a denominator $E^{2.2}$ instead of E^2 . Details about this method are given in Appendix J.

2.2. Bethe–Fano (B–F) cross-section

Bethe [44] derived an expression for a cross-section doubly differential in energy loss E and momentum transfer \mathbf{K} using the first Born approximation for inelastic scattering on free atoms. Fano [34] extended the method for solids. In its non-relativistic form it can be written as the Rutherford cross-section modified by the “inelastic form factor” [34,45]:

$$d\sigma(E, Q) = (k_R/\beta^2) |F(E, \mathbf{K})|^2 dQ/Q^2 \quad (2)$$

where $F(E, \mathbf{K})$ is the transition matrix element for the excitation and $Q = q^2/2m$, with $\mathbf{q} = \hbar\mathbf{K}$ the momentum transferred from the incident particle to the absorber. Usually, $F(E, \mathbf{K})$ is replaced by the generalized oscillator strength (GOS) $f(E, K)$ defined by

$$f(E, K) = \frac{E}{Q} |F(E, \mathbf{K})|^2. \quad (3)$$

An example of $f(E, K)$ is shown in Fig. 4. A full set of GOS for H-atoms can be seen in Ref. [45, Fig. 10]. Then we get

$$d\sigma(E, Q) = \sigma_R(E; v) E f(E, K) \frac{dQ}{Q}. \quad (4)$$

In the limit $K \rightarrow 0$, $f(E, K)$ becomes the optical dipole oscillator strength (DOS) $f(E, 0)$. Because of the $1/Q$ factor in Eq. (4), the values of the DOS are important for accurate cross-sections.

The cross-section differential in energy loss E is obtained by integrating Eq. (4) over Q ,

$$\sigma(E; v) = \sigma_R(E; v) \int_{Q_{\min}} E f(E, K) \frac{dQ}{Q} \quad (5)$$

with $Q_{\min} \sim E^2/2mv^2$ [45]. The dependence on particle speed v enters via Q_{\min} in addition to its appearance in $\sigma_R(E; v)$. In our current understanding, this approach to the calculation of $\sigma(E; v)$ is a close approximation to reality. The relativistic expression is described in Refs. [18,34]. A detailed study of $f(E, K)$ for all shells of solid silicon and aluminum has been made [18,46]. Checks have been made that $f(E, 0)$ agrees with optical data [18]. Here $\sigma(E; \beta)$

⁴The exact form of E_{\max} [1,38–40] is not important for the present application.

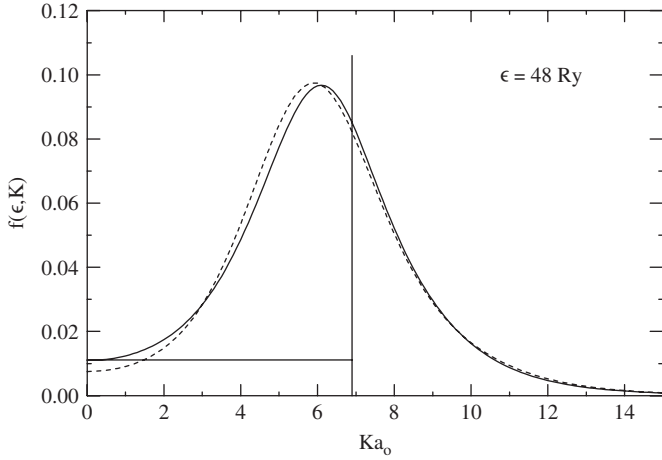


Fig. 4. Generalized oscillator strength (GOS) for Si for an energy transfer $\varepsilon = 48 \text{ Ry}$ ($\text{Ry} = 13.6 \text{ eV}$) to the 2p-shell electrons [18]. Solid line: calculated with Herman–Skilman potential, dashed line: hydrogenic approximation. The horizontal and vertical line define the FVP approximation (Section 2.3).

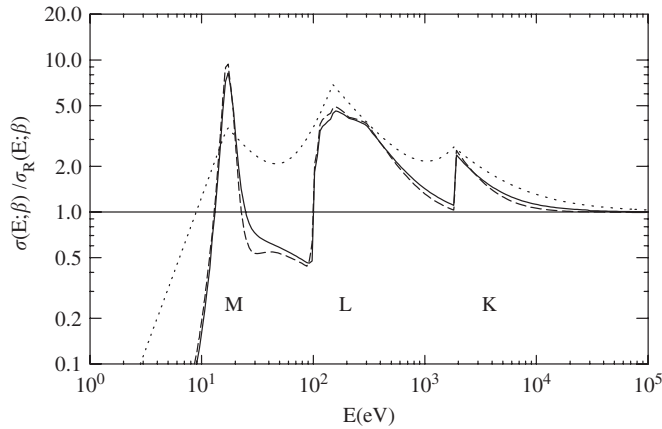


Fig. 5. Inelastic collision cross-sections $\sigma(E; \beta)$ for single collisions in silicon by particles with $\beta\gamma = 4$, calculated with different theories. In order to show the structure of the functions clearly, the ordinate is $\sigma(E; \beta) / \sigma_R(E; \beta)$. The abscissa is the energy loss E in a single collision. The Rutherford cross-section Eq. (1) is represented by the horizontal line at 1.0. The solid line was obtained with the relativistic version of Eq. (5) of the Bethe–Fano theory [18]. The cross-section calculated with FVP (Eq. (7)) is shown by the dashed line. The dashed line is calculated with a binary encounter approximation [35,36]. The functions all extend to $E_{\text{max}} \sim 16 \text{ MeV}$; see Eq. (1). The moments (Section 3) are $M_0 = 4 \text{ collisions}/\mu\text{m}$ and $M_1 = 386 \text{ eV}/\mu\text{m}$. The atomic shells are indicated by the letters M, L, K.

calculated with the relativistic version of Eq. (5) for minimum ionizing particles [34] is shown by the solid line in Fig. 5. B–F calculations are not available for gases, but see Section 2.4 and Appendix A.

2.3. Fermi virtual photon (FVP) cross-section

The GOS of Fig. 4 has been approximated [4,10,32,47] by replacing $f(E, K)$ for $Q < E$ by the DOS $f(E, 0)$ and by placing a delta function at $Q = E$ [10]. This approach is

here named the FVP method. It is also known under the names photo absorption ionization (PAI) model and the Weizsäcker–Williams approximation.

The differential CCS in the non-relativistic approximation is given by Ref. [10]

$$\sigma(E; v) = \sigma_R(E; v) \left[Ef(E, 0) \ln(2mv^2/E) + \int_0^E f(E', 0) dE' \right] \quad (6)$$

where for $E > E_M$, $\sigma(E; v) = 0$.

This model has the advantage that it is only necessary to know the DOS for the absorber, or, equivalently, the imaginary part of the inverse of the complex dielectric function $\text{Im}(-1/\varepsilon)$. Data for ε can be extracted from a variety of optical measurements [48,49]. In addition, $\text{Im}(-1/\varepsilon)$ can be obtained from electron energy loss measurements [50]. A detailed description of the relativistic PAI model is given e.g. in Refs. [10,16]. The relativistic cross-section is given here in the form of Eq. (28) in Ref. [10], except that $\sigma(E; \beta)$ is written instead of $d\sigma/dE$:

$$\begin{aligned} \sigma(E; \beta) = & \frac{\alpha}{\beta^2 \pi} \frac{\sigma_\gamma(E)}{EZ} \ln[(1 - \beta^2 \varepsilon_1)^2 + \beta^4 \varepsilon_2^2]^{-1/2} \\ & + \frac{\alpha}{\beta^2 \pi} \frac{1}{Nhc} \left(\beta^2 - \frac{\varepsilon_1}{|\varepsilon|^2} \right) \Theta \\ & + \frac{\alpha}{\beta^2 \pi} \frac{\sigma_\gamma(E)}{EZ} \ln \left(\frac{2mc^2 \beta^2}{E} \right) \\ & + \frac{\alpha}{\beta^2 \pi} \frac{1}{E^2} \int_0^E \frac{\sigma_\gamma(E')}{Z} dE' \end{aligned} \quad (7)$$

with $\sigma_\gamma(E) = f(E, 0) \times 1.098 \times 10^{-16} \text{ cm}^2 \text{ eV}$ [51], $\sigma_\gamma(E) \sim (E/N)\varepsilon_2(E)$, and $\tan \Theta = \varepsilon_2 \beta^2 / (1 - \varepsilon_1 \beta^2)$. For gases, ε_2 and $\varepsilon_1 - 1$ are proportional to the gas pressure p , therefore from Eq. (7) we must expect that the straggling function for a segment of length $x_1 p_1$ will differ from that of a segment of length $x_2 p_2$ even if $x_1 p_1 = x_2 p_2$ (see Fig. 16).

The cross-section calculated with Eq. (7) for Si is given by the dashed line in Fig. 5. For P10 it is given by the solid line in Fig. 6,⁵ for Ne in Fig. J.2. Calculations have also been made for several other gases, but are not given here. Optical data used are described in Appendix C.

2.4. Calculation and comparison of cross-sections

For the calculation of CCS it is not practical to calculate $f(E, K)$ or $\sigma_\gamma(E)$ ab initio for each use. I have used numerical tables for these functions [26], rather than using e.g. a polynomial approximation to the photo absorption cross-sections [53], also see Appendix C. For the optical absorption coefficients $\sigma_\gamma(E)$ used in Eq. (7) it must be noted that the lowest excitation energy for Ar is 11.6 eV

⁵The gas pressure is assumed to be 1 atm. A dependence on gas pressure is shown in Fig. 16 and in Section 7.2.

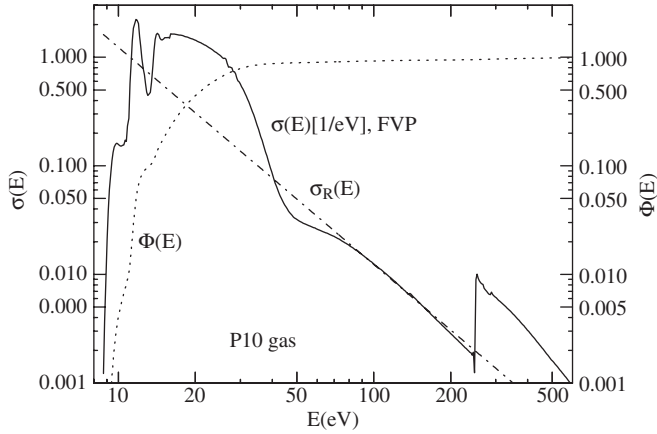


Fig. 6. Inelastic collision cross-section $\sigma(E; \beta\gamma)$ for single collisions in P10 gas by ionizing particles with $\beta\gamma = 3.6$, calculated with FVP theory: solid line. The Rutherford cross-section Eq. (1) is given by the dash-dotted line. The dotted line represents the cumulative probability density function $\Phi(E)$ of Eq. (7), see Fig. 9. For $\beta\gamma = 3.6$ the functions extend to $E_{\max} \sim 13$ MeV, see Eq. (1). The moments are $M_0 = 30$ collisions/cm and $M_1 = 2.1$ keV/cm. The ionization energy for Ar is $E_1 = 15.8$ eV [52], for the L-shell it is 250 eV. Functions for Ne are given in Appendix J.

and the ionization energy is 15.94 eV. For methane, these values are 8.5 and 12.6 eV [52]. In Ar the collisions with $11.6 < E < 15.94$ eV lead to excited states which can produce secondary ionization; see Section 9. If we want to compare calculations of $\sigma(E; \beta)$ with experimental stopping powers dE/dx ; see Section 3, we must include all energy losses because they are included in the standard measurements of dE/dx .

For this study, differential CCS $\sigma(E; \beta)$ have been calculated with FVP for Ne, Ar and P10; for Si both the B–F and the FVP method were used. These functions for ionizing particles with $\beta\gamma = 4$ in Si are shown in Fig. 5. Numerical tables are available in Ref. [26]. The Rutherford cross-section is given by the analytic form, Eq. (1) and is shown by the horizontal line in Fig. 5. An example from a binary encounter algorithm is included. The shape of this function is quite different.⁶ The FVP result for Si agrees reasonably well with the B–F result even though it differs by as much as 50% at some energy losses E .

The moments $\Sigma_t (= M_0)$ and M_1 (Section 3) and the most probable values Δ_p for straggling functions $f(\Delta)$ (Section 5) for a Si-absorber of thickness $x = 8 \mu\text{m}$ calculated with both methods are listed in Table 1. The differences in Σ_t are 6–8%, in M_1 less than 1% and in Δ_p around 3%. These differences change little with particle speed.

The ratio M_1/Δ_p is not given in the table. It increases from 1.46 to 3.14 with $\beta\gamma$, while Σ_t/Δ_p is almost constant for $\beta\gamma > 0.5$. Σ_t and Δ_p reach asymptotic values to within $\pm 0.1\%$ for $\beta\gamma > 50$. The minimum values for Σ_t are near $\beta\gamma = 16$, for M_1 at $\beta\gamma = 3.2$, and for Δ_p at $\beta\gamma = 5$.

⁶The parameters of the function can of course be chosen to get agreement e.g. for the moments, Eq. (13), see Ref. [35].

Table 1

Integral properties of CCS for Si calculated with Bethe–Fano (B–F) and FVP algorithms

$\beta\gamma$	Σ_t		M_1		Δ_p/x	
	B–F	FVP	B–F	FVP	B–F	FVP
0.316	30.325	32.780	2443.72	2465.31	1677.93	1722.92
0.398	21.150	22.781	1731.66	1745.57	1104.90	1135.68
0.501	15.066	16.177	1250.93	1260.18	744.60	765.95
0.631	11.056	11.840	928.70	935.08	520.73	536.51
0.794	8.433	9.010	716.37	720.98	381.51	394.03
1.000	6.729	7.175	578.29	581.79	294.54	304.89
1.259	5.632	5.996	490.84	493.65	240.34	249.25
1.585	4.932	5.245	437.34	439.72	207.15	215.02
1.995	4.492	4.771	406.59	408.70	187.39	194.60
2.512	4.218	4.476	390.95	392.89	176.30	183.06
3.162	4.051	4.296	385.29	387.12	170.70	177.16
3.981	3.952	4.189	386.12	387.89	168.59	174.81
5.012	3.895	4.127	391.08	392.80	168.54	174.63
6.310	3.865	4.094	398.54	400.24	169.62	175.60
7.943	3.849	4.076	407.39	409.07	171.19	177.10
10.000	3.842	4.068	416.91	418.58	172.80	178.66
12.589	3.839	4.064	426.63	428.29	174.26	180.06
15.849	3.839	4.063	436.30	437.96	175.45	181.24
19.953	3.839	4.063	445.79	447.44	176.36	182.14
25.119	3.840	4.063	455.03	456.68	177.04	182.79
31.623	3.840	4.064	463.97	465.63	177.53	183.28
39.811	3.841	4.064	472.61	474.27	177.86	183.61
50.119	3.842	4.065	480.93	482.58	178.09	183.83
63.096	3.842	4.065	488.90	490.55	178.22	183.95
79.433	3.842	4.065	496.52	498.17	178.32	184.06
100.000	3.842	4.066	503.77	505.42	178.38	184.10
125.893	3.843	4.066	510.66	512.31	178.43	184.15
158.489	3.843	4.066	517.20	518.84	178.44	184.17
199.526	3.843	4.066	523.40	525.05	178.47	184.18
251.189	3.843	4.066	529.29	530.94	178.48	184.18
316.228	3.843	4.066	534.91	536.56	178.48	184.21
398.107	3.843	4.066	540.28	541.92	178.48	184.22
501.187	3.843	4.066	545.43	547.08	178.48	184.22
630.958	3.843	4.066	550.40	552.05	178.48	184.22
794.329	3.843	4.066	555.21	556.86	178.48	184.22
1000.00	3.843	4.066	559.89	561.54	178.48	184.22

$\Sigma_t = M_0$ [collisions/ μm], M_1 [eV/ μm] for heavy particles, Δ_p in eV for $x = 8 \mu\text{m}$. B–F presumably is more accurate. Numerical values can be found in Ref. [26].

The minimum values for Σ_t are at $\beta\gamma \sim 18$, for M_1 at $\beta\gamma \sim 3.2$, for Δ_p at $\beta\gamma \sim 5$. The relativistic rise for Σ_t is 0.1%, for M_1 it is 45%, for Δ_p it is 6%. The difference between B–F and FVP is $\sim 6\%$ for Σ_t , 0.3–0.9% for M_1 and $\sim 3\%$ for Δ_p .

Straggling functions calculated with both methods are compared in Appendix A.

I expect that similar differences exist between B–F and FVP for Ar and P10, but since the *absolute differences* between the results for B–F and FVP will enter as systematic errors into the TPC calibration (Section 14) only the *dependence on particle speed of these differences* will be important in PID.

Therefore, I believe that the FVP method will be adequate for present purposes, at least for light elements. Data for $f(E, 0)$ are available, Appendix C, so that calculations can be made for many substances.

Several tests should be made for any such calculation: the sum rule for optical data (Eq. (16)) should be fulfilled, the I -value I (Eq. (17)) should be compared to tabulated data [39,40] and M_1 should agree with established values of dE/dx [39,40]. My calculations until April 2003 were made for Ar only. Later calculations were made for P10. The differences between Ar and P10 are not large and are given for straggling functions in Appendix B.

3. Integral functions of collision cross-sections (CCS)

Integrals over the differential cross-section $\sigma(E; \beta)$ are needed in the Monte Carlo calculations of straggling functions. They can be used for comparisons with measurements of stopping powers which provide one reality check of the calculations. They also show the rarity of large energy losses.

3.1. Total cross-sections and mean free paths

The macroscopic (total) CCS is defined as the number of collisions per cm

$$\Sigma_t(\beta\gamma) \equiv N \int \sigma(E; \beta\gamma) dE \quad (8)$$

where N is the number of atoms per cm^3 . It determines the average number $m_c = x\Sigma_t$ of collisions in a segment of length x .

Values of $\Sigma_t = M_0$ for Si are given in Table 1, for P10 gas and Ne in Table 2. For Si, Ne and Ar it may be noted that the values of M_1 agree to about 1% with the data for muons in Ref. [38].

The inverse of Σ_t is the mean free path between collisions $\lambda \equiv 1/\Sigma_t$ (9)

and is used to calculate the distance between collisions in a Monte Carlo calculation: $x = -\lambda \cdot \ln r_r$ where $0 < r_r < 1$ is a random number. The dependence of λ on $\beta\gamma$ is given in Fig. 7. An approximation for the gas used in the ALICE TPC (currently 85% Ne, 10% CO_2 and 5% N_2) is made by using the CCS for Ne with a gas density $\rho = 0.00091 \text{ g/cm}^3$ for the CERN altitude. A better approximation can be made by including optical data for N_2 and CO_2 from Ref. [52].

3.2. Cumulative probability density function $\Phi(E)$

For the Monte Carlo calculations described in Fig. 3, the stochastic energy loss E for *single collisions* is selected from the cumulative p.d.f. (also called cumulative distribution function)

$$\Phi(E; \beta\gamma) = \int^E \sigma(E'; \beta\gamma) dE' / \int^{\infty} \sigma(E'; \beta\gamma) dE'. \quad (10)$$

Examples of $\Phi(E; \beta\gamma)$ for Si are given in Fig. 8. The dependence of these functions on $\beta\gamma$ is not large. For P10 gas, Figs. 6, 9 and 10, the dependence is even less. Numerical tables can be found in Ref. [26]. This small

Table 2

Integral properties of CCS, Eq. (13), calculated with the FVP algorithm for P10 and the ALICE TPC Ne gas ($\rho = 0.91 \text{ mg/cm}^3$)

$\beta\gamma$	P10				Ne	
	A_p	w	M_0	M_1	M_0	M_1
0.316	22.0926	11.4916	211.0726	15.1286	91.8949	9.9703
0.398	14.6338	8.1277	146.5664	10.7146	64.0487	7.0517
0.501	9.9505	5.8737	103.9873	7.7376	45.6034	5.0810
0.631	7.0166	4.3998	76.0672	5.7440	33.4737	3.7696
0.794	5.1720	3.4753	57.9161	4.4322	25.5713	2.9050
1.000	4.0128	2.9035	46.2566	3.5811	20.4887	2.3466
1.259	3.2927	2.5456	38.8999	3.0442	17.2819	1.9936
1.585	2.8565	2.3229	34.3884	2.7197	15.3192	1.7796
1.995	2.6043	2.1897	31.7545	2.5369	14.1800	1.6590
2.512	2.4717	2.1173	30.3570	2.4494	13.5846	1.6002
3.162	2.4170	2.0853	29.7722	2.4253	13.3474	1.5829
3.981	2.4133	2.0800	29.7206	2.4432	13.3459	1.5930
5.012	2.4428	2.0919	30.0180	2.4890	13.4992	1.6211
6.310	2.4941	2.1147	30.5430	2.5531	13.7539	1.6612
7.943	2.5593	2.1443	31.2156	2.6291	14.0747	1.7090
10.000	2.6337	2.1779	31.9825	2.7127	14.4387	1.7618
12.589	2.7137	2.2140	32.8078	2.8011	14.8305	1.8178
15.849	2.7970	2.2513	33.6658	2.8923	15.2399	1.8757
19.953	2.8820	2.2892	34.5369	2.9847	15.6598	1.9347
25.119	2.9674	2.3271	35.4067	3.0772	16.0853	1.9941
31.623	3.0523	2.3649	36.2903	3.1693	16.5121	2.0535
39.811	3.1370	2.4024	37.2469	3.2607	16.9365	2.1125
50.119	3.2162	2.4394	38.0550	3.3485	17.3547	2.1706
63.096	3.2888	2.4758	38.6576	3.4321	17.7706	2.2276
79.433	3.3556	2.5116	39.0968	3.5115	18.1605	2.2828
100.000	3.4178	2.5468	39.4162	3.5874	18.5054	2.3353
125.893	3.4761	2.5813	39.6515	3.6600	18.7926	2.3845
158.489	3.5312	2.6150	39.8283	3.7296	19.0191	2.4301
199.526	3.5832	2.6477	39.9648	3.7963	19.1915	2.4722
251.189	3.6322	2.6793	40.0725	3.8601	19.3194	2.5108
316.228	3.6776	2.7094	40.1590	3.9209	19.4125	2.5464
398.107	3.7186	2.7374	40.2288	3.9784	19.4794	2.5792
501.187	3.7547	2.7630	40.2850	4.0325	19.5271	2.6098
630.957	3.7853	2.7859	40.3296	4.0830	19.5610	2.6383
794.328	3.8101	2.8055	40.3634	4.1298	19.5852	2.6651
1000.000	3.8292	2.8219	40.3885	4.1731	19.6024	2.6904

A_p and FWHM w given in keV for $x = 2 \text{ cm}$, $\Sigma_t = M_0$ in collisions/cm, M_1 in keV/cm. Numerical values can be found in Ref. [26].

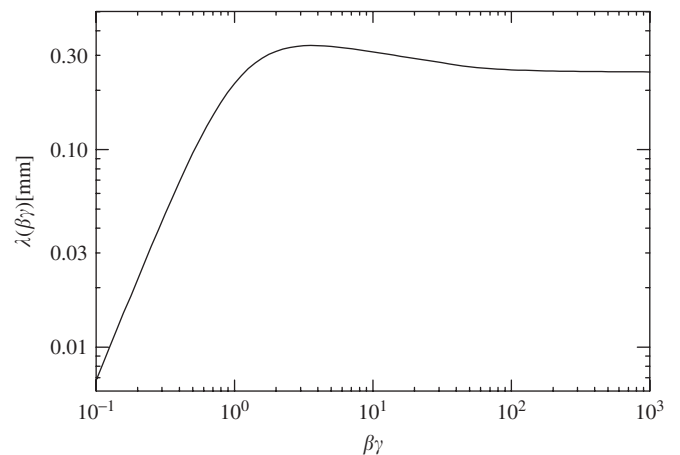


Fig. 7. The mean free path length λ , Eq. (9), as function of $\beta\gamma$ for P10 gas at 1 atm and 20°C ($Z = 17.2$, $A = 37.5575$ and $\rho = 1.5616 \text{ mg/cm}^3$).

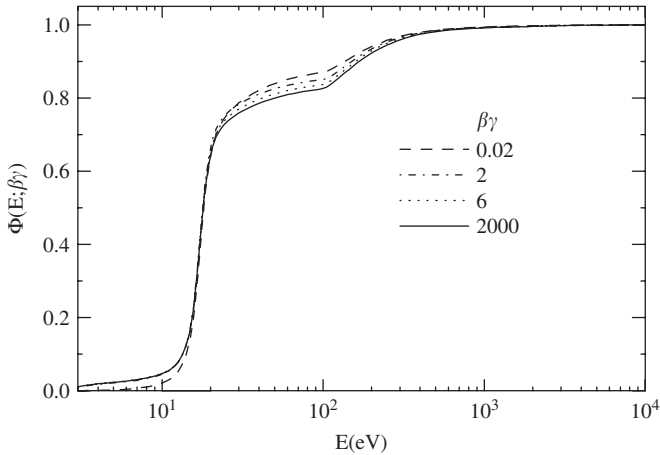


Fig. 8. Cumulative energy loss functions $\Phi(E)$, Eq. (10), for single collisions in Si are shown for several values of $\beta\gamma$. The excitation energy for L_2 electrons is 100 eV, for K electrons it is 1840 eV. Details for $E < 250$ eV can be found in Ref. [29]. A table of the functions is given in Ref. [26].

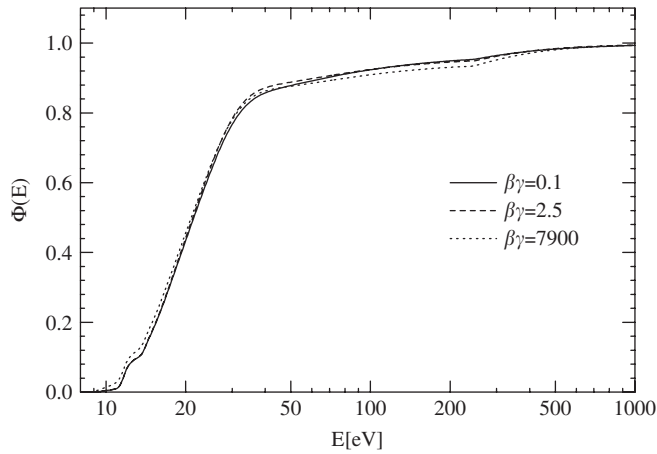


Fig. 9. Cumulative energy loss functions $\Phi(E)$ for single collisions in P10 gas, Eq. (10), are shown for several values of particle speed $\beta\gamma$. For $1.0 \leq \beta\gamma \leq 7.9$ the difference between the functions is no more than the width of the line. A table of the functions is given in Ref. [26].

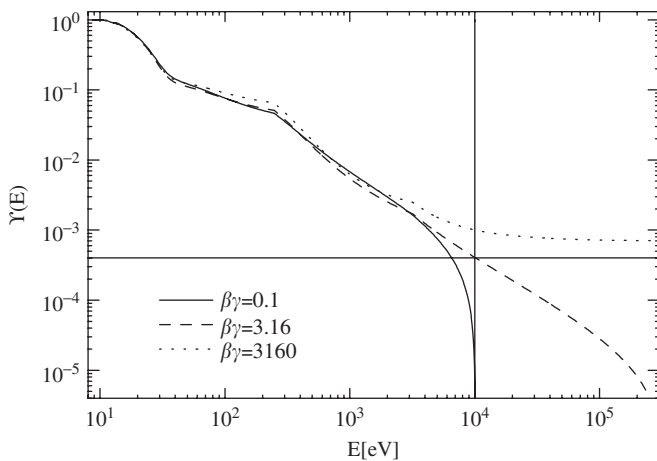


Fig. 10. Probabilities $\Upsilon(E) = 1 - \Phi(E)$ for single collisions in P10 gas in which the energy loss exceeds a value E for different $\beta\gamma$ in P10 gas.

dependence of $\Phi(E)$ on $\beta\gamma$ can simplify Monte Carlo calculations involving single collisions. For gases, to a reasonable approximation, a single function $\Phi(E)$ can be used for all speeds.

The equivalent functions $F(\Delta)$ for energy losses Δ for track segments are given in Section 5.2. They are used for Monte Carlo calculations for energy losses along tracks.⁷

The complementary function $\Upsilon(E) = 1 - \Phi(E)$ for P10 gas is given in Fig. 10. As an example for a track of total length $t = 120$ cm in STAR, the average total number of collisions for $\beta\gamma = 3.16$ is $m_c = t\Sigma_t = 120 \times 30 = 3600$ (Table 2). The number of collisions exceeding $E_1 = 10$ keV is $m_1 = \Upsilon(10^4; 3.16) \times m_c = 1.4$; $\Upsilon(10^4; 3.16) \approx 0.0004$ is shown by the vertical and horizontal lines in Fig. 10. For Si, Fig. 8, the energy loss for more than 90% of all collisions is below 200 eV.

The macroscopic cross-section (collisions/cm) for energy losses exceeding a value E_r is

$$\Sigma_t(E_r; \beta\gamma) \equiv N \int_{E_r}^{E_{\max}} \sigma(E; \beta\gamma) dE. \quad (11)$$

It is equal to $\Upsilon(E_r) \times \Sigma_t(\beta\gamma)$. If $\sigma(E; \beta\gamma)$ from FVP is not available, a 10% estimate of $\Sigma_t(E_r)$ for large energy losses, approximately $10 \leq E_r(\text{keV}) \ll E_{\max}$, can be made with the approximation calculated with the Rutherford cross-section, Eq. (1). Neglecting the term $\beta^2 E/E_{\max}$ it is

$${}_R\Sigma_t(E_r) \sim 153 \frac{\rho Z}{\beta^2 A E_r} \frac{1}{\beta^2 E_r(\text{keV})} = \frac{y}{\beta^2 E_r(\text{keV})} \quad (12)$$

in units of 1/cm, E_r in keV, and with $y = 0.064$ for Ne, $y = 0.114$ for Ar and $y = 178$ for Si. For example, for $\beta \sim 1$ and $E_r = 10$ keV in Ar, $\Sigma_t(E_r) = 0.011/\text{cm}$, and, on the average, only one collision with $E > 10$ keV will occur on a track of length $t = 90$ cm. (See Section 9, also see Fig. 9 or 10).

3.3. Moments of collision cross-sections, stopping power and sum rules

It is useful to consider the moments of $\sigma(E)$. Here they are defined by Refs. [18,28,54]

$$M_\nu(\beta) \equiv N \int E^\nu \sigma(E; \beta) dE. \quad (13)$$

A sum over excited states is included in the integral. In general, $\sigma(E)$ will have finite values over a certain range of values of E and will be zero elsewhere, thus no limits need to be defined for the integral.⁸ If the collisions are statistically independent, the moments are related to experimentally observed quantities.

The moment M_0 is the total CCS Σ_t (Section 3.1). M_0 is the most important parameter for the calculation of

⁷Monte Carlo calculations are described in Section 4.4.

⁸The Rutherford cross-section is an exception. For M_1 , the limits E_{\max} , Eq. (1), and $E_{\min} \sim I^2/E_{\max}$ are usually used. For M_0 no plausible lower limit is available, see Section 4.5, but Eq. (15) might be of use.

straggling functions. Its magnitude is determined almost completely by energy losses $E < 1000$ eV, as shown in Figs. 8–10. Theories for M_0 can be found in Refs. [28,36,45]. The moment M_1 is usually called the stopping power $-dT/dx$, where T is the kinetic energy of particles. It can be calculated with the Bethe–Bloch equation, in Ref. [1, Eq. (27.1)].⁹

The moments are obtained as an incidental result of the calculation of $\sigma(E)$ in Sections 2.2 and 2.3. M_0 and M_1 for P10 are given in Figs. 24 and 25. M_1 agrees to 1% with the ionization stopping power found in Ref. [38]. Note that in Ref. [38] other contributions to dE/dx appear for $\beta\gamma > 100$, see Appendix I. The mean energy loss $\langle\Delta\rangle$ in an absorber of thickness x is $\langle\Delta\rangle = x dT/dx$. Values are given in Figs. 13, 14, G.1 and G.2, where it is seen that $\langle\Delta\rangle$, and the higher moments, are not useful in the current context [54,57,58]. The partial (restricted) stopping power S_r is given by

$$S_r(E; \beta) \equiv N \int^E E' \sigma(E'; \beta) dE'. \quad (14)$$

The mean energy loss per collision given by

$$\langle E \rangle = M_1 / M_0 \quad (15)$$

varies slowly with particle speed for $\beta\gamma < 100$. It might be useful for estimates of general features of straggling functions for absorbers where M_1 is known.¹⁰ A useful quantity in the calculation of CCS is the moment of the DOS $f(E, 0)$

$$S_0 = \int f(E, 0) dE \quad (16)$$

which usually is called the Thomas–Reiche–Kuhn sum rule [45]. It should equal the atomic number of the absorber and can be used as one of the checks for the reliability of the computer programs. Equally useful is the mean logarithmic excitation energy I defined by Ref. [28]

$$\log I = \int f(E, 0) \log E dE. \quad (17)$$

It should agree with tabulated values [39,40]. Values of I have been calculated for some materials [59,60] but originally were derived from experimental measurements of dE/dx [55,61,62].

4. Calculation of straggling (“Landau”) functions

Energy loss distribution functions $f(\Delta; x, \beta\gamma)$ (also called energy loss spectra) are usually called *straggling functions*, and the expression “Landau function” here refers specifically to the function derived from the Rutherford cross-section [2,17,18], see Fig. 1. In particle physics, the name “Landau function” is used generically to refer to all straggling functions. For a good understanding of strag-

gling functions it is useful to consider separately the distributions of the number of collisions in a segment x (Section 4.1), and the energy loss spectra for multiple collisions (Section 4.2). These are the energy loss spectra of particles which have made exactly n collisions in a segment. For very thin absorbers the Poisson distribution dominates the shape of the straggling function, Fig. 2 and Ref. [5]. Methods to calculate straggling functions are described in Sections 4.3–4.5.

4.1. Poisson distribution

An important feature for the understanding of straggling functions is the Poisson distribution giving the distribution of the number of collisions in a segment x [16,18]

$$P(n) = \frac{m_c^n}{n!} e^{-m_c} \quad (18)$$

where $P(n)$ gives the fraction of particles suffering n collisions, and $m_c = x\Sigma_t = xM_0 = x/\lambda$ is the average number of collisions for all particles.

The mean value for $P(n)$ is m_c , and the standard deviation is $s = \sqrt{m_c}$, with a relative width $s/m_c = 1/\sqrt{m_c}$. Note that the large difference in the FWHM between straggling functions and the Landau function in Figs. 1 and 13 is in part due to the difference in m_c ; see Section 4.5.

4.2. Energy loss spectra for multiple collisions

The spectra for multiple collisions can be calculated by convolution. The n -fold convolution of the single collision spectrum $\sigma(E)$ is obtained by iteration

$$\begin{aligned} \sigma(\Delta)^{*n} &= \int_0^\Delta \sigma(E) \cdot \sigma^{*(n-1)}(\Delta - E) dE \quad \text{with} \\ \sigma(\Delta)^{*0} &= \delta(\Delta) \quad \text{and} \quad \sigma(\Delta)^{*1} = \sigma(E). \end{aligned} \quad (19)$$

Here, the particle speed v is implicit as a parameter. Examples of convolution spectra of Eq. (19) for P10 are given in Fig. 11. Note the large reduction of the 12 eV spike for $n = 2$, and its complete disappearance for $n = 3$. The spectra for Si are given in Fig. 12.

4.3. Analytic calculation of straggling functions $f(\Delta; x, \beta\gamma)$ for segments

Accurate straggling functions can only be obtained with the use of the CCS described in Sections 2.2, 2.3 and Appendix J. A convenient and accurate method to calculate $f(\Delta; x, \beta\gamma)$ is with convolutions [5,10,16,18], with $m_c = x\Sigma_t(v)$

$$f(\Delta; x, v) = \sum_{n=0}^{\infty} \frac{m_c^n e^{-m_c}}{n!} \sigma(\Delta; v)^{*n}. \quad (20)$$

A more practical and faster method is described in Ref. [18]. It has been used for the calculations described here. There

⁹Eq. (27.1) in Ref. [1] is an approximation for M_1 valid for large speeds, say $\beta > 0.2$. For $\beta < 0.2$ a complete theory is given in Refs. [38,40,46,55,56].

¹⁰For P10, Table 2, $\langle E \rangle = 85$ eV $\pm 10\%$ for $1 < \beta\gamma < 200$, for Ne $\langle E \rangle = 125$ eV $\pm 10\%$, for liquid water $\langle E \rangle = 65$ eV $\pm 10\%$.

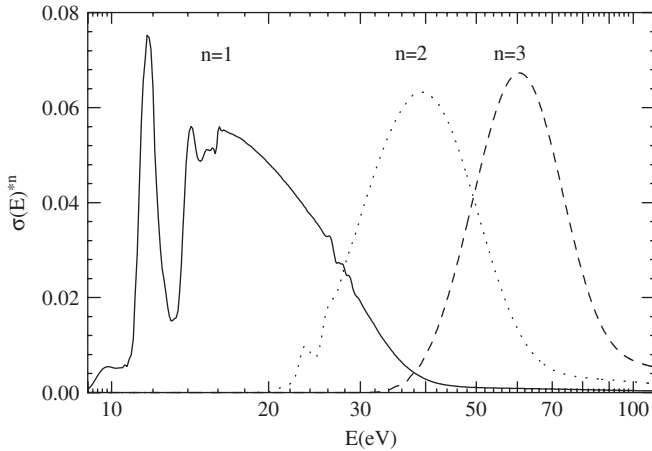


Fig. 11. The first three convolution spectra $\sigma(E)^{*n}$ defined in Eq. (19) for P10-gas are given. Solid line: single collisions, dotted line: two collisions, dashed line: three collisions. To show detail ordinates for $\sigma(E)^{*2}$ and $\sigma(E)^{*3}$ are not to scale.

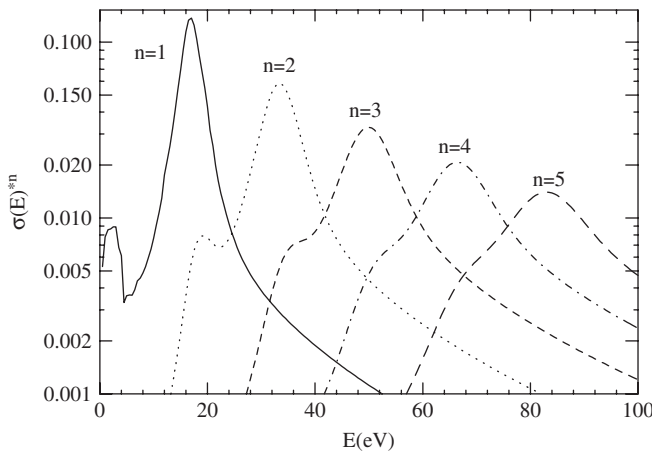


Fig. 12. Same as Fig. 11, but for solid Si, and for n up to 5. The *plasmon peak* at 17 eV appears in each spectrum at $17n$ eV, and its FWHM is proportional to n . The structure at ~ 2 eV appears at $2 + 17(n-1)$ eV, but diminishes with increasing n . For $n=6$ (not shown) the plasmon peak (at 102 eV) merges with the L-shell energy losses at 100 eV, also see Fig. 2.

are no simple analytic functions which represent straggling functions. Calculations with the analytic methods are fast. For the study of the performance of detectors many straggling functions will be needed. While they can be calculated quickly¹¹ it may be more efficient to store straggling functions as numerical tables on a computer. This is the approach currently used for the STAR TPC: straggling functions for $0.1 < \beta\gamma < 1000$ and many segment lengths x are stored [67].

An alternative approach is the method of scaling based on the similarities of straggling functions as discussed in Section 8. A modification useful for some calculations was

¹¹With a 2 GHz CPU, the calculation of a straggling function for one segment takes 0.5 s.

described by Williams [4]. The cumulative function $F(\Delta; x, v)$ defined in Section 5.2 is used for applications.¹²

4.4. Monte Carlo calculation of straggling functions

An actual *simulation of the traversal* of a particle through a segment of length x can be done with a Monte Carlo calculation, as shown in Fig. 3. In Monte Carlo calculations, the interactions occurring during the passage of the particles through matter are simulated one at a time, collision by collision, and include secondary collisions by the δ rays [29]. A particle j travels random distances x_i between successive collisions, calculated by selecting a random number r_r and determining the distance to the next collision from the mean free path λ given by Eq. (9)

$$x_i = -\lambda \ln r_r = -(\ln r_r) / \Sigma_t(\beta\gamma). \quad (21)$$

The energy loss E_i is selected with a second random number from the integrated collision spectrum of Eq. (10) or Figs. 8 and 9. This process is repeated until $\sum x_i$ exceeds the segment length x . The total energy loss Δ_j of the particle is $\Delta_j = \sum_i E_i$. To get E_i practically, the inverse function $E(\Phi; \beta\gamma)$ of $\Phi(E; \beta\gamma)$ is calculated with cubic spline interpolation [26]. The straggling function $f(\Delta)$ is obtained by binning the Δ_j . The method suggested for the ALICE TPC in Ref. [23, Section 7] is described in Appendix J and in Ref. [26]. The calculation of straggling functions for tracks is described in Section 6.

4.5. Landau–Vavilov calculation of straggling functions and modifications

This section concerns the reasons for the difference between the Landau function¹³ and the functions calculated here. In particular, the difference in the number of collisions m_c leading to the broadening of $f(\Delta)$ seen in Fig. 1 is discussed (also see Ref. [18, Appendix H]). In the Landau–Vavilov calculations [5,17,18,37] Laplace transforms were used to solve the transport equation for the Rutherford cross-section, Eq. (1). In order to get the correct non-relativistic *asymptotic stopping power* M_1 , Landau used the conventional values $E_{\min} = I^2/2mv^2$ and $E_{\max} = 2mv^2$ [28] to calculate M_1 , Eq. (13).

Neglecting the term $\beta^2 E/E_{\max}$ in Eq. (1) and setting $z = 1$, we get for M_1

$$M_1 = \frac{k}{\beta^2} \rho \frac{Z}{A} \ln \frac{E_{\max}}{E_{\min}} = \frac{k}{\beta^2} \rho \frac{Z}{A} 2 \ln \frac{2mv^2}{I} \quad (22)$$

where I is defined in Eq. (17), and M_1 equals the Bethe result [44] without shell-, Barkas- and Bloch-corrections.

¹²Monte Carlo calculations (Section 4.4 and [63]), with sufficient statistics [26], as well as Laplace transform methods with $\sigma(E; v)$ (Section 4.5 and [5,17,37]) have been shown to give results identical to the convolutions [26].

¹³The Vavilov straggling functions [5,37] were also derived from Eq. (1). For the thin absorbers described here they differ little from the Landau functions.

For the CCS we get¹⁴

$$\begin{aligned} {}_R M_0 &= \frac{k}{\beta^2} \rho \frac{Z}{A} \left(\frac{1}{E_{\min}} - \frac{1}{E_{\max}} \right) \sim \frac{k}{\beta^2} \rho \frac{Z}{A} \frac{2mc^2 \beta^2}{I^2} \\ &= k \rho \frac{Z}{A} \frac{2mc^2}{I^2}. \end{aligned} \quad (23)$$

Thus ${}_R M_0$ does not depend on v . Values for Si are ${}_R M_0 = 6 \times 10^6$ collisions/cm, for Ar 3600 collisions/cm. They are much larger than the values of M_0 given in Tables 1 and 2. For example, for $\beta\gamma = 3.6$ in Si, $M_0 = 4 \times 10^4$ collisions/cm. Therefore, the relative width $s = 1/\sqrt{\langle m_c \rangle}$ of the Poisson distribution, Eq. (18), for the Rutherford cross-section result is much less than that for the realistic cross-sections. As a consequence the Landau function in Fig. 1 is much narrower than the straggling function. With increasing x the differences in w diminish, see Ref. [18, Fig. 15].

Straggling functions could be calculated with Laplace transforms for the spectra given in Figs. 5 and 6, but the integrations would be tricky and tedious [27,54]. The results would be the same. In order to achieve reduced values of M_1 relating to the fact that large energy losses cannot deposit all their energy in thin absorbers, the maximum energy loss E_{\max} in Eq. (22) can be replaced by $E_r < E_{\max}$, leading to a “restricted mean energy loss”. Calculations have been made with “restricted energy transfers”; see Ref. [1, Eq. (27.7)]. In the non-relativistic approximation this leads to a modified Eq. (22), viz.

$${}_R M_1 = \frac{k}{\beta^2} \rho \frac{Z}{A} \ln \frac{2mv^2 E_r}{I^2} \quad (24)$$

where E_r is the same as T_{cut} in Ref. [1, Eq. (27.7)].¹⁵ It is then possible to obtain the experimental values of Δ_p by choosing E_r [64]. A comparison with Landau’s equation for Δ_p (Eq. (36)), written in a form equivalent to Eq. (24), i.e.

$$\Delta_p/x = \frac{k}{\beta^2} \rho \frac{Z}{A} \ln \frac{2mv^2 1.45k\xi}{I^2} \quad (25)$$

shows that E_r , according to Landau [2], would have to equal $1.45kx$, i.e. it would depend on segment length x . For the calculation of ${}_R M_0$ (Eq. (23)), replacement of E_{\max} by E_r would not remedy the problem with m_c described below Eq. (23): typical values of E_{\min} are less than 1 eV and the term $1/E_r$ would be negligible in Eq. (23).

A modification of the large value of ${}_R M_0$ of Eq. (23) can be achieved by “considering the influence of the quantum mechanical resonances,” Blunck and Leisegang [41,65], later studies in Ref. [5,27,42]. The discrepancy between the Blunck and Leisegang calculation, experiment, and FVP calculation was explained in Refs. [18,66, Fig. 11]. A short description is given here. The inclusion of a “resonance” correction K_r^2 for M_2 given by Blunck and Leisegang in

effect results in a convolution of the Landau- (or Vavilov [37]-) function with a Gaussian of width corresponding to K_r^2 which will shift Δ_p and reduce the asymmetry of the straggling function as can be seen in Refs. [5, Fig. 2,18, Fig. 11]. From Eq. (19) it is clear that the largest possible energy loss for a given Δ is $E = \Delta$. This will restrict the effective value of K_r^2 used, see Ref. [18, Appendix G, Fig. 11]. The inclusion of higher moments considered by Blunck and Leisegang leads to divergences discussed in Ref. [54].

5. Examples of straggling functions for segments

5.1. Properties of straggling functions

To define the concepts of most probable energy loss Δ_p and FWHM w and to examine the concept of mean energy loss, a function $f(\Delta; x, \beta\gamma)$ calculated with convolutions is given in Fig. 13 for ionizing particles with $\beta\gamma = 3.6$ traversing a segment of length $x = 1.2$ cm in Ar. The mean energy loss is given by $\langle \Delta \rangle = xM_1(\beta) = 3044$ eV ($M_1(\beta)$ is the Bethe–Bloch function, in Ref. [1, Eq. (27.1)]¹⁶); it is about twice Δ_p , also see Table 2. The mean energy loss calculated for the part of $f(\Delta)$ shown in the figure (i.e. for $0 < \Delta < 5000$ eV) is $\langle \Delta \rangle_r = M_1(5000 \text{ eV})/F(5000 \text{ eV}) = 1723[\text{eV}]/0.9358 = 1841$ eV, Eqs. (26) and (27). It is 35% larger than Δ_p , also see Figs. 18 and 19. For present purposes, $f(\Delta)$ is the same for all particles with charge ± 1 and the same $\beta\gamma$.¹⁷

Functions for several x are shown in Fig. 14: the ratio of Δ_p/x to the Bethe–Bloch mean energy loss $\langle \Delta \rangle/x$ increases with x (also see Fig. 25). For a sensible analysis of ionization in segments, we should use the most probable energy loss Δ_p and the FWHM w as the parameters associated with $f(\Delta)$. Because of the change in shape of $f(\Delta; x)$ with x shown in Figs. G.1 and G.2, the parameters Δ_p and w have a complex dependence on x , as shown in Fig. 15. The dependence of $f(\Delta)$ on gas pressure is shown in Fig. 16.¹⁸ The relation between energy loss Δ , energy deposition D and ionization J is discussed in Section 9.

Fisyak [67] has used $z = \log(\Delta/x)$ as the energy loss variable. An example of $f(z)$ is shown by the solid line in Fig. 17. The Gaussians shown in the figure are equivalent to the Johnson functions [68] (one of several functions discussed by Tschalär [58]). The use of tabulated reference straggling functions with the two parameter scaling

¹⁶With the notation used in this paper, the stopping power must be called dT/dx , where T is the kinetic energy of the particles. Instead I use the expression M_1 , Eq. (13). The expression dE/dx is used wherever reference is made to the common use of the Bethe–Bloch expression. Comments about the uses of the symbol dE/dx for energy deposition, ionization, ADC output etc. are made in the Introduction.

¹⁷For $E > 100$ keV, electron spectra begin to differ from the spectra for heavier particles, see Appendix F.

¹⁸The “density dependence” shown in Ref. [16, Fig. 1.20] is mostly related to the change in effective track length exemplified for Δ_p in Fig. 25.

¹⁴For $\beta^2 > 0.1$ the relativistic correction is very small.

¹⁵It is not clear how the density correction, Eq. (36), should be modified in this approach.

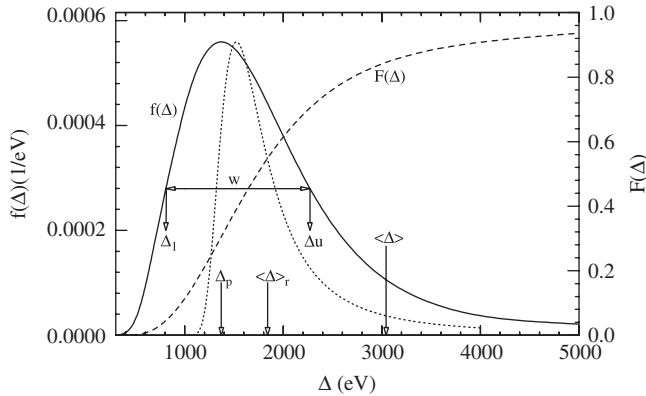


Fig. 13. The straggling function $f(\Delta)$ for particles with $\beta\gamma = 3.6$ traversing 1.2 cm of Ar is given by the solid line. It extends to $\Delta \sim E_{\max} = 13$ MeV. The Landau function [2] is given by the dotted line. The cumulative straggling function, $F(\Delta)$ Eq. (26), is given by the dashed line. Parameters describing $f(\Delta)$ are the most probable energy loss $\Delta_p(x; \beta\gamma)$, i.e. the position of the maximum of the straggling function, at 1371 eV, and the full-width-at-half-maximum (FWHM) $w(x; \beta\gamma) = 1463$ eV. The parameters Δ_l and Δ_u can be used for the scaling procedure of Section 8. Mean energy loss $\langle \Delta \rangle$ and $\langle \Delta \rangle_r$, Eqs. (26) and (27), are discussed in the text.

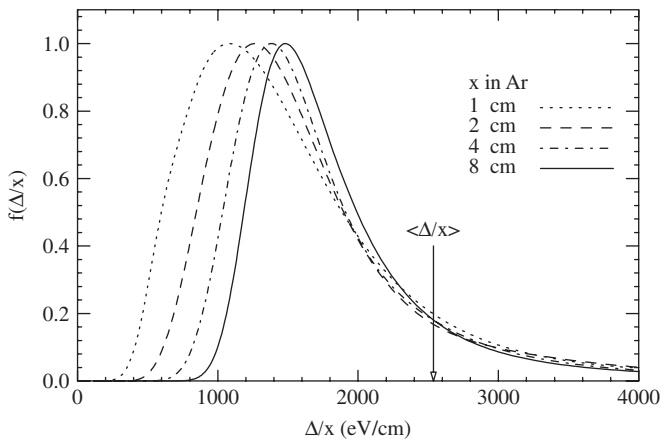


Fig. 14. Calculated straggling (energy loss, “Landau”) functions $f(\Delta/x)$ (note that Δ/x is called dE/dx in current literature of particle physics) for $\beta\gamma = 3.6$ particles, traversing segments $x = 1, 2, 4, 8$ cm in Ar. For the full spectrum extending to 13 MeV, the mean energy loss $\langle \Delta/x \rangle$ is the same for all x . The trend of Δ_p/x with particle speed is shown in Figs. 24 and 25. For Si see [1, Fig. (27.7)]. In order to show the change in shape the functions are scaled to the same peak height.

described in Section 8 gives closer approximations to measured functions in the TPC than these analytic functions and therefore is used in this paper.

5.2. Cumulative straggling functions $F(\Delta; x, \beta\gamma)$

For the Monte Carlo simulation of full particle tracks (Section 6) the cumulative straggling functions $F(\Delta; x, \beta\gamma)$ for segments are needed. They are obtained with

$$F(\Delta; x, \beta\gamma) = \int^{\Delta} f(\Delta'; x, \beta\gamma) d\Delta' \quad \text{and} \quad F(\infty; x, \beta\gamma) = 1. \quad (26)$$

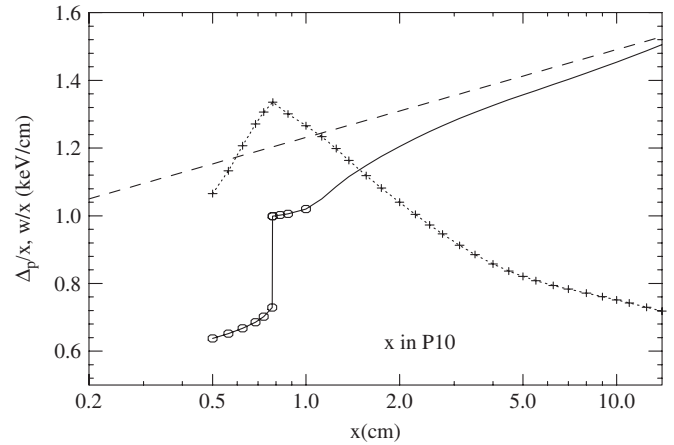


Fig. 15. The dependence of Δ_p/x (solid line) and w/x (dotted line) for particles with $\beta\gamma = 3.6$ on absorber thickness x . The Landau approximation, Eq. (36), $\Delta_p/x = A(\beta\gamma) + \ln x$ is shown by the dashed line. The structure for $x < 1$ cm is due to the increasing contribution from L-shell excitations (Fig. G.2). The Bethe–Bloch $dE/dx = 2.43$ keV/cm would be a horizontal line (see Fig. 24).

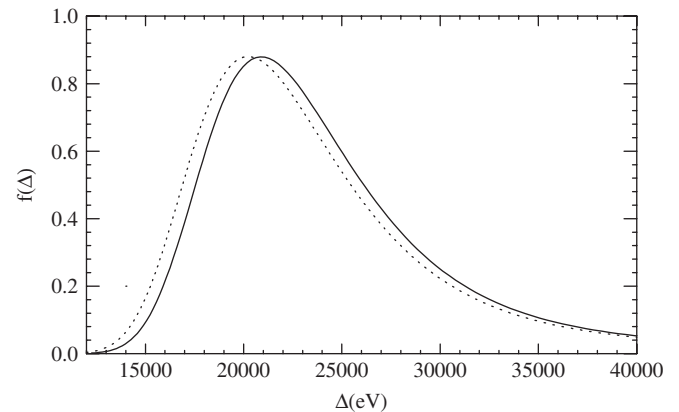


Fig. 16. Straggling (energy loss) functions $f(\Delta)$ for particles with $\beta\gamma = 100$, for $x = 2$ cm at a pressure of 5 atm: dotted line, and $x = 10$ cm at 1 atm: solid line. The shift is caused by the “density effect,” Eqs. (7) and (36). Also see Refs. [69, 16, Figs. 1.20 and 9.3]. The values of Δ_p are 20.23 and 20.9 keV (3.3% different), and $w = 9.728$ and 9.595 keV, a difference of -1.4% . Also see Section 7.2.

An example is given as $F(\Delta)$ in Fig. 13. The corresponding expression for the mean energy loss is

$$M_1(\Delta; x, \beta\gamma) = \int^{\Delta} \Delta f(\Delta'; x, \beta\gamma) d\Delta' / F(\Delta; x, \beta\gamma) \quad (27)$$

where $M_1(\infty; x, \beta\gamma)$ is the Bethe–Bloch result $x \cdot dE/dx$. In a TPC there are restrictions limiting the maximum observable energy loss in a cell: the dynamic range of the ADCs is restricted, and the range of delta-rays may exceed a practical cell volume. For measured spectra it will be difficult to determine the appropriate upper limit of the integral, and the comparison of experiment and calculation with cumulative functions $M_1(\Delta)$ for segments may be inaccurate.

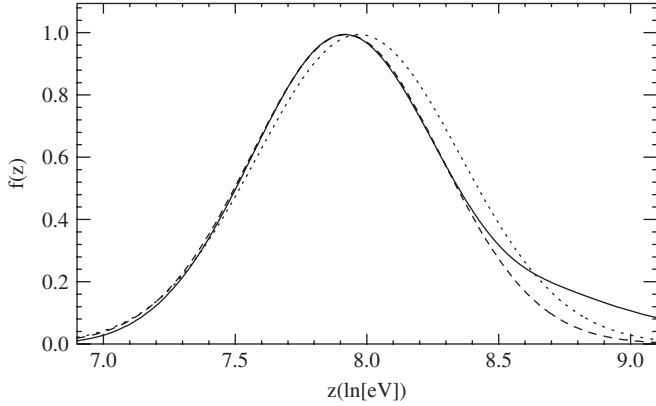


Fig. 17. Solid line: straggling function $f(z)$ for particles with $\beta\gamma = 4.3$, for a segment with $x = 2$ cm. Dashed line: a Gaussian with the most probable energy loss and the FWHM of $f(z)$. The agreement is good for $z < 8.35$ ($\Delta = 4230$ eV). Dotted line: a Gaussian with the mean energy loss and the standard deviation of $f(z)$ limited to $6.9 < z < 9$ shown in the graph. The tail of $f(z)$ for $z > 8.4$ increases the standard deviation, and the corresponding Gaussian does not approximate $f(z)$ well. Also see Fig. 20.

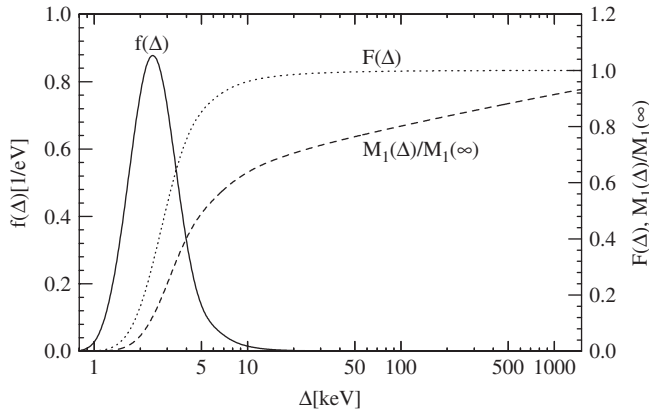


Fig. 18. Straggling function $f(\Delta)$ (Eq. (20)), for particles with $\beta\gamma = 3.7$ traversing 2 cm of P10: solid line, its cumulative function $F(\Delta)$, (Eq. (26)): dotted line, and $M_1(\Delta)/M_1(\infty)$, (Eq. (27)): dashed line. $M_1(\infty)$ is the Bethe–Bloch value $x dE/dx$. The functions extend to the maximum energy loss $E_{\max} = 14,000$ keV.

The functions $f(\Delta; x, \beta\gamma)$, $F(\Delta; x, \beta\gamma)$ and $M_1(\Delta; x, \beta\gamma)$ for P10 gas are given in Fig. 18 and for Ne in Fig. 19. Clearly the use of $M_1(\Delta; x, \beta\gamma)$ cannot be expected to provide useful information about the parts of $f(\Delta)$ relevant for PID. When only part of the segment spectra is available for the energy loss calibration of a TPC, the use of $M_1(\Delta)$ would produce larger errors than the use of $f(\Delta)$ or $F(\Delta)$.

6. Straggling functions for particle tracks

The trajectory of a charged particle through a detector is called a *track*, with a length t . In principle the distribution in total energy loss along the track can be calculated with the convolution method (Section 4.3). Such functions are not useful for PID because of the long tail of large energy losses. Therefore, tracks are divided into *segments* of length

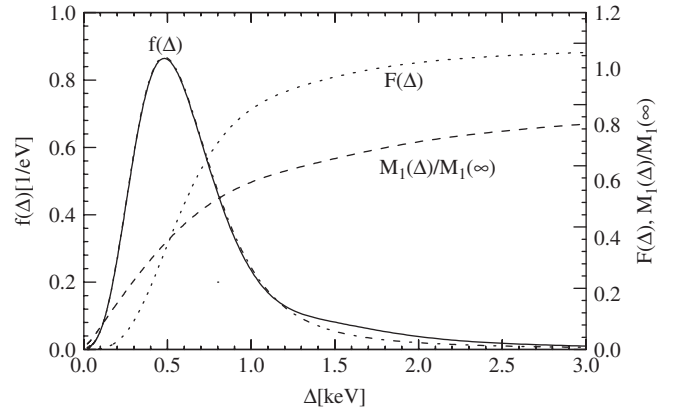


Fig. 19. Solid line: the straggling function $f(\Delta)$, (Eq. (20)), for particles with $\beta\gamma = 3.9$ traversing $x = 0.75$ cm of Ne. The straight part of the function between 1.4 and 2 keV is caused by energy losses to K-shell electrons ($I_K = 867$ eV). The mean free path for these collisions is 8 cm. The dashed-dotted line gives the function without these collisions. The cumulative functions $F(\Delta)$, (Eq. (26)): dotted line, and $M_1(\Delta)/M_1(\infty)$, (Eq. (27)): dashed line. $M_1(\infty) = 1.43$ keV/cm is the Bethe–Bloch value of $x \cdot dE/dx$. Also see Fig. J.3.

x , with the number of segments equal to $n_s = t/x$ and the ionization is recorded for each segment. For each track a compound “descriptor” (defined in Eq. (28)) is determined. Frequently used descriptors are the “truncated mean” and a likelihood number. Calculations of straggling functions for particle tracks are made for energy losses only.¹⁹

6.1. Calculations of specific energy losses Δ/x and descriptors C for tracks

A simulation of the energy losses along a particle track is made with a Monte Carlo calculation similar to the one described in Section 4.4, but rather than using energy losses for each collision a total energy loss Δ_i for each segment i is selected at random from the integral straggling function $F(\Delta; x, \beta\gamma)$ for segments, Eq. (26). For each track j the n_s values of Δ_i are assembled into a descriptor C_j . The primary descriptor used here is the truncated mean. To calculate the truncated mean C_j^{20} for track j , the n_s segment values Δ_i/x are sorted according to size and a reduced number $n_t = f_r n_s^{21}$ of the smallest segment values is summed and averaged²²

$$C_j = (1/n_t) \sum_1^{n_t} \frac{\Delta_i}{x}. \quad (28)$$

¹⁹In the measurements in a TPC the ADC output Q , equivalent to the ionization J in each segment, is measured and recorded, see Sections 1 and 9–11. Q is the result produced by the energy loss Δ , as described in Section 1.1.

²⁰In many publications C_j is designated as dE/dx . In Ref. [16] it is called an estimator $\langle S \rangle_\eta$.

²¹The optimum value of the “truncation fraction” f_r is between 0.5 and 0.7 and depends on the track geometry.

²²Calculations have been made for as many as 10^7 tracks. For each $\beta\gamma$ this takes about 80 s with a 2 GHz CPU.

The change of segment lengths x due to the curvature of the tracks, see Appendix D, is assumed to be negligible or averaged.²³ It is a disadvantage of the truncated mean that some information about the tracks is disregarded. On the other hand distortions in the registration of large energy losses will be unimportant. A great advantage is that no calculated straggling functions for segments are needed for the determination of C from experimental data.

The *likelihood* descriptor ζ is obtained by calculating the maximum value of the likelihood function [10, Eq. (45)]

$$L_j(\zeta) = \prod_{i=1}^{n_s} f(\Delta_i/\zeta; x, \beta\gamma) \quad (29)$$

where $f(\Delta_i; x, \beta\gamma)$ is the energy loss straggling function for a single segment for a selected $\beta\gamma$ [10]. The one-parameter scaling of Section 8.1 (Fig. 29) is implied here by the use of the factor ζ . In practice the logarithm of Eq. (29) is used

$$\ln L_j(\zeta) = \sum \ln f(\Delta_i/\zeta; x, \beta\gamma). \quad (30)$$

There are disadvantages to the likelihood method:

- (1) Straggling functions $f(\Delta; x, \beta\gamma)$ for segments must be known;
- (2) in a TPC large energy deposition values may be different from large energy losses, see Fig. 42; this might be remedied by replacing energy loss spectra $f(\Delta; x, \beta\gamma)$ in Eq. (30) by energy deposition spectra $g(D; x, \beta\gamma)$,²⁴
- (3) in Eq. (29) one-parameter scaling of the straggling functions is used, which does not take into account the change in shape implicit in Fig. 29 and explicit in Fig. 30.²⁵

Fig. 32 suggests that the determination of $L(\zeta)$ with two-parameters a and b might be a better method

$$\ln L_j(a, b) = \sum \ln f((\Delta_i - a)/b; x, \beta\gamma). \quad (31)$$

The likelihood method will not be considered further.

For a large number of tracks the truncated mean values C_j are binned and accumulated into a pdf or straggling function for tracks $f(C; \beta\gamma, t)$ as shown in Fig. 20 for a STAR TPC “reference track” consisting of 12 inner segments with $x = 12$ mm and 25 outer segments with $x = 20$ mm. This pdf has only a short tail of large energy losses and the moments M_ν , Eq. (13), specifically Eqs. (32) and (33) reach asymptotic values quickly and thus are useful.

²³Conceptually it would be preferable to use two-parameter scaling for Δ_i described in Section 8.2, Fig. 33. I have not tried to do this so far. The use of $\Delta_i/\Delta_p(x)$ (i.e. one-parameter scaling) did not change the resolution, Eq. (41) (Section 13.2).

²⁴The delta-ray escape would also have to be included.

²⁵This might cause problems in ALICE-TPC.

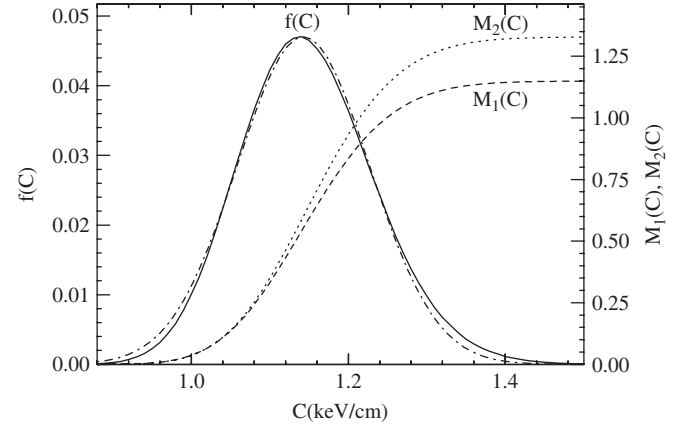


Fig. 20. The straggling functions $f(C)$ for truncated mean values C of STAR TPC reference tracks ($t = 64.4$ cm for particles with $\beta\gamma = 3.6$) in P10 gas: solid line. The cumulative functions are $M_1(C)$: dashed line, and $M_2(C)$: dotted line. The mean value for $0 < \Delta < 1.64$ keV is $\langle C \rangle = M_1(1.64 \text{ keV}) = 1.1491$ keV/cm, the second moment $M_2(1.64 \text{ keV})$ is 1.3279, and the standard deviation is $\sigma = 0.0861$ keV/cm or 7.5%. The most probable value is $C_p = 1.138$ keV/cm. A Gaussian fitted to $f(C)$ is given by the dashed-dotted line.

For ν tracks the moments are defined by²⁶

$$M_1 = \langle C \rangle = \sum_{j=1}^{\nu} \frac{C_j}{\nu}, \quad (32)$$

$$M_2 - M_1^2 = \sigma^2 = \sum_{j=1}^{\nu} \frac{C_j^2}{\nu} - \langle C \rangle^2. \quad (33)$$

The calculated straggling function for the reference track, the corresponding cumulative functions and a best-fit Gaussian are shown in Fig. 20. Other examples are given in Figs. 37–39 and 43–47. The relation between energy losses, energy deposition, measured ionization and ADC output Q in the TPC is discussed in Sections 1, 9, 10 and Appendix D. The corresponding functions for tracks are not calculated here because they depend on the geometry of the tracks inside the TPC and on corrections which are not well known.

6.2. Dependence of truncated mean values on track lengths and number of segments

For a PID analysis with truncated mean values, there will be a near periodic fluctuation of the values of $\langle C \rangle$ with the number of segments n_s caused by the rounding of $f_r n_s$ to an integer. Its period depends on the truncation fraction f_r . An example is shown in Fig. 21 for tracks in STAR-TPC composed of 12 inner and 10–32 outer segments, for $\beta\gamma = 3.6$ and $f_r = 0.7$. The σ of Eq. (33) is also given. The *overall* trend of $\langle C \rangle$ increasing with n_s depends on track composition. It is shown for $\beta\gamma = 0.5, 3.6$ and 15 in Fig. 22.

²⁶ $\langle C \rangle$ will be called an *average* value to avoid confusion with the *truncated mean* value C .

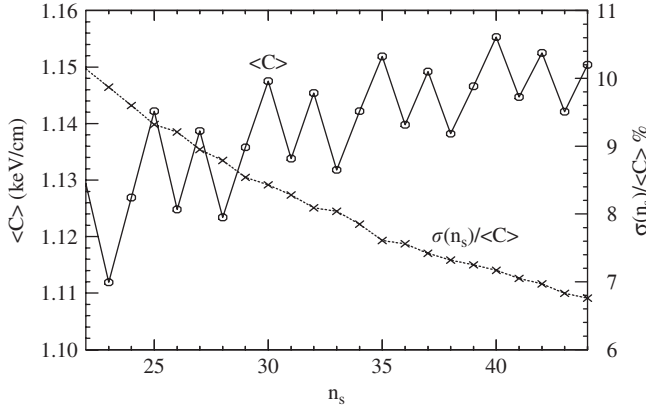


Fig. 21. Average values $\langle C \rangle$ of truncated ($f_r = 0.7$) mean values C for each track as function of the number n_s of segments in a track are shown by the symbol \circ . Lines are drawn to guide the eye. Track lengths are 34.4–78.4 cm. The standard deviation σ is given by \times . It can be approximated to $\pm 1\%$ by $\sigma(n_s) = 0.65/n_s^{0.563}$. The ratio $\sigma/\langle C \rangle$ decreases from 11.5% at $n_s = 22$ to 7.8% at $n_s = 44$. Besides the overall trend of $\langle C \rangle$ with n_s seen in Fig. 22 there are excursions of up to $\pm 1\%$ ($\pm 1.5\%$ for $n_s < 25$).

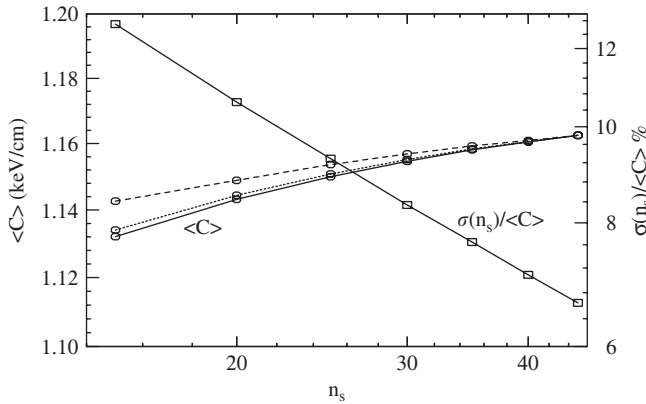


Fig. 22. Tracks selected for integer values of the truncation (10 inner segments and $(n_s - 10)$ outer segments, with $f_r = 0.6$). The average $\langle C \rangle$ is given for three particle speeds, normalized at $n_s = 45$. No excursions are seen. The points are connected by solid lines for $\beta\gamma = 3.6$, dotted lines for $\beta\gamma = 15$ and dashed lines for $\beta\gamma = 0.5$. The “resolution” $\sigma/\langle C \rangle$, Eq. (41), is given by the square symbols, also see Fig. 49.

The trend is the opposite for tracks consisting of outer segments only, $x = 2$ cm, shown in Fig. 23. The values are normalized at the highest n_s .

From Fig. 21 we see that $\langle C \rangle$ has an inherent uncertainty of about $\pm 1\%$ on top of the overall trend seen in Fig. 22. For the longer tracks $\langle C \rangle$ is almost constant and an average value can be used rather than the exact value for a given t . For Fig. 22, for $50 \leq t \leq 80$ cm the values of $\langle C \rangle$ deviate by only $\pm 0.3\%$ from the value $\langle C \rangle(t_0 = 62 \text{ cm}) = 1.158$. For Fig. 23 with $\langle C \rangle(t_0 = 50 \text{ cm}) = 1.193$ the same is the case for $40 \leq t \leq 70$ cm. In general the change of $\langle C \rangle$ with track length for $t > 20$ cm is a few %, but is about 5% for $10 < t < 20$ cm. The change of σ with t can be represented by

$$\sigma(t) = \sigma_0/t^s \quad (34)$$

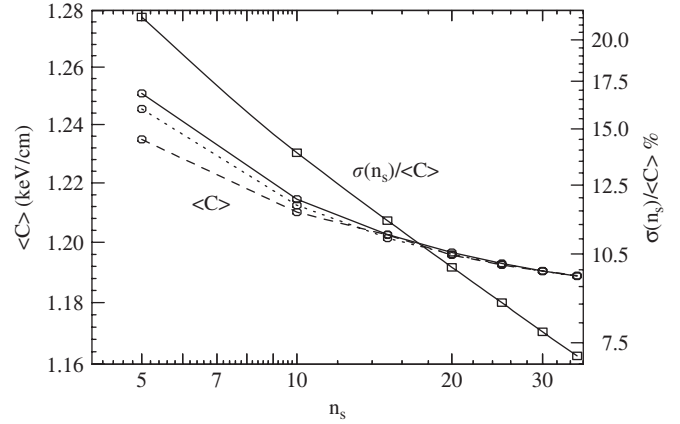


Fig. 23. Tracks consisting of outer segments only ($t = n_s \cdot 2$ cm). Otherwise same as Fig. 22.

where $0.45 < s < 0.55$. For Figs. 21 and 22 $s \sim 0.49$, for Fig. 23 $s \sim 0.53$. Values of $\langle C \rangle$ and σ for several track lengths and particle speeds are given in Table 3. The largest difference between two values of $\langle C \rangle$ is 10% at $\beta\gamma = 3.6$ for $t = 62$ cm and $t = 103.3$ cm.

7. Dependences of Δ_p , $\langle C \rangle$, σ_t and w on $\beta\gamma$ and gas pressure

7.1. Landau and Bethe–Bloch functions

It has been known for a long time and can be seen in Figs. 1, 2, 13 and 14 that the mean energy loss $\langle \Delta \rangle = xM_1$ is not a suitable quantity to describe straggling functions for thin absorbers. Thus the Bethe–Bloch expression giving M_1 (e.g. [1, Eq. (27.1)]) is not appropriate for the description of energy loss in thin absorbers. Attempts have been made to “parameterize” this function, e.g. with Eq. (24), such as to produce Δ_p . Landau [17] did point out that the most probable energy loss is the appropriate parameter. Based on the use of the Rutherford cross-section, Eq. (1), he gave an equation for the most probable energy loss

$${}_L A_p = \xi \left(\log \frac{\xi}{\varepsilon'} + 0.37 \right) \quad (35)$$

where $\xi = x \cdot k/\beta^2$, Eq. (1), $\varepsilon' = I^2/(2mc^2\beta^2\gamma^2)$, I is the logarithmic mean excitation energy of the absorber (Eq. (17) and [40]) and ε' is the E_{\min} of Eq. (22). For present purposes this can be written [18, 70, 71] as

$${}_L A_p(x; \beta) = \xi \left[\ln 2mc^2\beta^2\gamma^2 - \ln I + \ln \frac{\xi}{I} + 0.2000 - \beta^2 - \delta(\beta) \right] \quad (36)$$

where $\delta(\beta)$ represents the density effect correction.

This expression contains the segment length x in the logarithmic term, thus ${}_L A_p(\beta\gamma)/x$ depends on x , which qualitatively explains the behavior seen in Fig. 14. For

Table 3

Parameters for the STAR TPC tracks with 10 ($t = 20$ cm), 25 ($t = 50$ cm) outer segments, and with 10 inner segments and 25 outer segments ($x = 1.2$ and 2 cm for $t = 62$ cm, $x = 2$ and 3.33 cm for $t = 103.3$ cm). Units for $\langle C \rangle$ and σ are keV/cm

t	20 cm		50 cm		62 cm		103.3 cm	
	$\langle C \rangle$	σ						
$\beta\gamma$								
0.5	5.183	0.5352	5.108	0.3190	4.996	0.2726	5.321	0.2532
3.6	1.214	0.1686	1.193	0.1019	1.158	0.0886	1.274	0.0805
15	1.383	0.1800	1.360	0.1092	1.323	0.0830	1.452	0.0857

$\beta\gamma > 500$ in Si Eq. (36) is valid to $\pm 1\%$ for $x > 80 \mu\text{m}$, see Ref. [18, Table V], but $w_L = 4\xi$ [2] is too small for $x < 1$ cm [18, Fig. 15]. Eq. (36) is not practical to use because it requires a separate calculation of $\delta(\beta)$.

7.2. Bichsel functions

The Landau function ${}_L\Delta_p(\beta\gamma)$ is an approximation which does not include factors related to atomic structure, such as seen in Figs. 5, 6 and G.2. A more realistic dependence of Δ_p on x and $\beta\gamma$ must be obtained with the FVP or the B–F cross-sections. Such calculations have been made and results are given here, also see Ref. [26]. Note that the density effect $\delta(\beta\gamma)$ is calculated implicitly in Eq. (7). Functions $\Delta_p(\beta\gamma; x)$ for single segments of Si have been given in Ref. [1, Fig. 27.7]. Functions for single segments with several lengths x in P10 are given in Fig. 24. The same functions scaled to 1.00 at $\beta\gamma \sim 3.5$ are given in Fig. 25. A decrease of the relativistic rise of Δ_p/x with increasing segment length x is seen. I have not found a simple explanation for this effect. It is similar to the measured decrease found with increasing gas pressure [16, Fig. 1.20] (some of the decrease is due to the effect shown in Fig. 16). Other examples can be found in Refs. [71,72].

For tracks, the functions calculated are for average values $\langle C(\beta\gamma; t, f_r) \rangle$ of the spectra, Eq. (32), where f_r is the truncation fraction. Examples for P10 are given in Fig. 26 and in Table 5. The variations of $\langle C \rangle$ with t at a given particle speed are described in Section 6.2.

The influence of the atomic structure on the dependence on particle speed can be seen in comparisons with Landau functions. They are shown for Ar in Fig. 27 and for Si in Fig. 28. The analytic expression $F_g(v)$ given as Eq. (9.5) in Ref. [16] has five parameters which will be enough to fit any of the functions given here (see Eq. J.1).

Note the large change in the “relativistic rise” of $\Sigma_t(\beta\gamma)$ with density:

- For Si, $\Sigma_t(\beta\gamma)$ is constant to 0.1% for $\beta\gamma > 16$ (the minimum);
- for P10 the relativistic rise is about 36% from $\beta\gamma \sim 4$ to 10,000;
- for Ne it is about 47% for the same range of $\beta\gamma$ (Table 2 and Fig. 25).

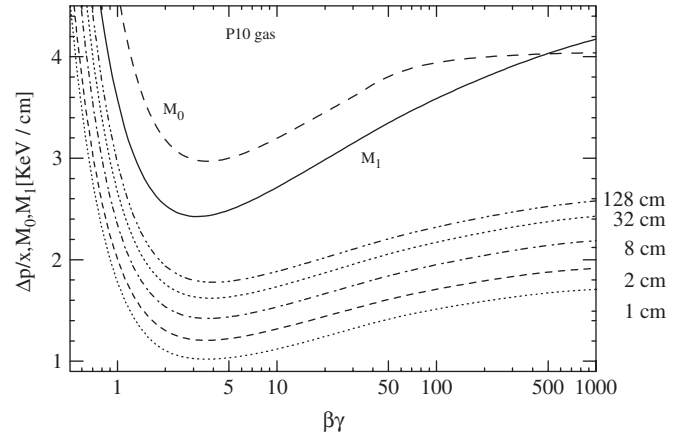


Fig. 24. The dependence of Δ_p/x (Bichsel functions) on $\beta\gamma$ for segments of several lengths x (Table 2). Segment lengths x are marked at right. The long-dashed line gives the Bethe macroscopic CCS $M_0/10$ (collisions/cm), the solid line gives the Bethe $dE/dx = M_1(\beta\gamma)$ (Eq. (13)).

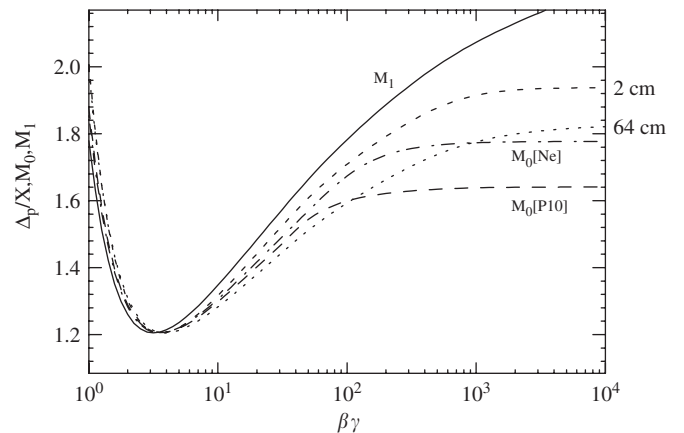


Fig. 25. Solid line: the dependence of the Bethe $M_1(\beta\gamma) = dE/dx$ on $\beta\gamma$, Eq. (13). Dotted and short dashed lines: Δ_p/x for segments of length $x = 2$ cm and $x = 64$ cm in P10. Long dashed and dash dotted lines: $M_0(\beta\gamma)$ for P10 and Ne. All functions are normalized to the function Δ_p/x for $x = 2$ cm. The difference in M_1 for P10 and Ne is small.

8. Scaling of straggling functions

As mentioned in Section 4.3 the similarity of straggling functions can be used to reduce the number of tabulated functions needed for a given purpose such as the PID proposed in Section 13.3. This can be done with *scaling*

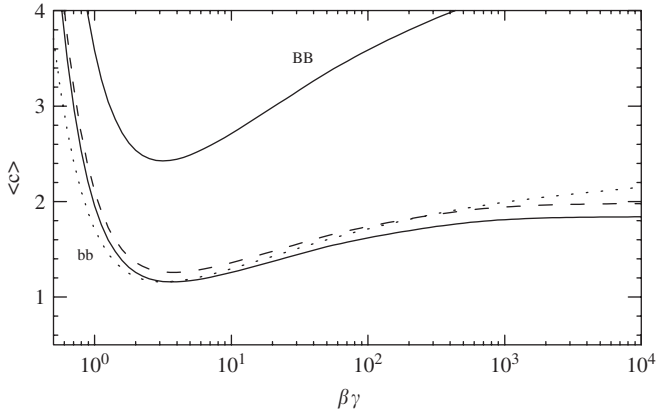


Fig. 26. The dependence of $\langle C \rangle$ for tracks with length t ($f_r = 0.60$) on particle speed $\beta\gamma$ in P10. The Bethe–Bloch function dE/dx is given by the line labeled BB. The same function scaled to the minimum value of the reference function is the dotted line labeled bb. Two Bichsel functions are given. Solid line: reference track $t = 64.4$ cm (12 inner segments with $x = 1.2$ cm and 25 outer segments with $x = 2$ cm). Dashed line: slanted track with $t = 107$ cm consisting of 12 inner segments with $x = 2$ cm and 25 outer segments with $x = 3.333$ cm. A track with $t = 34.4$ cm (12 inner and 10 outer segments) is not shown, on the average it is 1.5% below the reference track (see Fig. 22, Section 6.2). More details on the variation with track length are given in Section 6.2.

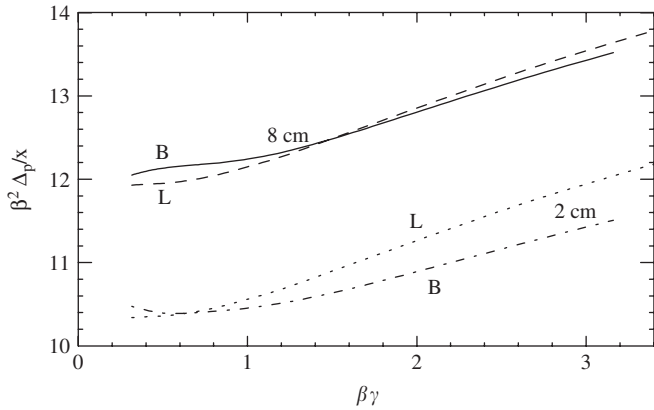


Fig. 27. Comparison of Landau Δ_p/x as function of $\beta\gamma$ (the lines are labeled L), Eq. (35) or (36), and Bichsel values (labeled B) for Ar, $x = 2$ cm and $x = 8$ cm. The separation between functions for L is constant, while it increases with $\beta\gamma$ for B.

which is explored in this section. For straggling functions calculated with the Rutherford spectrum it was shown by Landau [17] that a single function $\phi(\lambda)$ [2] can represent all functions $f_L(\Delta; \beta, x)$ with the relation

$$\lambda = \Delta/\xi - a_L(\beta; x) \quad \text{specifically } a_L(\beta; x) = \ln \xi/\epsilon' + 0.423 \quad (37)$$

where ξ and ϵ' are defined below Eq. (35) and the peak of $\phi(\lambda)$ is at $\lambda_p = -0.222$. As seen in Appendix G, straggling functions for segments evolve with segment length from complex forms into unimodal smooth functions, also see [5]. For P10 this occurs at approximately 15 mm ($m_c \sim 45$), Fig. G.2. For $x > 15$ mm, straggling functions for increas-

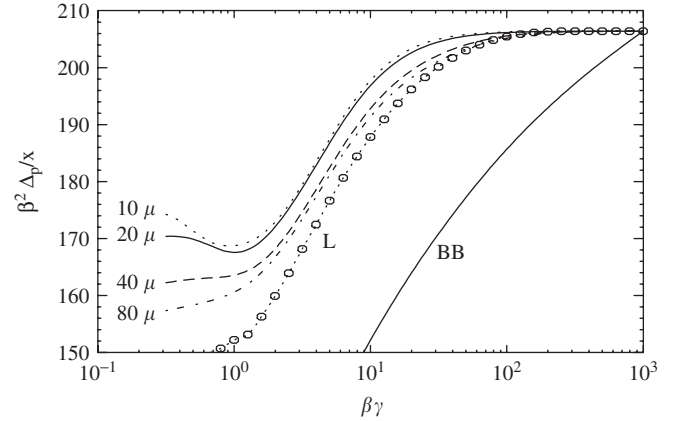


Fig. 28. Comparison of Bethe–Bloch BB, Landau L (for $x = 10 \mu\text{m}$) and Bichsel functions for Δ_p/x for thin Si absorbers.

ing x are similar in shape. For a given particle speed this follows from the similarity of the multiple collision spectra seen in Figs. 11 and 12 and the similarity for large m_c of the Poisson distributions Eqs. (18) and (20). Similarity can also be expected for different particle speeds because of the similarity of the single CCS seen in Figs. 8 and 9. For the comparison of experimental data for segments with calculations, scaling can reduce the number of tables needed. The principle is to use a few tables of “reference functions” for suitable $\beta\gamma$ and x , then scale abscissas and ordinates for other $\beta\gamma$ and x .

Scaling may be useful for simulations for curved tracks. For studies exploring the scaling relations the ab initio calculations of straggling functions must be used. One- and two-parameter scaling are compared in this section. One-parameter scaling is not a suitable approximation in principle, Eq. (37). It is shown here because it has been used heretofore, e.g. for the maximum likelihood calculations, Eq. (29).

Scaling for tracks will give better approximations than for segments. In the examples shown in Figs. 36–41 the abscissas for different functions are scaled to that of a *single reference function*, shown by the solid line. for the STAR TPC the “reference track” is for $\beta\gamma = 3.6$, and consists of 12 inner segments with $x = 12$ mm and 25 outer segments with $x = 20$ mm for a track length $t = 64.4$ cm, see Fig. 20. To show the similarities in shape clearly, the ordinate scale is chosen such that the peaks are at the same ordinate.

8.1. One-parameter scaling

Obtaining straggling functions for tracks, $f(C; t, \beta\gamma)$, from a reference straggling function $f(C; t, (\beta\gamma)_0)$, is implemented by multiplying the scale of the independent variable C by a factor $b(\beta\gamma)$.

For one-parameter scaling of *tracks* with fixed t , the ratio of the mean values can be used: $b(\beta\gamma) = \langle C(\beta\gamma) \rangle / \langle C((\beta\gamma)_0) \rangle$, Table 5. Examples are shown for tracks with

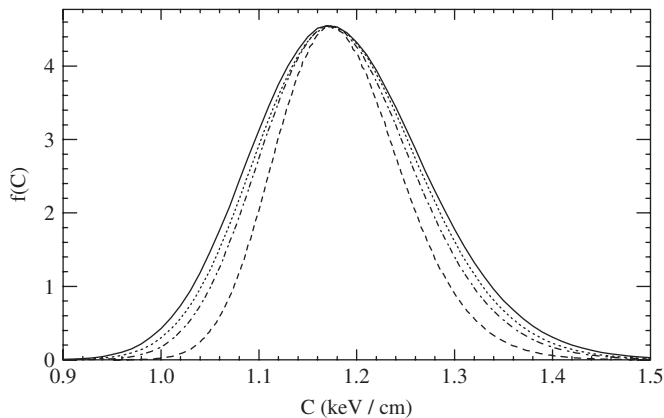


Fig. 29. One-parameter scaling for straggling functions $f(C)$ for particles with different speeds traversing tracks with $t = 32 \times 2$ cm of P10. The solid line is for $\beta\gamma = 3.6$, the dashed line for $\beta\gamma = 0.5$, the dashed-dotted line for $\beta\gamma = 1$, the dotted line for $\beta\gamma = 15$. The functions have been scaled to coincide at the peak. Abscissa values C are for $\beta\gamma = 3.6$. Values for $\langle C \rangle$ are in Table 5. The scaling factor $b(\beta\gamma)$ is defined in the text.

32 segments of $x = 2$ cm in Fig. 29. The functions are different in shape because the scaled FWHM w are different. Thus the use of one-parameter scaling would lead to errors.

The differences are less for $(\beta\gamma) > (\beta\gamma)_0 \sim 3.6$, and the use of the maximum likelihood calculations, Eq. (30), in e.g. NA49 was not as compromised as it is for STAR-TPC.

A second example is the comparison for segments of $x = 7.5$ mm in neon in Fig. 30. The shapes are quite different due to the difference in m_c , Appendix G. It would be difficult to *experimentally measure* the shapes of these functions accurately [73].²⁷ On the other hand, for tracks with $x = 7.5$ mm segments I have found no serious problems for PID calculations with truncated means, but have not made calculations with the maximum likelihood approach [74].

8.2. Two-parameter scaling for segments

The next approximation is two-parameter scaling. In order to see how good this approximation can be, the following procedure is used. For a given x consider two cumulative straggling functions $F_1(\Delta; x, [\beta\gamma]_1)$ and $F_2(\Delta; x, [\beta\gamma]_2)$. Find the values Δ_1 and Δ_2 for which $F_1(\Delta_1; x, [\beta\gamma]_1)$ and $F_2(\Delta_2; x, [\beta\gamma]_2)$ are equal, and make the graph of Δ_2 versus Δ_1 , called a “scaling relation”. Examples for $x = 2$ cm in Ar are shown in Fig. 31. The lines seen can be approximated by straight lines $\Delta_2 = a + b \cdot \Delta_1$. Two-parameters, a and b , are needed. For TPC calibrations with segments (Sections 11 and 14) the most important part of the straggling functions is in the region $\Delta_l < \Delta < \Delta_u$ (Fig. 13) and the straight line can be

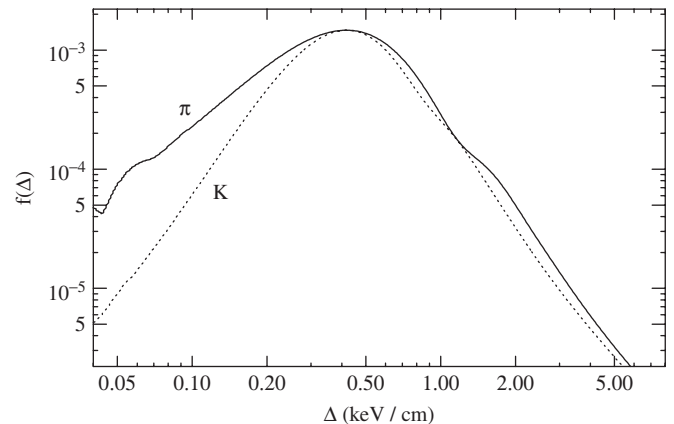


Fig. 30. One-parameter scaling for straggling functions $f(\Delta)$ for $pc = 500$ MeV pions and kaons traversing $x = 7.5$ mm of Ne. The abscissa for the kaon-function has been scaled so that its peak coincides with the pion-peak. The shapes differ considerably, mainly due to the difference in the mean numbers of collisions, Eq. (20), $m_c(\pi) = 8$, $m_c(K) = 12$, also see Appendix G.

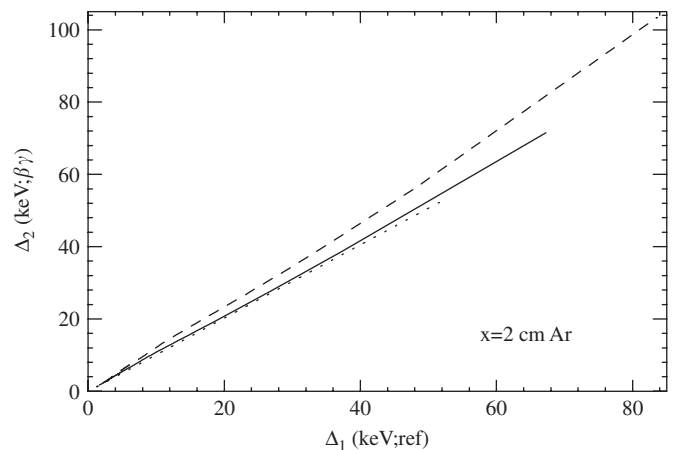


Fig. 31. Scaling relation between the abscissa values for common values of the cumulative functions $F(\Delta; \beta\gamma)$ for segments, Fig. 13, for different particle speeds, see text. For two-parameter scaling the lines are approximated by straight lines $\Delta_2 = a + b \cdot \Delta_1$. The abscissa Δ_1 is for a reference function with $\beta\gamma = 3.7$. Solid line: $\beta\gamma = 1.43$, dotted line: $\beta\gamma = 4.3$, dashed line: $\beta\gamma = 1.0$.

chosen through these two points (which define FWHM). Then b is the ratio of the FWHM, $b = w_2/w_1$.²⁸

A comparison of straggling functions with different $\beta\gamma$ for $x = 2$ cm in P10 scaled with this linear relation is shown in Fig. 32, with details given in Table 4. The same scaling method can be used for the dependence on *segment length*. A comparison for $\beta\gamma = 4.3$ is given in Fig. 33. Examples of the dependence on $\beta\gamma$ for Si-detectors are shown for thickness $x = 300 \mu\text{m}$, Fig. 34 and $x = 8 \mu\text{m}$, Fig. 35. Evidently two-parameter scaling of segments is useful for track simulations if the truncated mean is used but probably should not be used for likelihood simulations (Section 6.1).

²⁷For the innermost section of ALICE-TPC this must be kept in mind.

²⁸For tracks, points farther apart might be more suitable (Figs. 37 and 38).

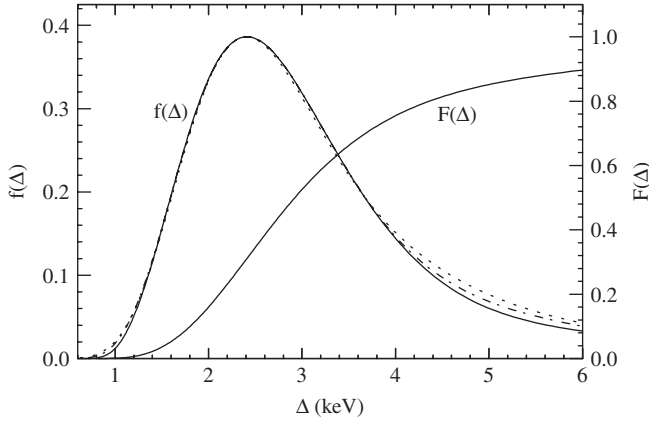


Fig. 32. Two-parameter scaled straggling functions $f(\Delta)$ for segment length $x = 2$ cm in P10 gas. Solid line: $\beta\gamma = 3.7$, dash-dotted line: $\beta\gamma = 1.2$ and dotted line: $\beta\gamma = 0.7$. Ordinate and abscissa scales are for $\beta\gamma = 3.7$. The abscissae for other $\beta\gamma$ are $\Delta(\beta\gamma) = a(\beta\gamma) + b(\beta\gamma) \cdot \Delta(3.7)$. The cumulative function $F(\Delta; 3.7)$ is also shown. The value $F(\Delta) = 0.7$ which is used to calculate the truncated mean for tracks is reached at $\Delta \sim 3.8$: the differences between the functions $f(\Delta)$ for $\Delta > 3.8$ keV are not important, see Table 4.

Table 4

Parameters Δ_ℓ , w , Δ_p , $f(\Delta_p)$ of the segment straggling functions $f(\Delta; \beta\gamma)$ for $x = 2$ cm (calculated with Eq. (20)) shown in Fig. 32

$\beta\gamma$	Δ_ℓ	w	b	a	Δ_p	$f(\Delta_p)$
3.7	1.5925	2.0798	1.0	0	2.4100	0.3862
2.2	1.6916	2.1530	1.0352	0.043	2.5360	0.3700
1.2	2.3869	2.6026	1.2514	0.3941	3.4149	0.2984
0.7	4.5415	3.9403	1.8945	1.5245	6.0788	0.1929

The scaling factors are calculated with $b = w(\beta\gamma)/w(3.7)$, $a = \Delta_\ell(\beta\gamma) - b \cdot \Delta_\ell(3.7)$. The scaled values $\Delta_p = a + b \cdot 2.410$ calculated with scaling will differ slightly from the values in the table because of the curvature of the lines in Fig. 31. The scaled values $f(\Delta_p(3.7)/b(\beta\gamma))$ differ by up to 6% from those in the table.

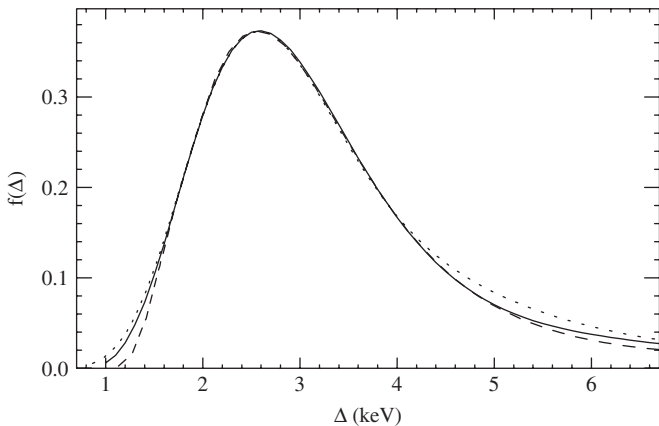


Fig. 33. Scaled straggling functions for P10 for particles with $\beta\gamma = 4.3$ for several segment lengths x . Two-parameter scaling is used so that Δ_ℓ and Δ_u coincide (see Fig. 13). Solid line: $x = 2$ cm, dotted line: 4 cm, dashed line: 1.2 cm. The function for $x = 8$ cm agrees within line width with that for 4 cm. See description given for Fig. 32. The variations in shape are due to the evolution of $f(\Delta)$ shown in Appendix G.

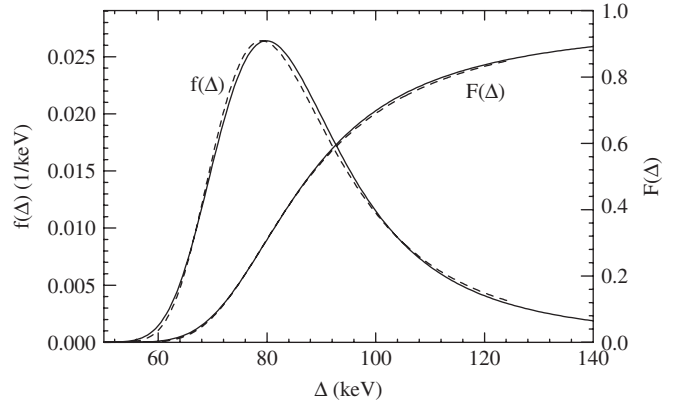


Fig. 34. Two-parameter scaled straggling functions $f(\Delta)$ and $F(\Delta)$ for $x = 300 \mu\text{m}$ Si for $\beta\gamma = 10$: solid line, $\beta\gamma = 1$: dashed line. Functions for $1 < \beta\gamma < 10$ lie between the lines shown. No amplifier noise is included. The abscissa scale is for $\beta\gamma = 10$.

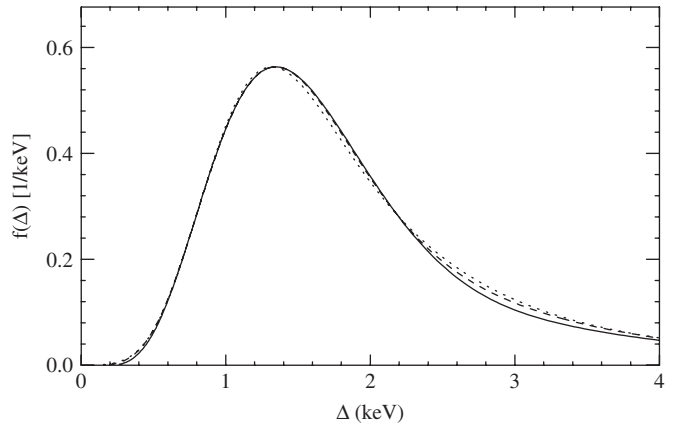


Fig. 35. Two-parameter scaled straggling functions $f(\Delta)$ for $x = 8 \mu\text{m}$ Si for particles with different $\beta\gamma$. Solid line: $4 \leq \beta\gamma \leq 20$. Dashed line: $\beta\gamma = 1.2$, dotted line: 0.7.

8.3. Two-parameter scaling for tracks

For straggling functions obtained with the truncated mean for a track the scaling relation for $f(C_2; \beta_2, t_2)$ relative to $f(C_1; \beta_1, t_1)$ is

$$C_2(\beta_2, t_2) = a(\beta_2, t_2) + b(\beta_2, t_2) \cdot C_1(\beta_1, t_1). \quad (38)$$

The approximation made with two-parameter scaling can be assessed from the plot of the values C_1 and C_2 obtained for equal values from $F(C_2; \beta_2, t_2) = F(C_1; \beta_1, t_1)$. Such functions are shown in Fig. 36 for $\beta_2 = \beta_1$, $t_1 = 64.4$ cm (the STAR reference track) and for $t_2 = 38.4, 50.4, 74.4$ cm. The values of a and b were calculated for $F_{1,2} = 0.1$ and $F_{1,2} = 0.9$ rather than the FWHM values. The corresponding straggling functions $f(C_2; 3.6, t_2)$ scaled to $f(C; 3.6, 64.4 \text{ cm})$ are shown in Figs. 37 and 38. Close agreement is seen. The scaling with particle speed for a fixed track length $t = 64$ cm is given by the functions $f(C_2; 15, 64)$ and $f(C_1; 0.5, 64)$ shown in Fig. 39.

The scaling coefficients for all speeds for $t = 40$ cm and $t = 62$ cm are given in Table 5. Only one reference function,

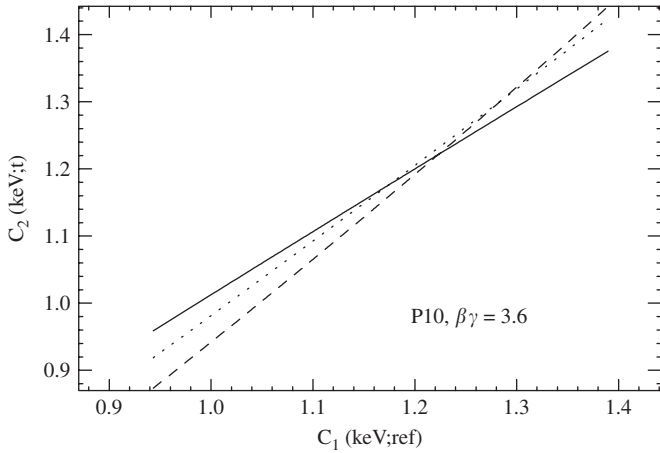


Fig. 36. Scaling relations Eq. (38) relative to the reference track ($t = 64.4$ cm). Solid line $t_2 = 74.4$ cm, dotted line $t_2 = 50.4$ cm, dashed line $t_2 = 38.4$ cm.

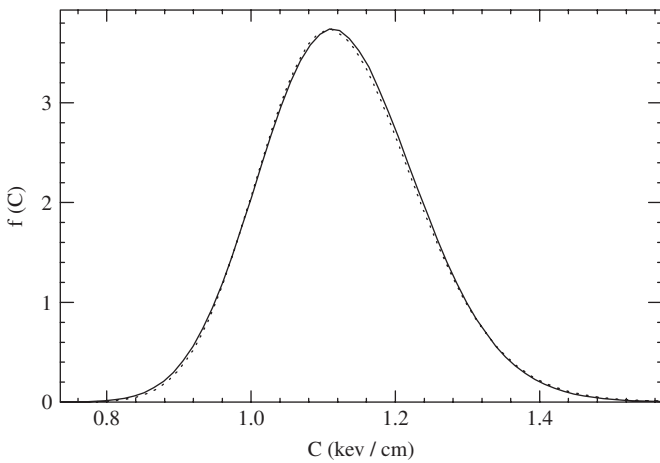


Fig. 37. Straggling functions for tracks of different lengths in P10 gas for $\beta\gamma = 3.6$ scaled with two parameters to the reference function $t = 64.4$ cm, which is shown by the solid line. Functions for track lengths $t = 74.4$ cm and $t = 103.3$ cm agree with this function within the linewidth. Tracks with $t = 38.4$ cm are represented by the dotted line. The truncation factor is $f_r = 0.6$, see Table 5.

$f(C; 3.6, 64.4)$, is needed to produce good approximations for a wide range of t and $\beta\gamma$. For short tracks consisting of outer segments only and for $\beta\gamma < 1$, scaling to the reference track does not give good results. This is evident from the scaling relation shown in Fig. 40 and for the $f(C)$ in Fig. 41. For short tracks and small $\beta\gamma$ different reference functions are needed.

8.4. Practical implementation

Because of differences in parameters and shapes of scaled functions seen in Figs. 30, 32, 33, 35, G.1 and G.2 scaling for segments must be used judiciously. For fairly long tracks the differences are smaller, Figs. 21–23, 34, 37–39, and if an uncertainty of $\pm 1\%$ for $\langle C \rangle$ and σ is acceptable, common scaling coefficients a and b can be

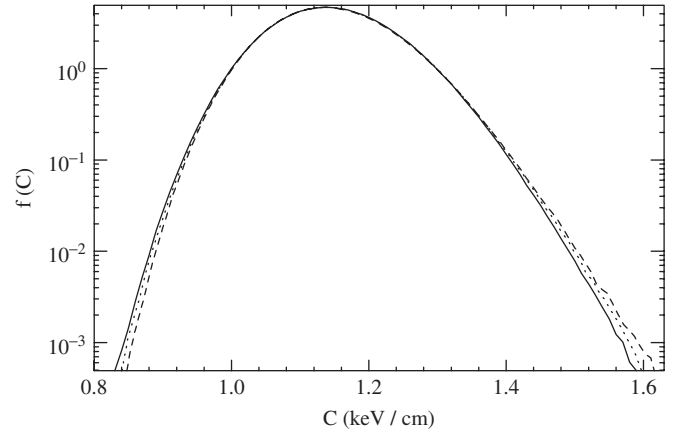


Fig. 38. Same as Fig. 37, but with logarithmic ordinate. Solid line: reference function ($t = 64.4$ cm); dotted line: $t = 50.4$ cm, dashed line: $t = 38.4$ cm. The functions for $t = 74.4$ cm and $t = 103.3$ cm differ from the reference function by at most a linewidth. The differences in the tails are the residuals of the effects described in Appendix G.

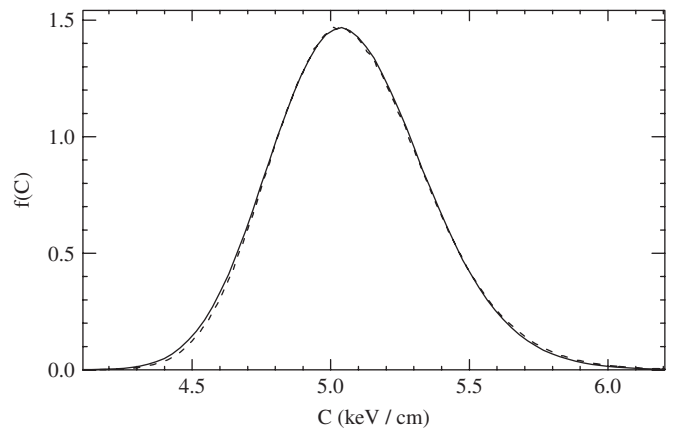


Fig. 39. Straggling function $f(C)$ for P10 for track length $t = 64$ cm (outer segments only) and two particle speeds, solid line: $\beta\gamma = 15$, dashed line: $\beta\gamma = 0.5$. Two-parameter scaling is used. The reference track as well as all functions for $0.5 < \beta\gamma < 15$ lie between the two lines.

used for a range of track lengths t , as outlined in Section 6.2, based on Figs. 21–23.

For STAR-TPC to scale to the single reference track $f(C; 64.4 \text{ cm}, \beta\gamma = 3.6)$ such coefficients are given in Table 5 for tracks with $t = 40$ cm (20 outer segments with $x = 2$ cm) and $t = 62$ cm (10 inner segments and 25 outer segments). The parameters C_r , a and b in the tables are then valid for $30 \leq t \leq 60$ cm and $50 \leq t \leq 80$ cm. For σ the approximation with Eq. (34) in Section 6.2 can be used. For short tracks, Fig. 41, scaling must be used with caution. We see from Fig. 29 that one-parameter scaling for segments should not be used. Two-parameter scaling for segments, Figs. 32 and 33, may be adequate for some applications (e.g. track calculations with the use of truncated means), but for accurate calculations the original functions should be used.

Table 5

Mean values $\langle C \rangle$ of truncated mean track descriptors C , $f_r = 0.6$, their standard deviations σ and scaling coefficients a and b for tracks of length $t = 20 \times 2$ cm (left 4 cols., Fig. 23) and $t = (10 \times 1.2 + 25 \times 2)$ cm (right 4 cols., Fig. 22) in P10 gas as function of particle speed $\beta\gamma$

$\beta\gamma$	$t = 40$ cm				$t = 62$ cm			
	$\langle C \rangle$	σ	a	b	$\langle C \rangle$	σ	a	b
0.400	7.4618	0.4911	1.0790	5.4988	7.2927	0.3688	2.4176	4.1969
0.440	6.3363	0.4246	0.7535	4.8085	6.1860	0.3200	1.9194	3.6732
0.484	5.4010	0.3739	0.5002	4.2222	5.2699	0.2844	1.5270	3.2230
0.532	4.6299	0.3304	0.3060	3.7252	4.5134	0.2519	1.2127	2.8426
0.586	3.9915	0.2947	0.1561	3.3051	3.8898	0.2226	0.9586	2.5251
0.644	3.4664	0.2615	0.0446	2.9489	3.3754	0.1982	0.7585	2.2542
0.709	3.0319	0.2361	-0.0372	2.6455	2.9510	0.1794	0.6036	2.0227
0.779	2.6753	0.2139	-0.1048	2.3965	2.6024	0.1624	0.4726	1.8355
0.857	2.3817	0.1954	-0.1571	2.1892	2.3154	0.1486	0.3658	1.6807
0.943	2.1416	0.1797	-0.1900	2.0105	2.0800	0.1371	0.2848	1.5479
1.037	1.9443	0.1672	-0.2242	1.8702	1.8877	0.1276	0.2179	1.4400
1.141	1.7831	0.1561	-0.2452	1.7498	1.7300	0.1196	0.1650	1.3497
1.255	1.6517	0.1473	-0.2612	1.6500	1.6018	0.1128	0.1237	1.2754
1.381	1.5451	0.1400	-0.2765	1.5716	1.4979	0.1075	0.0886	1.2160
1.519	1.4596	0.1340	-0.2861	1.5059	1.4143	0.1031	0.0647	1.1646
1.671	1.3907	0.1290	-0.2883	1.4489	1.3470	0.0993	0.0461	1.1228
1.838	1.3359	0.1254	-0.2973	1.4097	1.2939	0.0963	0.0265	1.0941
2.022	1.2933	0.1222	-0.2999	1.3750	1.2521	0.0940	0.0213	1.0624
2.224	1.2608	0.1198	-0.3000	1.3472	1.2202	0.0923	0.0088	1.0459
2.446	1.2360	0.1181	-0.3019	1.3276	1.1963	0.0909	0.0070	1.0267
2.691	1.2185	0.1167	-0.3029	1.3131	1.1792	0.0900	0.0010	1.0173
2.960	1.2066	0.1155	-0.3003	1.3007	1.1678	0.0892	0.0000	1.0084
3.256	1.1999	0.1151	-0.2990	1.2941	1.1610	0.0886	0.0016	1.0012
3.582	1.1967	0.1146	-0.2928	1.2856	1.1580	0.0884	0.0014	0.9989
3.940	1.1970	0.1144	-0.2919	1.2851	1.1586	0.0885	0.0009	0.9997
4.334	1.2002	0.1144	-0.2894	1.2859	1.1618	0.0885	0.0045	0.9994
4.767	1.2057	0.1147	-0.2895	1.2904	1.1675	0.0886	0.0070	1.0020
5.244	1.2135	0.1151	-0.2861	1.2944	1.1748	0.0888	0.0090	1.0066
Higher $\beta\gamma$								
5.000	1.2094	0.1147	-0.2856	1.2906	1.1708	0.0888	0.0098	1.0025
6.050	1.2279	0.1157	-0.2809	1.3022	1.1891	0.0895	0.0183	1.0108
7.321	1.2512	0.1169	-0.2713	1.3140	1.2123	0.0904	0.0274	1.0232
8.858	1.2786	0.1183	-0.2633	1.3307	1.2390	0.0916	0.0365	1.0380
10.718	1.3081	0.1199	-0.2540	1.3479	1.2681	0.0928	0.0514	1.0504
12.969	1.3396	0.1215	-0.2452	1.3676	1.2989	0.0941	0.0652	1.0650
15.692	1.3717	0.1231	-0.2328	1.3845	1.3308	0.0955	0.0813	1.0783
18.987	1.4048	0.1250	-0.2251	1.4064	1.3633	0.0969	0.0917	1.0975
22.975	1.4379	0.1267	-0.2156	1.4266	1.3960	0.0983	0.1076	1.1117
27.800	1.4714	0.1284	-0.2055	1.4466	1.4286	0.0997	0.1187	1.1303
33.637	1.5045	0.1305	-0.1970	1.4674	1.4612	0.1012	0.1322	1.1465
40.701	1.5376	0.1320	-0.1897	1.4900	1.4937	0.1025	0.1471	1.1617
49.249	1.5683	0.1338	-0.1787	1.5066	1.5241	0.1040	0.1581	1.1785
59.591	1.5969	0.1355	-0.1718	1.5255	1.5523	0.1054	0.1696	1.1929
72.105	1.6239	0.1370	-0.1720	1.5486	1.5784	0.1067	0.1765	1.2091
87.247	1.6487	0.1387	-0.1635	1.5628	1.6028	0.1081	0.1853	1.2227
105.569	1.6719	0.1407	-0.1639	1.5831	1.6258	0.1094	0.1908	1.2378
127.738	1.6944	0.1422	-0.1661	1.6046	1.6476	0.1107	0.1954	1.2526
154.563	1.7161	0.1437	-0.1623	1.6197	1.6685	0.1120	0.2012	1.2654
187.022	1.7361	0.1455	-0.1664	1.6401	1.6885	0.1133	0.2029	1.2810
226.296	1.7558	0.1472	-0.1663	1.6571	1.7075	0.1145	0.2044	1.2960
273.818	1.7742	0.1484	-0.1659	1.6729	1.7255	0.1157	0.2092	1.3075
331.320	1.7919	0.1501	-0.1713	1.6926	1.7423	0.1168	0.2095	1.3215
400.898	1.8077	0.1514	-0.1655	1.7011	1.7578	0.1179	0.2104	1.3344
485.086	1.8221	0.1528	-0.1746	1.7213	1.7719	0.1189	0.2114	1.3454
586.954	1.8350	0.1540	-0.1756	1.7329	1.7845	0.1199	0.2079	1.3593
710.215	1.8461	0.1552	-0.1852	1.7512	1.7953	0.1208	0.2083	1.3681
859.360	1.8557	0.1565	-0.1893	1.7631	1.8044	0.1216	0.2090	1.3755
1039.825	1.8635	0.1572	-0.1924	1.7724	1.8118	0.1223	0.2067	1.3839
1258.189	1.8699	0.1576	-0.1962	1.7807	1.8178	0.1228	0.2043	1.3910
1522.408	1.8750	0.1585	-0.1962	1.7857	1.8227	0.1233	0.2056	1.3943

Values for $\langle C \rangle$, σ and a are in keV/cm. The scaling parameters are in relation to the reference track $t = 64.4$ cm (12×12 mm + 25×20 mm) and $\beta\gamma = 3.6$. The variation of C due to the Monte Carlo calculation is of the order of ± 0.005 for a and b , ± 0.001 for $\langle C \rangle$ and σ . Therefore, *linear interpolation* between adjacent values should be used. For both t the coefficient b is within $\pm 1\%$ equal to the ratio σ/σ_r where $\sigma_r = 0.0885$ keV/cm. See Section 8.4 for practical use.

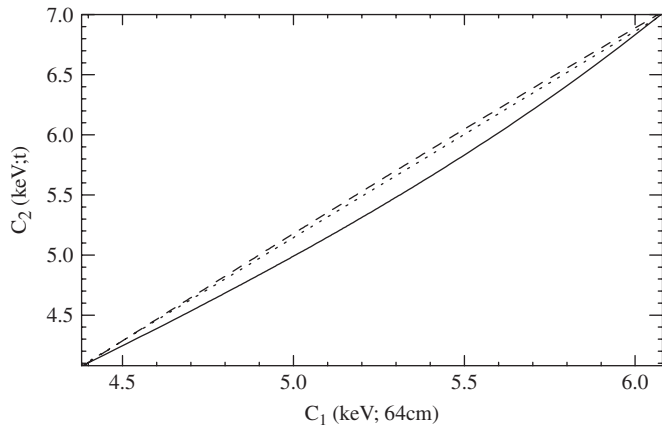


Fig. 40. Scaling relations for $\beta\gamma = 0.5$ for tracks consisting of outer segments only, for two track lengths relative to a track of $t = 25 \times 2$ cm. Solid line: $t = 20$ cm, dashed line: $t = 64$ cm. To show the curvature of these lines, a dotted straight line is given.

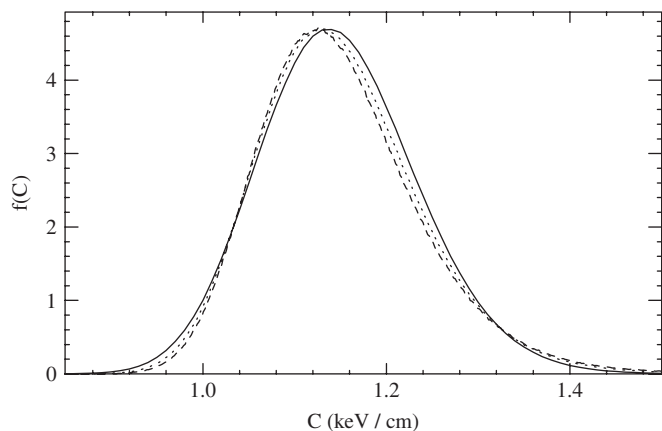


Fig. 41. Two-parameter-scaled straggling functions for P10 for one track length $t = 20$ cm for two particle speeds relative to the reference track ($\beta\gamma = 3.6$, $t = 64.4$ cm): solid line. Dashed line: $\beta\gamma = 0.5$, dotted line: $\beta\gamma = 15$. Evidently different reference functions are needed for short tracks.

The implementation of scaling consists of reading a reference table [26] of C_r , $f(C_r)$ and $F(C_r)$ (which is for $\beta\gamma = 3.6$), select another value of $\beta\gamma$ and read $a(\beta\gamma)$ and $b(\beta\gamma)$ from Table 5. The values of C for this $\beta\gamma$ are $C(\beta\gamma) = a(\beta\gamma) + b(\beta\gamma) \times C_r$. In the new table C_r is replaced by $C(\beta\gamma)$, and $f(C_r)$ and $F(C_r)$ remain the same.

The functions for arbitrary (or selected) values of $C(\beta\gamma)$ can be calculated with e.g. a cubic spline interpolation [75, p. 86].

9. Energy loss, energy deposition and ionization

It must be understood that in each stage of the conversion of energy loss Δ into the ADC output Q , described in Section 1, a change in shape of the p.d.f.s and therefore also in the most probable values Δ_p and FWHM w will occur. These changes are described for TPCs in Sections 9 and 10. A more detailed description has been

given by Lapique and Piuz [79]. For Si detectors they are described in Ref. [14].

In the geometry of the STAR TPC [11,12] the z -direction is defined by the central axis of the TPC which is also the direction of travel of the heavy ions. Reaction products are emitted in all directions, Fig. 3 in Ref. [12] and traverse a variety of track lengths.²⁹ The full trajectory of a particle with $pc > 1.5$ GeV emitted perpendicularly to the z -direction from the collision point at the center of the TPC to the outer wall of the TPC has a length of about 2 m. The distance traversed in the TPC gas is about 1.5 m. The length of the *observable* ionization volume consists of 13 inner segments with $x = 12$ mm and 32 outer segments with $x = 20$ mm for a total length of about $t = 80$ cm [11, Fig. 4]. For present PID purposes the track length is defined as the summed length of the track segments from which the ionization is collected. Depending on magnetic field B , particle momentum p and angle with respect to the z -direction the track length t can be much longer than 80 cm.

Ions and electrons are separated in the gas by an electric field in the z -direction. The ions move slowly, but the electrons are transported to the proportional counters at the pad planes within less than $40 \mu\text{s}$. During the transport of the electrons through the gas (as much as 2 m in STAR TPC) *diffusion* will introduce a displacement from the straight trajectory along the electric field lines. The transit time of the electrons is measured and gives the z coordinate of the initial location of electrons associated with a segment. The ionization J ³⁰ from a track segment is summed over the widths of several pads in each pad row, see Ref. [11, Fig. 4]. In order to determine the *energy deposition* D we must define a volume V in which the energy losses are collected. Such volumes, called cells in Ref. [16], are defined next. The area of the pads in one pad row covered by J from one track and the length corresponding to the spread in arrival times of J at the pads form an “observation volume V ” around the track. The length of V along the track defines the “track segment”.

For the following calculations we consider the volume V surrounding a track segment to be a right cylinder with an axis defined by the particle track, a projected length of the axis in the x - y plane corresponding to the height of the pad rows and in the z -direction corresponding to the spread in arrival time at the pads. For collisions inside of V there are three collision products which can deposit energy outside of V . They are K-shell X-rays, delta-rays with ranges exceeding the size of V and bremsstrahlung.³¹

²⁹Particles with lifetimes of 1 ns or less which are produced in the primary heavy ion collisions will not reach the TPC. Most of the particles observed in the TPC will be “stable” ($e, \mu, \pi, K, p, d, t, \dots$).

³⁰To simplify the understanding of the process the ionization J is discussed rather than the observed quantity Q , the ADC output (Section 1.1).

³¹The production of bremsstrahlung and other effects are discussed in Appendix I.

To consider the escape of X-rays we use the following information. Only K-shell excitations of Ar are important. The mean free path of X-rays with energy just below the K-shell ionization energy $E_1 = 3.203$ keV is approximately 4 cm in Ar at 1 atm [76]. The number of collisions, Eqs. (10)–(12), at $\beta\gamma = 3.6$ for energy losses exceeding 3.2 keV is 0.036/cm ($\lambda = 28$ cm). In 80% of the collisions an Auger electron with energy below 3 keV is produced [77,78], so that the mean free path for X-ray production is 140 cm. For Ne, the value is approximately 800 cm.³²

The effect can be simulated with a Monte Carlo calculation as shown in Fig. 3. As a simplification it is assumed that *all* collisions with $E > 3.2$ keV are K-shell excitations. It is then assumed that 80% will produce an Auger electron (which will deposit its energy locally) and that 20% will produce an X-ray which escapes from the cell V . Two spectra are obtained simultaneously with the Monte Carlo calculation: One with all the energy losses (equivalent to the convolution calculation), $f(\Delta)$, the other for the energy *deposition* for $E < 3.2$ keV, $g(D)$. The percent difference of $g(D)/f(\Delta)$ is given in Fig. 42, together with $f(\Delta)$ and $g(D)$. Thus the X-ray escape usually can be neglected for truncated mean calculations.

The importance of δ ray escape depends on the method of evaluation of their ionization.³³ For the *truncated mean value* along a track, the largest energy loss included in $f(C)$ can be obtained from Fig. 38 where $C_{\max} = 1.6$ keV/cm. If we assume in a primitive first approximation that a *single collision* produced this energy loss in a segment of $x = 2$ cm its magnitude would be $E = 3.2$ keV. The range of an electron with this energy is about 0.2 mm, Appendix E. Therefore, for the evaluation of the truncated mean, a primary ionization cell has a diameter of less than 0.4 mm which is much less than the extent of lateral diffusion. For likelihood evaluations larger cells will occur.³⁴

Another estimate of the magnitude of delta-ray escape can be made from the probability of large energy losses along a track. For a particle with $\beta\gamma = 3.6$ to produce a delta-ray with $E > 10$ keV we get from Eq. (12) or Fig. 10 a mean free path of 80 cm. On the average only one collision per track will occur. The range for 10 keV electrons is 1.4 mm, and in the 0.5 T magnetic field, the initial radius of curvature is $r_c = 0.7$ mm, Eq. (D.1). In effect the cell for *one* segment of the track might then be greater than 2 mm in diameter, all others would be thinner.³⁵ Usually the enlargement of the cell size due to the diffusion of the electrons will exceed the initial cell sizes [80]. It is left to the

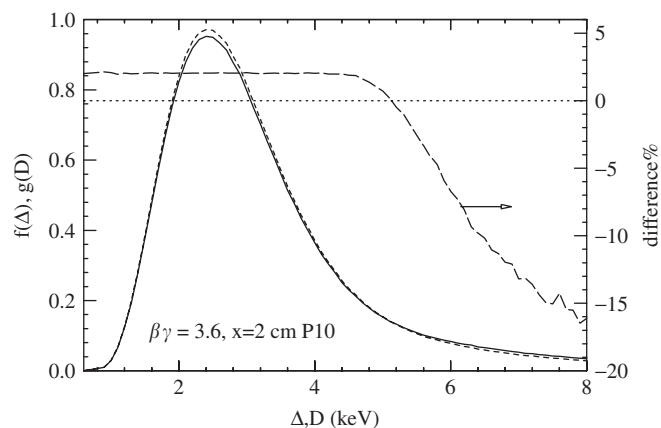


Fig. 42. Calculated example of an energy deposition spectrum taking into account K-shell X-ray escape. The solid line is the energy loss spectrum $f(\Delta)$, the dashed line the energy deposition spectrum $g(D)$. The long-dashed line is the difference between the spectra, in %. For a more realistic approximation the difference might be less than half as much, see text. The calculation was made for 10^7 particles with 0.1 keV ADC bins.

reader to consider this effect on the detection, spatial resolution and PID of the particles and their tracks.

The energy deposition by the fast particles leads to ionization in the detector. The ionization process is complex and only some information about it is given here [16,81]. A collision of a fast particle in a gas will produce an excitation (with a probability of about 20% in P10, see $\Phi(E)$ in Fig. 6) or an ionization giving an electron–ion pair. If the kinetic energy $K = E - E_1$ (where E_1 is the ionization energy of the gas) of the secondary electron (delta-ray) exceeds E_1 , further electron–ion pairs will be produced [16,79,82].³⁶

Thus for gases, the ionization is produced by several processes

- ionization by primary collisions, producing $x \cdot \Sigma_t \cdot (\Phi(E_{\max}) - \Phi(E_1))$ (Eq. (10)) ion pairs in a segment x ,
- secondary ionization by the δ rays with energies exceeding the ionization energy E_1 of the atoms or molecules,
- tertiary ionization by collisions of atoms and molecules in excited states, Penning ionization etc.

Essentially there is no theory³⁷ giving the relation between energy deposition D and ionization J . An example of the Penning effect in P10 is the ionization of a methane molecule (ionization energy $E_1 = 12.6$ eV) by Ar atoms in excited states. In Figs. 6 or 9, 23% of the collisions have energy losses less than the ionization energy of Ar ($E_1(\text{Ar}) = 15.94$ eV), and 14% have losses between $E_1(\text{CH}_4)$ and $E_1(\text{Ar})$. Therefore, for the calculations used

³⁶This happens for only 20–30% of all collisions [16, Figs. 9, 10 or Table 1.4].

³⁷Simulations can be made with Monte Carlo calculations but the necessary cross-sections may be unreliable or unavailable.

³²The variance of the counts in one ADC bin usually exceeds the number of X-ray escapes per bin.

³³Calculations of delta-ray escape have been made but are so far unpublished.

³⁴In an early study of likelihood analysis I found a reduction in overlap if one or two large energy losses were excluded.

³⁵The *restricted energy loss* for $E_r < 10$ keV, Eq. (24), is only 80% of dE/dx given by the Bethe–Bloch theory. On the average the 20% residual energy loss will be produced by one collision with $E > 10$ keV per track.

here, all excitations are included in the calculation of CCS. A more detailed description can be found in Ref. [81].

In order to calculate the number J of ion pairs produced by the energy deposition D the approximation $J = D/W(T)$ is used where $W(T)$ is the average energy needed to produce an electron–ion pair by a particle with kinetic energy T , usually measured experimentally [31]. We assume that $W(T)$ is independent of T and particle type.³⁸ As a guess a variation of $\pm 2\%$ might be used for the dependence on $\beta\gamma$, Figs. 56 and 57. An effect which must be considered is that a discrete number of ion pairs is produced in each segment [73]. Consider the smallest segments in ALICE [24, Fig. 30: energy losses $\Delta < 100$ eV will produce only 0–4 ion pairs. The proportional counter and the ADC will disguise this discreteness and may not register such small values of J .

Similar processes occur in solids: an electron hole pair is created by the primary collision and the secondary electrons and holes can produce further ionizations. Detailed descriptions of the process can be found in Refs. [14,83]. The average energy for the creation of an electron hole pair is also called W here (ε elsewhere). It is about 2% less for alpha particles than for protons with energies of a few MeV. From Table IX in Ref. [18] it appears that this difference might still exist at energies of several hundred MeV. It is unexplained.³⁹

10. Conversion of ionization into pulse-height

The stages from the production of ionization J in a TPC to its conversion into pulse-height Q are described in Section 1.1. More details can be found in Refs. [13,16, 1, Section 28.7]. Information for STAR is given in Refs. [11–13], for ALEPH in Ref. [85], for ALICE in Ref. [24]. Modifications of the ionization cloud⁴⁰ during its transport to the pad plane are caused by the loss of electrons due to attachment to gas contaminants (O_2 , H_2O). This electron loss is corrected in the measurements [12,13,87]. Changes in shape are caused by diffusion during the transport to the pad plane. Diffusion should be taken into account in the calculation of spectra: electrons initially belonging to one segment of the track can drift into a neighboring segment [74,80]. This and related problems have been studied for the STAR TPC but no quantitative data are available [67]. Calculations have been made for the ALICE test TPC [74]. The effects have not been included in the calculations

³⁸Insufficient data are available to calculate the dependence of $W(T)$ on T . Customarily it is neglected. For the ionization by delta-rays of energy E the value W is energy dependent [82], but the spectrum of low energy electrons depends little on $\beta\gamma$, Figs. 8 and 10, and we can expect that the W for the total ionization should depend little on $\beta\gamma$.

³⁹It should be assumed that ionization products from surrounding structures (e.g. SiO_2 surface layers) will diffuse into the measurement volume of the detector [84].

⁴⁰In some papers the ionization cloud is called a “cluster”. In others, a cluster designates the ion pairs produced in a single collision, see Fig. 3, and Section 1.2.4 in Ref. [16].

described here. For Si details of these effects are described in Ref. [14].

A broadening of $G(J)$ is due to the Fano fluctuations and the variance of the gas multiplication factor (“anode gas gain,” [11, Table 3,16, Section 9.7]).⁴¹ For present purposes we assume that these effects result in a Gaussian with a width σ_Q given by Ref. [22]

$$\left(\frac{\sigma_Q}{Q}\right)^2 = \frac{B_n}{J} \quad (39)$$

where J is the number of ion pairs produced by one particle traversing the gas and $0.5 < B_n < 1.0$ a parameter defined in Ref. [22]. This Gaussian is much narrower than $f(\Delta)$, see Fig. D.1. About the conversion to pulse height I shall assume here that there is a simple relation

$$J = r + s \cdot Q \quad (40)$$

where Q is the channel number resulting from the linear conversion of the analog signal of the multi-wire-proportional counter (MWPC) into a digital value in an ADC, and r is a “pedestal”. During STAR-TPC data taking this is frequently checked with “pedestal calibrations”. One aspect of the spacial dependence of the coefficients relating J and Q is determined with the “laser calibration” [86]. At STAR-TPC the problems of stability of electronics, loss of drifting electrons, variable gas pressure, gas contamination etc. are measured periodically. Several aspects are described in Tang’s dissertation [87]. The quality of these corrections can be seen in Fig. D.2.

11. Calibration and diagnostics of detectors

The *energy calibration* of a TPC is the assignment of an *energy deposition value* D to a measured ADC value Q , Sections 1.1, 10. The cleanest way to do this is with monoenergetic radiation from radioactive sources [11,88]. It would be desirable to use several sources with energies up to say 20 keV to check the linearity of the gas amplification, Appendix H. It may be more practical to “self-calibrate” the TPC by using the ionization produced by the particles during the experiments. The calibration can be made by using measurements of ionization spectra for segments or for truncated mean values for tracks and comparing them with calculated spectra (Section 14). From Figs. 13, 18 and 19 it is evident that for *segments* the mean energy loss and its variance are not suitable for this purpose. The only distinct features for a calibration for the segments are Δ_p and w , but the use of the cumulative functions $F(\Delta)$ could also be tried. Practical evaluations are described in Section 14. For tracks the truncated mean values and the variances are acceptable for a first approximation because the straggling functions have only short tails, Fig. 20, but

⁴¹For a scintillation detector a broadening is introduced by the electron multiplication. For a solid state detector the preamplifier will introduce a broadening of $G(J)$ due to electronic noise [14,18].

problems seen in Figs. 58 and 59 must be taken into account.

For Si detectors the calibration based on the W -value for photons [27] resulted in experimental straggling functions for which the *average absolute values* of Δ_p and w for many detectors agreed with calculations based on the B–F theory (Section 2.2) to $\pm 0.2\%$, with uncertainties of $\pm 2\%$ for individual measurements [18], also see Ref. [14].

For Ar, Ne and P10 I do not know of any independent measurements of W for relativistic particles. Also, the difference between the B–F and FVP calculations (Appendix A) for most probable energy losses Δ_p is not known, see Table 1. In addition, the uncertainty of the gas multiplication factor is not well known. A calibration must be based on a combined factor for these parameters. It is important to determine the gas amplification factor as a function of the magnitude of J . *It should not be assumed that the ADC output Q is proportional to the ionization J over a wide range of J* , see Appendix H. I have enough confidence in the theory presented here that I want to suggest that the differences found between measurements and calculations could be used as diagnostic tools to determine problems in our understanding of the processes in the TPC. Some differences will be caused by the effects described in Sections 9 and 10, others seen in Section 14 are unexplained.

12. Compounded spectra in TPC

Tracks in a TPC are made mainly by “stable particles”, i.e. particles with lifetimes exceeding 1 ns, such as electrons, muons, pions, kaons, protons, deuterons and tritons [12, Fig. 3]. Measurements for these tracks (Section 1.1) give the ADC output Q_i per segment x_i of a track of length $t = \sum x_i$ by a particle with momentum p . For each track the descriptor C_j (Section 6.1) is derived. In current literature the data C_j for many tracks are presented in the form of a scatter-plot of “ dE/dx ” versus *transverse momentum* p_T , e.g. [11, Fig. 11, p. 676, 1, Fig. 28.5, p. 262, 69].⁴² The coordinate system of these scatter-plots gives a distorted impression of reality for purposes of PID. Firstly, the descriptor C_j representing the ionization measured along the tracks is a finite quantity,⁴³ not an infinitesimal energy dE and is observed over a finite track length t . The abscissa for the graphs should be the momentum p and not p_T : the transverse momentum p_T of a particle can be produced by particles with momenta as high as $1.6p_T$. This increase in p may change $\langle C \rangle$ considerably (Table 5).

The ordinate for *segments* should be Q/x , but, as was shown in Figs. 14 and 24, Q/x depends on x and graphs of Q/x (or dE/dx) versus p should be made for small ranges of x . Alternatively, two-parameter scaling (Section 8.2)

⁴²The quantity dE/dx given in the usual scatter plots is the quantity C_i defined in Eq. (28).

⁴³It is advisable to calibrate Q with realistic simulations of Δ or C rather than with the “Bethe–Bloch dE/dx ” [67].

could be used. For *tracks* the ordinate should be C , Eq. (28), and an increase in t may increase $\langle C \rangle$ by several %, Figs. 21–23, 26. This can also be seen from a comparison of Figs. 43–45: it appears inadvisable to consider broad bands of momenta or track lengths for PID. For a comparison between experiment and calculation x , t and p should be measured along the actual trajectory of the particles and for the calculations the corrections described in Sections 9 and 10 should be made. For curved tracks the segment lengths will change along the track. No calculations have been made for this effect. For the rest of this Section I describe calculated examples of TPC data and therefore shall use the truncated mean C for tracks as the “observable” quantity. The modifications incurred in the conversion of Δ into Q (energy deposition and other corrections outlined in Sections 9 and 10) are not made in the calculations given here [11–13,67,74].

In order to give the reader an impression of the complexity of PID, Monte Carlo simulations (Section 6.1) to obtain C_j for 10^6 tracks have been made for $pc = 0.6, 0.7, 2$ and 10 GeV for the stable particles (except muons) defined above. From C_j the straggling functions $f(C; t, pc, M)$ are accumulated: Figs. 43–47. Monte Carlo fluctuations are seen in the tails. For $pc = 0.6$ and 0.7 GeV a pion spectrum for 10^6 particles is shown, and two kaon and electron spectra are shown for 50,000 and 5000 particles each. Spectra for $pc = 2$ GeV are shown in Fig. 46 and for $pc = 10$ GeV in Fig. 47. Here, arbitrary fractions of particles are given in order to show clearly the location of the spectra. Readers are invited to contemplate these figures to consider their own approach

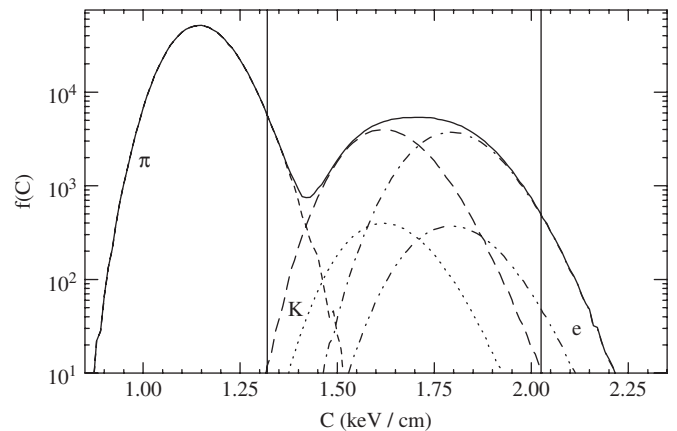


Fig. 43. Monte Carlo calculation of straggling functions $f(C; p, t, M)$ for $pc = 0.6$ GeV particles along tracks of length $t = 78.4$ cm (12 inner segments with $x = 12$ mm, 32 outer segments with $x = 20$ mm of the STAR TPC). The truncation factor is 0.6, so that 26 segments are used to calculate the truncated mean energy losses C . The solid line shows the combined spectrum for 10^6 pions and 50,000 kaons and electrons. The separate functions are shown for 10^6 pions (short dashes, $\beta\gamma = 4.3$), 50,000 kaons (dashed line, $\beta\gamma = 1.215$), 5000 kaons (dotted line) and the same number of electrons (dash-double-dotted lines, $\beta\gamma = 1174$). The binning in constructing the spectra is done with bins of $1 \text{ daeV} = 10 \text{ eV}$. Protons and heavier particles have $C > 2.3 \text{ keV/cm}$. The vertical lines at 1.32 and 2.03 keV/cm are used for PID described in Section 13.5. For kaons, $\sigma \sim 0.115 \text{ keV}$.

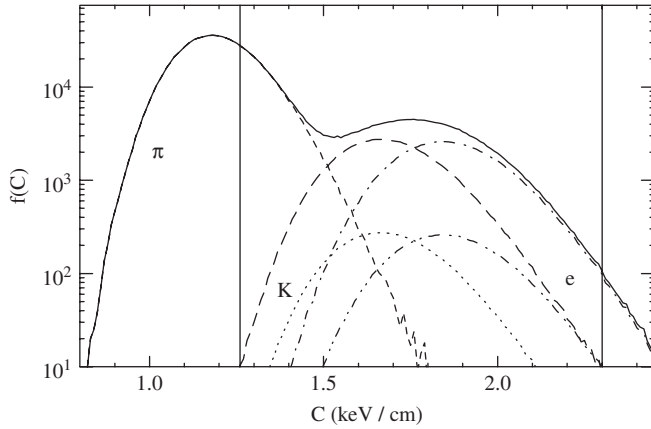


Fig. 44. Same as Fig. 43 but for $t = 40$ cm. The overlaps are increased. For kaons, $\sigma \sim 0.15$ keV.

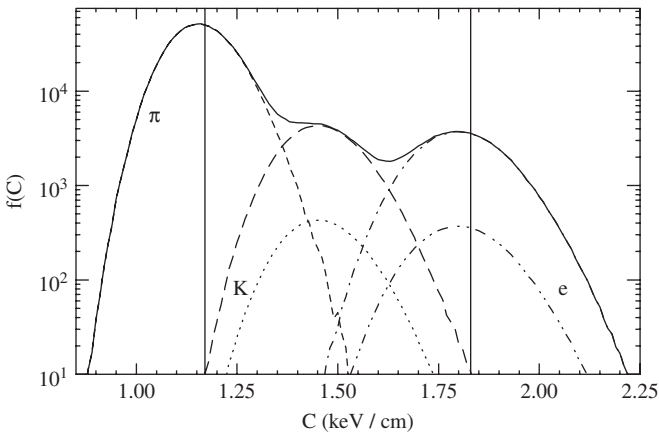


Fig. 45. Same as Fig. 43 but for $pc = 0.7$ GeV. The proton spectrum begins at $C = 2.3$ keV/cm. Compared to Fig. 43, the locations of pion- and e-spectra are unchanged, the kaon spectrum is moved to smaller C , the K - π overlap is larger and the K - e overlap is smaller.

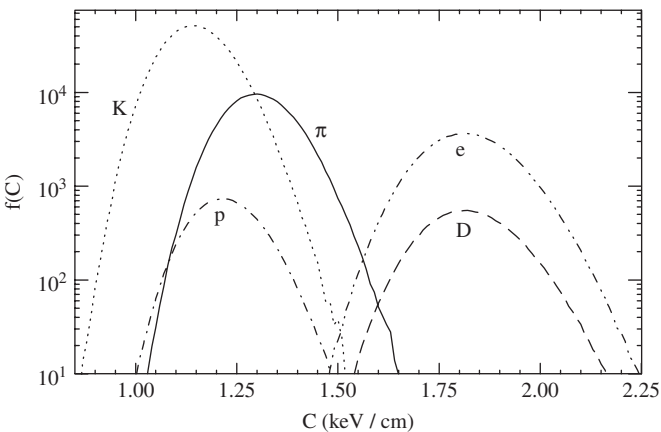


Fig. 46. Equivalent to Fig. 43 but for $pc = 2$ GeV. The spectra for protons p and deuterons D are also shown. In order to show the position and overlap of the functions, arbitrary numbers of particles are used.

to PID. In particular I suggest that the overlap (Section 13.2) will give a clearer indication of particle separation than the use of standard deviations, Eqs. (33) and (41) and Table 5.

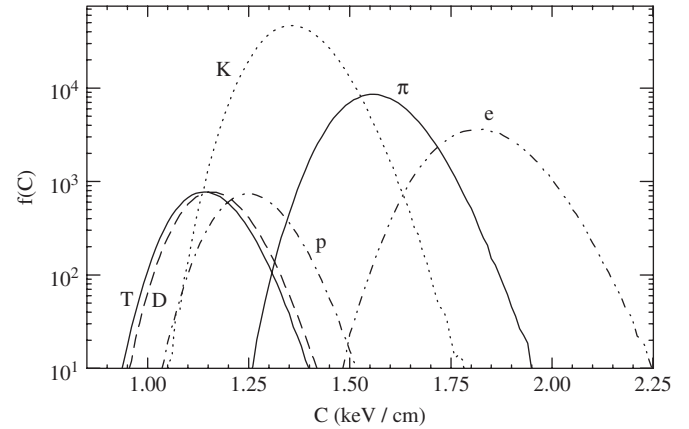


Fig. 47. Same as Fig. 46, but for $pc = 10$ GeV. The spectrum for tritons T is also included. In order to show the overlap of the functions, arbitrary, different scales for the ordinate have been used. PID appears only possible with further information, e.g. TOF, except possibly for identifying π and e with PID according to Section 13.4.

13. Particle identification PID with TPC measurements

13.1. Principles

PID means a determination of the number of particles of each mass from experimental spectra of the type shown in Figs. 43–47. PID is based on the fact that the momentum of a particle of mass M is given by $pc = Mc^2\beta\gamma$, while ionization depends on $\beta\gamma$ only. Momentum and ionization of particles along their tracks are measured to determine their mass M .

I am describing approaches to PID which are based on the concept that the ADC output Q is calibrated with calculated values such as Δ_p for segments or $\langle C \rangle$ for tracks. I expect that calculated spectra Figs. 43–45 will closely resemble measured spectra. This should be confirmed, see Section 14.

The effect of the corrections described in Sections 9–11 on the Δ_p and w for segments and $\langle C \rangle$ and σ for tracks are not included here. In a first approximation these corrections are symmetric in shape, and we can anticipate that they will cause only small shifts in converting Δ_p into Q_p and $\langle C \rangle$ into the corresponding ADC output Q_t . An increase of a few percent might occur for w of segments and for σ for tracks, [74], Appendix H.

13.2. Resolution, separation power and overlap

For tracks, the truncated mean value $\langle C \rangle$ and its variance σ , Eqs. (32) and (33) are used for PID in recent papers. As a measure related to PID, the concepts “resolution” and “separation power” have been defined. A description based on experimental data has been given by Tang [87]. Resolution is defined as the ratio

$$r_s = \frac{\sigma}{\langle C \rangle}. \quad (41)$$

Some values are shown in Figs. 21–23 and can be calculated from the data in Section 6.2 and in Table 5. A resolution function is also given in Fig. 49.

The separation power D for particles A and B with momentum p is defined by [10,64,87]

$$D = \frac{\langle C \rangle_A - \langle C \rangle_B}{\sigma_{A,B}} \quad (42)$$

In practice σ_A and σ_B so far have been assumed to be the same [87] or σ_B is used [64]. This is a coarse approximation. For a track with $t = 62$ cm, in Table 5, for $pc = 600$ MeV pions and kaons we have $\langle C \rangle_\pi = 1.161$ keV/cm, $\langle C \rangle_K = 1.639$ keV/cm, $\sigma_\pi = 0.0885$ keV/cm and $\sigma_K = 0.115$ keV/cm which differ by 30%. D can be calculated with the data in Table 5.

I believe that the “overlap” of straggling functions gives a more informative description about PID than the separation power of Eq. (42). The overlap is defined by the area which is joint to two adjoining straggling functions, e.g. the roughly triangular area between $C = 1.32$ and $C = 1.53$ and the π and K dashed curves in Fig. 43. (It would also include some electrons if their number were more than 5000.) Clearly the overlap depends on the relative number of particles.

The overlap cannot be derived directly from the experimental function, but it can be obtained from compounded spectra calculated with the numbers of particles derived with the methods described in Sections 13.3 and 13.4. Details and examples are given in Refs. [89,90]. A value of the number of particles in the overlap region can be obtained from Fig. 48 which shows the cumulative functions $F(C)$ for K and $1 - F(C)$ for π , Eq. (26). The number of particles for which no mass assignment can be made is given by the crossover points A or B . A program calculating these functions is available [26]. Overlaps are shown in Fig. 49. They have been calculated for tracks with 12 inner segments and with the number of outer segments given in the abscissa. The resolution r_s calculated with Eq. (41) is shown by the solid line. Examples of PID given below are based on the use of truncated mean values C for tracks. For calculations with the likelihood method, similar results will be obtained with smaller overlaps.⁴⁴ If there is an overlap of the functions $f(C; p, t, M)$, such as the pion, kaon and electron functions in Fig. 43, the cumulative functions $F(C; p, t)$ may be more suitable for PID. Such functions are given in Figs. 50–53. Cumulative figures corresponding to Figs. 46 and 47 might be useful for π -e assignments.

⁴⁴For experimental data, because of the problems outlined in Sections 6.2, 9–10 and Appendix D it is yet to be studied whether the overlaps will be smaller. I have made calculations with the likelihood method but do not have enough detail to give them here.

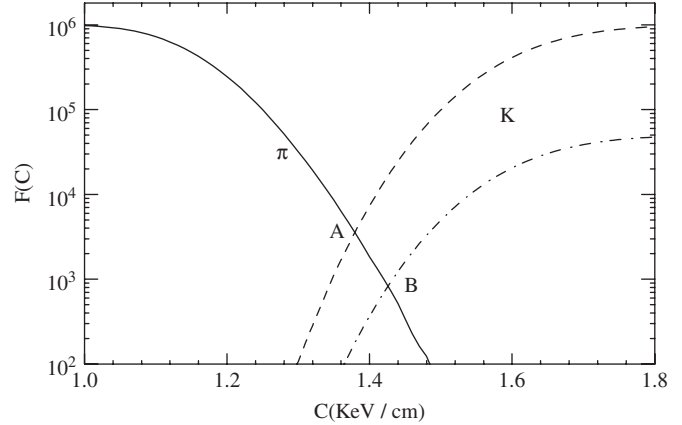


Fig. 48. Overlap for $t = 78.4$ cm of $pc = 0.6$ GeV π and K . The solid line is the cumulative function $1 - F(C)$ for 10^6 pions, the dashed line is $F(C)$ for 10^6 kaons. The overlap is given by $A = 3500$ particles. The dashed-dotted line is for 5% kaons, with an overlap $B = 800$ particles.

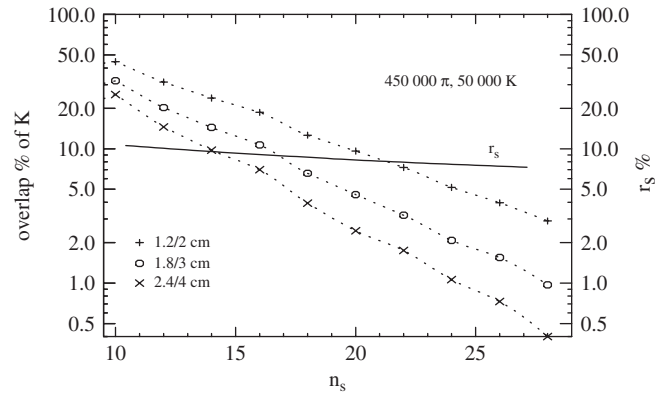


Fig. 49. Overlap of $pc = 0.6$ GeV π and K as a function of track length. The tracks consist of 12 inner segments (of lengths 1.2 or 1.8 or 2.4 cm) and n_s outer segments (of 2 or 3 or 4 cm). The solid line is the resolution r_s of Eq. (41) for a 1.2/2 cm track. The truncation is set to $f_r = 0.6$.

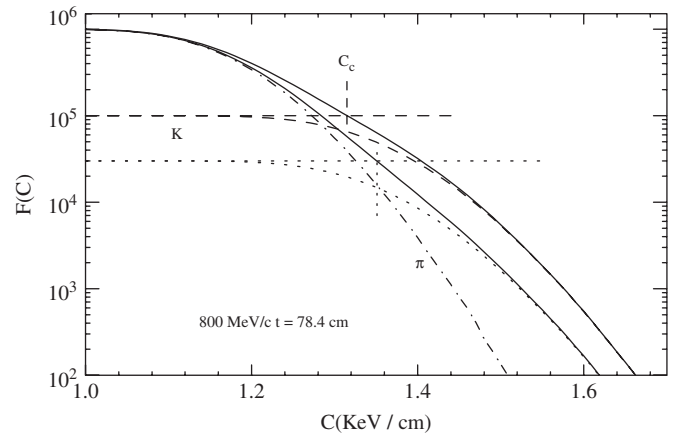


Fig. 50. Cumulative spectra $F(C; p, t, f_r)$ of spectra for $pc = 800$ MeV for pions (dashed-dotted line) and two fractions of kaons: $f_k = 3\%$, dotted line, $f_k = 10\%$, dashed line. The cross-over points of the kaon lines with the pion line shifts to the left. The cross-over points $C_c(f_r)$ of the horizontal lines from the left with the sum-p.d.f.s gives the number of kaons. This information is used in Section 13.4 for PID. The solid lines are the sum spectra for pions and kaons.

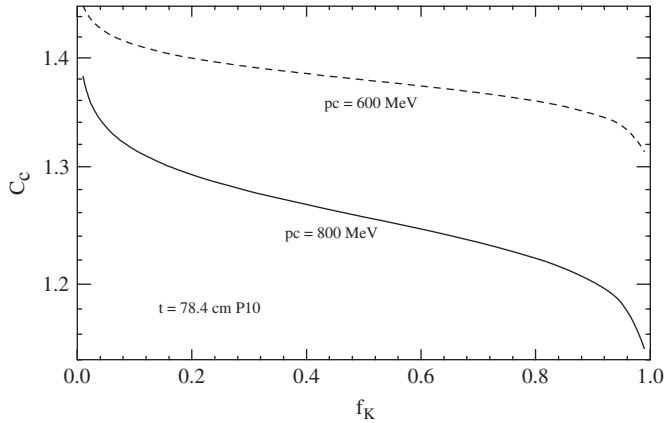


Fig. 51. The cross-over points C_c as a function of the fraction f_k of kaons in pion–kaon cumulative spectra $F(C; p, t, f_i)$ for $pc = 600$ MeV and $pc = 800$ MeV. For the calculations of C_c the sum of the particles must be constant.

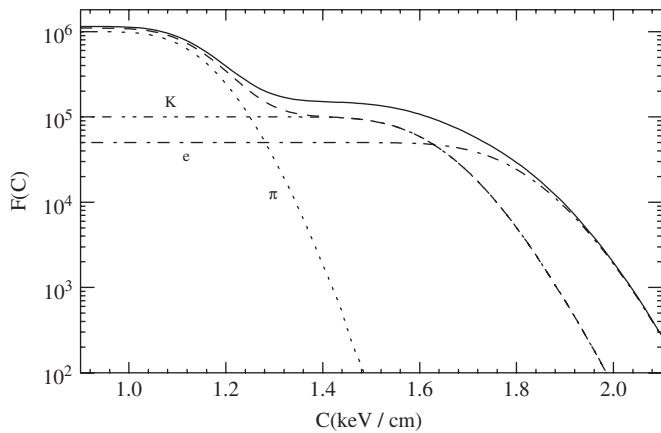


Fig. 52. Cumulative spectra $F(C_i)$ of p.d.f. for $pc = 600$ MeV, $t = 78.4$ cm of Fig. 43. There are 10^6 pions, 10^5 kaons and 50,000 electrons. The solid line is the sum of all of the C and is equivalent to an experimental observation. The dashed line is the sum for pions + kaons only. An evaluation of the functions is given in Section 13.4.

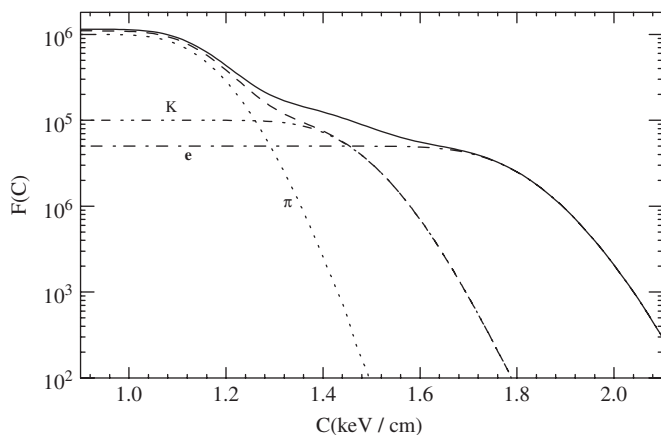


Fig. 53. Same as Fig. 52 for $pc = 700$ MeV. For pions and electrons the straggling functions are practically unchanged, but the kaon function shifts position. This is expected from Table 5.

13.3. Particle identification

In many publications experimental compounded spectra, Figs. 43–47, have been fitted with multi-Gaussian fit functions [87].⁴⁵ It is not clear how many fitting parameters are used for this procedure. I am suggesting that such fits with calculated functions given here (and tabulated in Ref. [26]) would reduce the need for fitting parameters: Since momentum p is known, the values of $\beta\gamma$ for all candidate particles can be determined and the corresponding values of $\langle C \rangle$ can be found in Table 5. Calculated functions $f(C)$ for each particle can be obtained readily by scaling the reference function of Figs. 37–39. The scaling parameters a and b are selected from Table 5, and the straggling function for each particle is scaled from the reference function. Figs. 22 and 23 may be used to fine tune $\langle C \rangle$ for track length, and an uncertainty can be assigned from Fig. 21. No fitting parameters should be needed for $\langle C \rangle$. The primary value of σ is also selected from Table 5 and adjusted for track length with the data in Figs. 21–23. Because of the effects described in Section 10 and Appendix D these values might need a best fit search over a range between σ and 1.1σ . The final search for fit parameters is made for the number of particles of each type. A preliminary estimate of these numbers could be obtained by fitting spectra to the left and right of the vertical lines in Figs. 43–45 or 50–53.

Problems with the scaling method will be encountered in the tails for the situation shown in Fig. 38, or for very short tracks, Fig. 41. To obtain the overlap numbers cumulative functions can be constructed according to Fig. 48 by using scaling of Fig. 38.

13.4. PID with cumulative straggling functions

PID can be made with the cumulative spectra shown in Figs. 50–53. For spectra where some parts of $F(C)$ are approximately constant, particle numbers can be read directly: in Fig. 52, for $C \sim 1.5$ keV/cm, the number of kaons plus electrons (full line) is about 15% of the total number of particles. For more reliable determinations, a calculation based on the use of the crossover points C_c shown in Fig. 50 can be made. The calculation is easy to understand for two particles. The values C_c must be calculated as a function of the fraction f_k of kaons. Two examples are shown in Fig. 50. C_c is the abscissa of the intersection of the horizontal line giving the fraction f_k of kaons (dotted and dashed lines) with the sum-spectra, solid lines. Examples of $C_c(f_k)$ for various fractions f_k of kaons are given in Fig. 51 for $pc = 600$ and 800 MeV.

The fraction of kaons is found in successive approximations. Select a plausible value C_1 (this will be easier if a calculated function $F(C; \pi)$ is superposed on the measured straggling functions), and find from the solid line (representing now the experimental straggling function) in the figure the experimental value $f_k = F(C_1)/F(C_a)$ where

⁴⁵This is the case for most STAR and NA49 publications.

C_a is the value below which $F(C < C_a)$ is constant. Next read the value $C_2 = C_c(f_k)$ from Fig. 51 and find $f_k = F(C_2)/F(C_a)$. Iterate until f_k is constant.

Evidently the procedure will be more complex for more than two particles. I have successfully calculated this for 700 MeV/c pions, kaons and electrons, Fig. 52 and 53. There are two cross-over points, which are a function of the two fractions f_k and f_e , and tables must be calculated for $C_c(f_k, f_e)$ and $C_e(f_k, f_e)$. This may not work if the number of kaons is less than the number of electrons.

Once the fractions of particles have been found, graphs of the type of Fig. 52, 53 for all particles can be drawn and the “purity” [87] can be read from the graph. The use of scaled straggling functions for this purpose will be somewhat more reliable than “multi-Gaussian fitting” described in [87], see the Gaussian fit in Fig. 20.

13.5. Exclusive assignment of particle masses

If the fractions of particles in an experiment have been determined, Fig. 43 can be calculated, and particle types can be assigned to given tracks according to their value of C_j . Take the solid line, i.e. the sum-p.d.f. of Fig. 43 (10^6 pions and 50,000 kaons and electrons each). For $C_j < 1.32$ keV/cm, all particles will be pions, for $C_j > 2.02$ keV/cm, all particles will be electrons, and for $1.32 < C_j < 2.02$ keV/cm we cannot uniquely assign a mass to the track, but we can read the numbers of each particle from Fig. 52, see purity [87]. Alternatively the procedure in Fig. 48 could be used.

14. Comparison of experiments and theory

In order to assess the performance of a detector, to calibrate it (Section 11), and to check our understanding of the theory, we compare experimental measurements with calculations. For the ALICE test TPC a detailed study has been made by Christiansen [74]. For the STAR TPC I have made some comparisons which I describe next. In the initial calibrations of the STAR TPC in the year 2000 the complexity of the problems described e.g. in Figs. 14, 17, 19, 21, 24, 29 was not fully appreciated, and the calibration was based on the use of the “Bethe–Bloch dE/dx ” [67]. I present in this section experimental data which I compare with calculations. The comparisons should be considered as tentative results which show reasonable agreement between experiment and calculation but should also be considered as a guide to more detailed and accurate studies especially to assess the effects described in Section 10 [74].

A set of ionization measurements for segments made with STAR in Running Period 1 (2001) was provided by Yuri Fisyak [67], as was another set for both segments and tracks made in Running Period 4 (2003). From these data experimental straggling functions $h(Q_x; x, p)$ for segments over bands of momenta $p \pm 6\%$ and segment lengths $x \pm 3\%$ were extracted. The functions for tracks were $h(C_x; t, p)$ where the track lengths were $70 < t(\text{cm}) < 76$ and the width

of the momentum band was 50 MeV/c. $C_x(t)$ is the measured truncated mean value of the ADC output for a track of length t . These functions correspond to thin vertical slices of a scatter plot similar to Fig. 11, p. 676 in Ref. [11]. Energy loss straggling functions for segments, $f(\Delta; x, p)$, and for tracks, $f(C; t, p)$, were calculated for pions with the central values of the experimental band of p and segment-lengths x or track lengths t . The experimental values of Q and C_x were given in keV/cm, based on a calibration with the Bethe–Bloch values, so they differ from the theoretical Δ_p and C by a factor which corresponds to the difference between $\langle \Delta \rangle$ and Δ_p shown in Figs. 13 and 14 or Δ_p/x and M_0 in Table 2. Since in the experimental spectra shown here the majority of particles was pions, I compare them with calculations for pions only. Other particles usually will fall in the tails of the spectra.

For segments it is evident from Figs. 18 and 19 that the use of mean values for the segment spectra can lead to inconsistent results, depending on the length of the spectra and the contribution from various particles.⁴⁶ For tracks, spectra of truncated mean values and RMS widths will cause fewer problems, see Fig. 20. For the first set of comparisons for segments [92] an individual straggling function was calculated for each experimentally measured function. The functions were compared graphically, Figs. 54 and 55.

For later comparisons the similarity in shape of the spectra seen in Figs. 32 and 37–39 was used: for comparisons for all $\beta\gamma$ and a given x or t a single calculated spectrum for $\beta\gamma = 3.8$ was scaled with the search parameters a, b and the peak value of $h(Q; x, p)$ or of $h(C; t, p)$, Appendix D. A three parameter least squares fit to experimental data was made with this spectrum. From the differences between experimental and calculated straggling functions seen in Sections 14.1 and 14.2 and Fig. F.1 in Appendix D it appears inadvisable to make the fit calculation for the *full* measured functions with calculated functions including pions only. Therefore, the comparisons were made for the central part of the measured $h(Q_x; x, p)$ or $h(C_x; t, p)$. A compounded function calculated for two or more particles would require too many parameters to give a reliable test of the theory. Comparisons were made without the corrections described in Sections 9 and 10. These corrections cause small changes in Δ_p and $\langle C \rangle$. Possibly they could explain some of the differences seen in Figs. 54–60.

14.1. Comparisons for segments

A first comparison for data from the STAR 2000 run was given in Ref. [92]. The experimental data were available through the ROOT program. A fit with the parametrized “Landau function” provided in ROOT did

⁴⁶This was confirmed in preliminary evaluations of experimental data with ROOT [91].

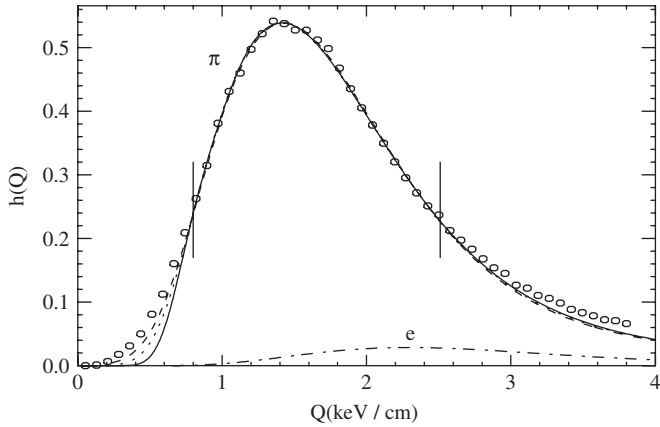


Fig. 54. An experimental straggling function for $x = 1.284$ cm in P10 and $pc = 417$ MeV is shown by the circles. The calculated functions are described in the text and are shown by the solid and broken lines. The vertical lines at $Q = 0.8$ and 2.5 keV/cm define the range of measured values of Q used for the fit calculations. An electron spectrum for $pc = 417$ MeV is given by the dashed-dotted line.

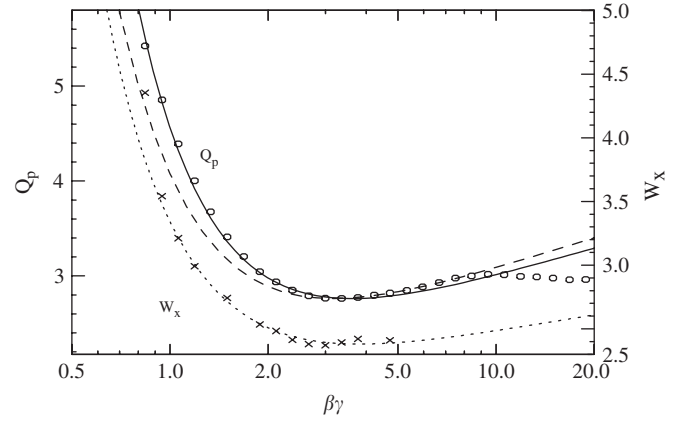


Fig. 56. The dependence of measured values of Q_p on $\beta\gamma$ is shown by the circles for $x = 2.12$ cm. For comparison, the calculated Bichsel function $f(\Delta; x, \beta\gamma)$, Section 7.2 is shown by the solid line. It is scaled to match experiments at the minimum ionization. The dashed line is the “Bethe–Bloch dE/dx ” scaled to have the same minimum as the experimental function. The FWHM w_x is given by crosses, scale at right. The calculated function is given by the dotted line. The deviation for $\beta\gamma = 0.8$ is unexplained.

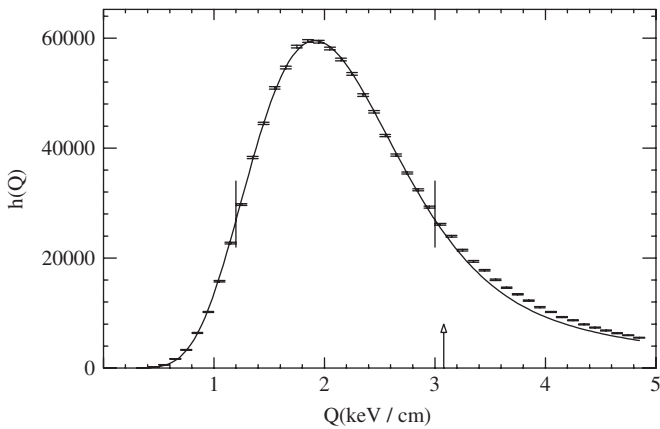


Fig. 55. An experimental straggling function for $x = 2.12$ cm in P10 and $pc = 525$ MeV is shown by the symbols with error bars. The function calculated for pions and fitted to $1.2 < Q < 3$ is shown by the solid line. The arrow at $Q = 3.08$ keV/cm indicates the location of Q_p for kaons and electrons, see Table 2. The deviations for $Q > 3$ keV/cm are unexplained. Scale for Q based on “ dE/dx calibration” [67].

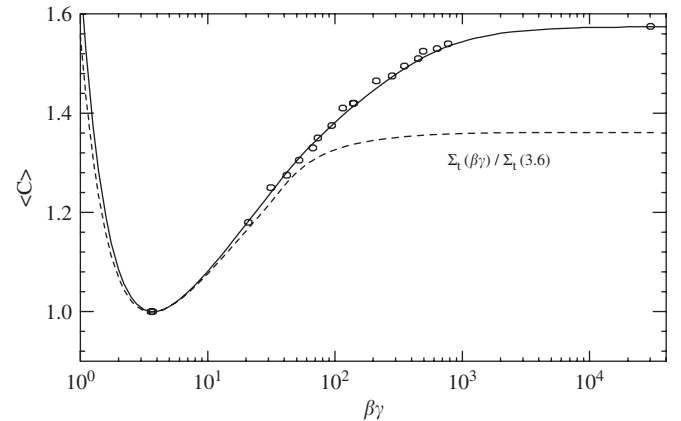


Fig. 57. Experimental data from Lehraus: circles. The solid line gives the FVP calculations of $\langle C \rangle(\beta\gamma)$ for tracks in P10 and is equivalent to the functions given in Fig. 26. Only one free parameter is needed, the normalization to 1.0 at minimum ionization. Compare to Fig. 10 in Ref. [10] and Fig. 2 in Ref. [64]. A dependence of $W(T)$ on $\beta\gamma$ cannot be excluded. The total collision cross-section $\Sigma_i(\beta\gamma)$ is also shown, it is the quantity needed for MC calculations, Section 4.4, also see Fig. 25. The difference is important for the method described in Appendix J.

not result in good agreement with experimental data as can be expected from Fig. D.3. Similarly, fits over the whole spectrum did not agree well with calculated spectra. Therefore the approach described above was used.⁴⁷ An example for $x = 1.284 \pm 0.04$ cm, $pc = 417 \pm 25$ MeV is given in Fig. 54. The measured function $h(Q_x; x, pc)$ is shown by the circles. The solid line represents a calculated straggling function $f(\Delta; x, pc)$ for pions in P10 gas. For the dotted line the calculation includes the fluctuations given

by Eq. (39) with a magnitude suggested in Ref. [22], for the dashed line this magnitude is 2.5 times as large. The other effects described in Section 10 may also contribute to the differences. They should be explored further. The dashed-dotted line is a calculated spectrum for electrons with 5% of the number of pions. The difference between experiment and calculation for $\Delta > 2.8$ keV appears to be at least in part due to electrons. As evident from the figure the difference for $\Delta < 0.8$ keV could be due in part to the

⁴⁷In my STAR Notes [92], until now, the quantity Q has been called J/x and the mean truncated value for one track was called $\langle J/x \rangle$. It is now called C .

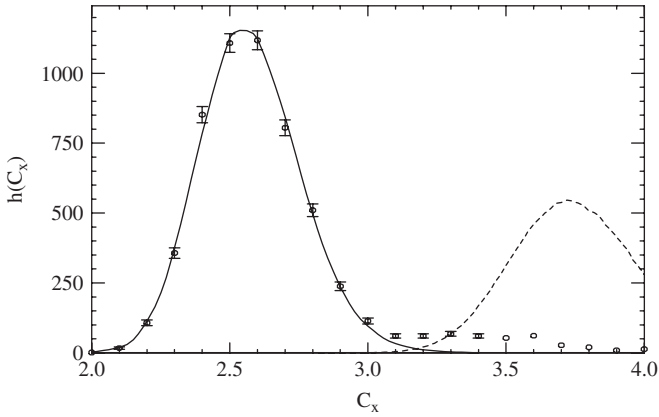


Fig. 58. Experimental spectrum $h(C_x)$ (symbols) for particles with track lengths $70 < t < 76$ cm in P10, with momenta $300 < pc < 350$ MeV. The simulation is made with spectra for $t = 73.2$ cm and $pc = 325$ MeV in P10 for pions, solid line and electrons, dashed line. The experimental data for $C_x > 3$ do not conform to the electron spectrum.

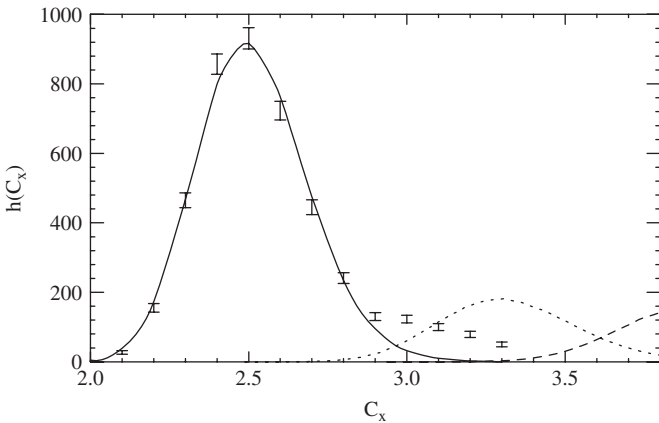


Fig. 59. Similar to Fig. 58, but for $600 < pc < 700$ MeV. The calculated pion spectrum is given by the solid line, a kaon spectrum with 20% intensity is shown by the dotted line, an electron spectrum with 20% intensity by the dashed line. The experimental data for $C_x > 2.9$ do not conform to the kaon spectrum.

Fano- and gas-multiplication fluctuations and in part to other effects described in Section 10.⁴⁸

A comparison for $x = 2.12$ cm and $pc = 525 \pm 6\%$ MeV is given in Fig. 55. There is no deviation for small values of Q . Comparisons were made for $x = 2.12 \pm 0.06$ cm and for many particle speeds. Results are shown in Fig. 56. The experimental most probable values $Q_p(\beta\gamma)$ and FWHM $w(\beta\gamma)$ obtained for these data are compared to values described in Section 7.2. They are normalized to calculated values at $\beta\gamma = 3.7$. The RMS deviation between experiment and calculation is $\pm 1\%$ for $1.2 < \beta\gamma < 9.5$ and $\pm 1.6\%$ for w . No explanation has been found so far for the deviations for

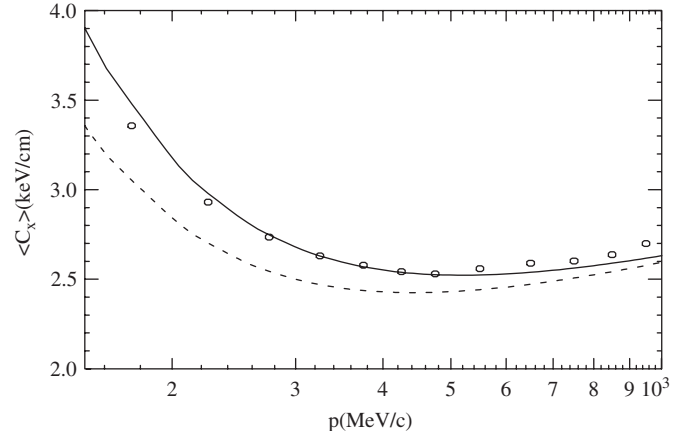


Fig. 60. Measured values (circles) of $\langle C_x \rangle$ ($f_r = 0.7$) for tracks with length $70 < t < 76$ cm as a function of particle momentum p for pions. The solid line gives calculated averages (C) of truncated mean values of energy loss C matched to experiment at minimum ionization, the dashed line is BB stopping power dE/dx . The differences for $p < 200$ MeV/c may be due to the increase in segment lengths due to curvature in magnetic field. The average deviation between $\langle C_x \rangle$ and the calculation is $(1 \pm 1.5)\%$. A dependence of $W(T)$ on $\beta\gamma$ cannot be excluded.

$\beta\gamma > 9.5$. For $x = 3$ cm segments, the RMS deviation between experimental and theoretical values for $1.2 < \beta\gamma < 9.5$ is only $\pm 0.5\%$, for $x = 4$ cm segments, for $4.2 < \beta\gamma < 9.5$ this deviation is $\pm 0.6\%$. We conclude that the calculated functions $\Delta_p(x; \beta\gamma)$ agree with measurements to 1% or better for $2 \leq x(\text{cm}) \leq 4$ and for $1.2 < \beta\gamma < 9.5$, while the Bethe–Bloch dE/dx function, normalized at $\beta\gamma = 3.7$ is about 10% lower at $\beta\gamma = 1$.

14.2. Comparisons for tracks

The geometry of older TPCs, consisting of fairly homogeneous segment lengths, permits an easy comparison with theory. This results in the good agreement of the data given by Lehraus et al. [93] with the present FVP calculations, shown in Fig. 57. No free parameters are used in these calculations except that the ionization at minimum is set equal to 1.0. The average deviation between experiment and calculation is $(-0.3 \pm 0.5)\%$, similar to what was found for Si [18]. The systematic deviation of 3% between B–F and FVP appearing in Table 1 does not appear because of the normalization at minimum ionization. The function $\Sigma_t(\beta\gamma)$ needed for the calculation of $f(\Delta)$ is also given.

The cylindrical geometry of the STAR TPC makes the analysis of experimental data for tracks more complex because track lengths depend on the angle of the track relative to the centerline. This is evident from the slanted track in Fig. 26. Comparisons for tracks of length $t = 73.2$ cm are made for $pc = 325$ MeV in Fig. 58 and for $pc = 650$ MeV in Fig. 59. In Fig. 58 the data for $C > 3$ keV do not agree with the spectrum for electrons and thus cannot be assigned a definite mass. For kaons the most probable value for $\langle D/x \rangle$ is about 7 keV, and no energy deposition

⁴⁸Inner pads are 3×12 mm. In general more than one pad will collect the ionization (Section 9). If the ionization on a marginal pad is below the threshold for the ADC, the total signal Q will be too small. It might be interesting to simulate this effect.

by kaons would appear on the graph. A similar situation occurs for Fig. 59. Experimental values for $C > 2.9$ keV could be kaons, but we would expect them to peak at 3.3 keV. A more detailed study is needed to explore these discrepancies. In Fig. 60 the experimental average values $\langle C \rangle$ are shown as a function of pion momentum p . The corrections described in Section 10 are not included in the calculations.

15. Conclusions and recommendations

The complexity of the energy loss spectra for single collisions is shown in Figs. 5, 6, and J.2. The consequences of these complexities persist for practically all the functions derived here and can be seen in Figs. 14, 15, 30, 41, C.2, and D.3. It is therefore not advisable to simplify the spectra as shown e.g. in Fig. J.2.

For straggling functions for thin absorbers, Eq. (20), it is instructive to consider the Poisson distribution and the convoluted CCS separately, Figs. 2 and G.1, also Ref. [5].

Because of the complexity of the evolution of straggling spectra $f(\Delta; x, \beta\gamma)$, with increasing x (Figs. G.1 and G.2) there are no simple analytic functions to represent them. Even for the representative parameters Δ_p , w and $\langle C \rangle$ the functional dependence on $\beta\gamma$ is complicated, Fig. 15, 21–28. The shape of straggling functions for segments is determined in part by the Poisson distribution, Eq. (18). Since this function depends greatly on Σ_t , while the B–F stopping power is given by M_1 , we must expect the dependence of Δ_p on $\beta\gamma$ that is seen in Figs. 15, 24, 25 and J.1. It will be useful to remember these properties if calculations are made with GEANT [63]. For segments, over limited ranges of x and $\beta\gamma$, two-parameter scaling can be used to relate, within limits, the functions, Figs. 31–35.

For tracks the straggling spectra $f(C; t, \beta\gamma)$ for the truncated mean C show smaller variations, Figs. 21–23, 26 and two-parameter scaling can be used over larger ranges of t and $\beta\gamma$, Figs. 36–39, but see Figs. 40 and 41. Even for long tracks a Gaussian is not a good approximation for the straggling function, as shown in Fig. 20.

It appears advisable to calibrate the energy deposition in detectors with the quantities calculated here, i.e. Δ_p , w or $\langle C \rangle$ and σ . Correction factors such as diffusion overlap for segments, variations of multiplication factors of proportional counters etc. can then be determined from the experimental data.

In the comparison of experiments and calculations the multiplication factor (or anode gas gain) of the proportional counters is an unknown parameter, with an unknown variance. The other effects described in Section 10 are expected to influence the peak values Δ_p or $\langle C \rangle$ little, but may change w by 10% or more. The variances of these effects are unknown. The effects can be determined with measurements of the type shown in Section 14 and in Appendix H.

I suggest that the calculations presented, after corrections for the effects described in Section 10, agree with

measurements to about 1%. Thus the results of the theory described here should be taken seriously. If differences between measurements and calculations appear, explanations should be found.

The difference between the B–F and the FVP theories for $Z < 20$ are small enough that it probably is not worthwhile to implement B–F for the present applications. This might be different for Kr.

It is therefore recommended that further measurements of ionization in TPCs be compared and calibrated with data calculated with FVP. Depending on the application, tabulated straggling functions such as those shown in Figs. 32–35 and 37–39 can be used [26]. Two-parameter scaling reduces the need for such tables. For the dependence on particle speed, functions such as those shown in Figs. 24–26 should be used rather than the “Bethe–Bloch dE/dx ” $M_1(\beta\gamma)$ and “restricted energy loss functions” (Eq. (24)). In particular it must be noted that the function $\Sigma_t(\beta\gamma)$ should be used for calculations of $f(\Delta)$, Appendix J.

The calculations can serve as a diagnostic tool to assess and improve the performance of the TPC. Consider e.g. that no explanation for the part of the spectra for $Q > 2.9$ keV in Figs. 58 and 59 have been found so far.

For PID, the concept of *overlap* will produce more descriptive information than the concepts “resolution” and “separation power”. It is conjectured that only the tails of experimental straggling functions are distorted by the process of collection of the ionization clouds in the TPC, Sections 9 and 10. This may make the use of the maximum likelihood determination of track parameters unreliable. I have not yet applied the PID procedures suggested in Section 13 to any TPC. I hope that they will be useful in practice. The use of broad momentum bands implied e.g. in considering simultaneously all tracks with a given transverse momentum p_T may increase the overlaps (or decrease the resolution). It is advisable to use two-parameter scaling for *each* track.

The use of scaling, shown in Figs. 32–39 and Table 5, will simplify the computing effort. It will be necessary to explore the dependence of the overlap or resolution on track length and the number of track segments. Most of the energy loss calculations have an uncertainty of less than 1%. The uncertainties of the conversions made in the various stages going from Δ to Q are not well established.

Programs and tables used for the production of the contents of this paper are available from the author, and in Ref. [26].

For thin segments, e.g. 7.5 mm Ne, Fig. 30, it must be kept in mind that the smallest energy depositions will produce only a few ion pairs.

Acknowledgements

Many colleagues have discussed the problems presented here with me. I am grateful to J. Berkowitz, J. Samson, W. Scholte and C. Brion for giving me tables of the optical absorption coefficients and advice. M. Inokuti has helped

me with many aspects of understanding collision cross-sections. Y. Fisyak and J. Porter have guided me to a better understanding of the operation and data analysis of the TPC. D. Groom, H. Matis and E. Nappi have helped with many suggestions. P. Christiansen has contributed much to my understanding of the ALICE TPC.

Appendix A. Comparison of B–F and FVP theories

Only for Si there are enough data about the generalized oscillator strengths needed in B–F theory. Straggling functions for Si were calculated with BF and FVP CCS described in Sections 2.2 and 2.3 with the convolution method (Section 4.3). An example of such calculations is given in Fig. A.1. The difference in Δ_p is -4% , in w it is 1.2% . The difference in Σ_t is 6% , in M_1 (“ dE/dx ”) only 0.5% , see Table 1.

I anticipate that similar differences will occur for calculations with both methods for Ne and Ar, but they might be bigger for Kr and Xe. For a detector filled with Ne, Ar or P10 gas the current understanding of gas multiplication is probably not accurate enough to discern differences similar to those seen in Fig. A.1, also see Appendix J.

Appendix B. Comparisons of straggling functions for Ar and P10

Until April 2003 all my calculations were made for Ar. Since then they have been made for P10. Comparisons of functions for segments $x = 1.2\text{ cm}$ for the two gases are given in Table B.1. A constant factor relating the functions will be irrelevant because it will disappear in the calibration of the TPC in terms of absolute energy losses or depositions, but the dependence on $\beta\gamma$ will remain. Variations in the factors r exceed the 1% level desired for this study.

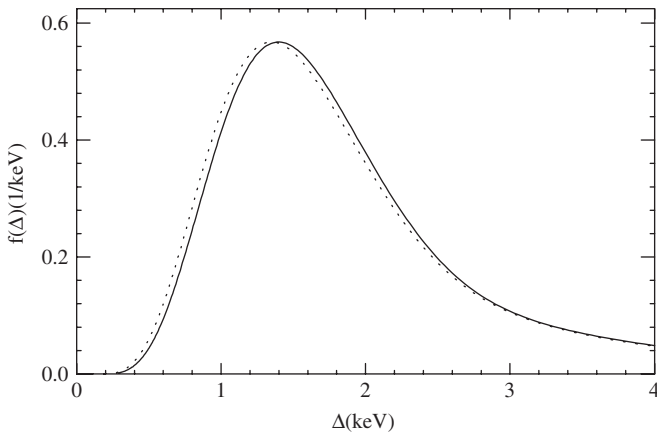


Fig. A.1. Straggling functions $f(\Delta)$ for particles with $\beta\gamma = 4$ traversing $x = 8\ \mu\text{m}$ of Si. The dotted line is calculated with the Bethe–Fano theory of Section 2.2, the solid line with FVP (Section 2.3). The values of the most probable energy losses are ${}_B\Delta_p = 1.349\ \text{keV}$ and ${}_F\Delta_p = 1.398\ \text{keV}$, of the FWHM ${}_Bw = 1.396\ \text{keV}$ and ${}_Fw = 1.380\ \text{keV}$.

Table B.1

Comparison of most probable energy losses Δ_p and FWHM w and their ratios $r_p = \Delta_p(\text{Ar})/\Delta_p(\text{P10})$ and r_w for segments $x = 12\ \text{mm}$

$\beta\gamma$	$\Delta_p(\text{Ar})$	$\Delta_p(\text{P10})$	r_p	$w(\text{Ar})$	$w(\text{P10})$	r_w
0.422	7.9487	7.4933	1.0608	4.9064	4.7023	1.0434
0.596	4.5785	4.3032	1.0640	3.1780	3.0752	1.0334
0.841	2.8778	2.6903	1.0697	2.3190	2.2527	1.0294
1.189	2.0323	1.8870	1.0770	1.8624	1.8085	1.0298
1.679	1.6306	1.5042	1.0840	1.6300	1.5845	1.0287
2.371	1.4603	1.3378	1.0916	1.5300	1.4855	1.0300
3.350	1.4104	1.2882	1.0949	1.5004	1.4558	1.0306
4.732	1.4255	1.3018	1.0950	1.5072	1.4646	1.0291
6.683	1.4742	1.3492	1.0926	1.5326	1.4928	1.0267
9.441	1.5399	1.4135	1.0894	1.5677	1.5297	1.0248
13.335	1.6139	1.4855	1.0864	1.6079	1.5701	1.0241
18.836	1.6919	1.5603	1.0843	1.6507	1.6119	1.0241
26.607	1.7708	1.6354	1.0828	1.6945	1.6541	1.0244
37.584	1.8485	1.7103	1.0808	1.7382	1.6964	1.0246
53.088	1.9204	1.7804	1.0786	1.7812	1.7384	1.0246

The gas densities used are $\rho(\text{Ar}) = 1.6607\ \text{mg/cm}^3$, $\rho(\text{P10}) = 1.5616\ \text{mg/cm}^3$, with a ratio of 1.0635. The values of r_p are slightly larger than the ratio of the gas densities, while r_w is smaller.

Table B.2

Comparison of average values $\langle C \rangle$ of truncated mean energy losses C_A for Ar and C_P for P10, Eq. (32) and the σ , Eq. (33), for tracks with $t = 78.4\ \text{cm}$

$\beta\gamma$	$\langle C \rangle_A$	$\langle C \rangle_P$	r_p	σ_A	σ_P	r_σ
1.146	1.8659	1.8104	1.0307	0.0634	0.0623	1.0177
1.433	1.5883	1.5411	1.0306	0.0657	0.0646	1.0170
1.720	1.4449	1.4020	1.0306	0.0669	0.0658	1.0167
2.006	1.3653	1.3246	1.0307	0.0683	0.0671	1.0179
2.293	1.3177	1.2782	1.0309	0.0686	0.0675	1.0163
2.866	1.2741	1.2357	1.0311	0.0689	0.0677	1.0177
3.582	1.2615	1.2231	1.0314	0.0692	0.0680	1.0176
4.299	1.2648	1.2259	1.0317	0.0689	0.0677	1.0177
6.449	1.3029	1.2622	1.0322	0.0675	0.0664	1.0166
7.165	1.3169	1.2755	1.0325	0.0677	0.0666	1.0165

The ratios r of the two values are given. Both r_p and r_w are smaller than the ratio of the gas densities.

Comparisons for $78.4\ \text{cm}$ tracks are given in Table B.2. Variations in r are less than 1% . The differences in the r between Tables B.1 and B.2 are related to the truncations for C . There is no obvious method to derive one from the other.

An explanation for the systematic trends in r_p and w in the tables could probably be found from the trends seen in Appendix G: the Poisson coefficient m_c , Eq. (18), changes with $\beta\gamma$.

Appendix C. Sources of optical absorption data for Ne, Ar, CH₄, P10 and solids

The photoionization cross-section [95] commonly used for FVP for Ar is given in Ref. [16, Fig. 1.4] and by the solid line in Fig. C.1 (“old data set”). New data

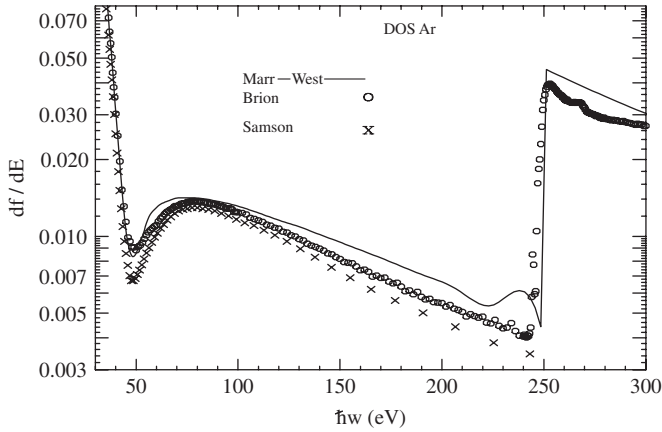


Fig. C.1. Comparison of photo absorption cross-sections for Ar. The photon energy is represented by the angular frequency ω . Solid line from Marr and West [95], \circ from Chan et al. [96], \times from Samson and Stolte [97]. Structures below 200 eV are due to the M-shell, the L-shell excitation begins at 250 eV, the K-shell excitation begins at 3.2 keV [52].

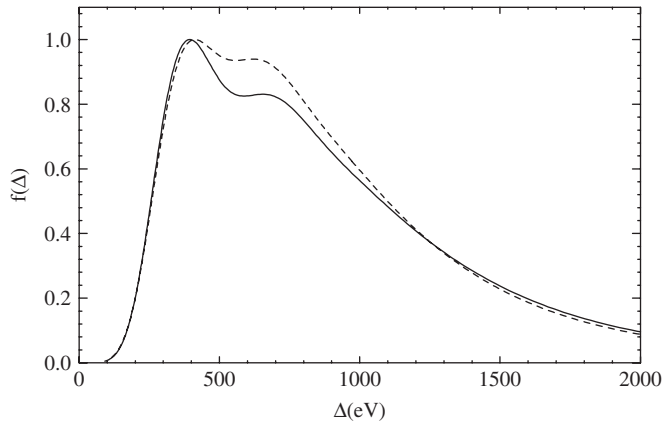


Fig. C.2. Straggling functions calculated with old (dashed line) and new (solid line) df/dE in Ar, for particles with $\beta\gamma = 4.3$ passing through a $x = 6$ mm segment. The functions are matched at Δ_p . Values of Δ_p are 0.416 and 0.392 keV, values of w are 0.844 and 0.772 keV. The differences (-6% and -9%) are much larger than those for Σ_t and M_1 .

from [52,97] are shown by the symbols. Calculations of straggling functions have been made with the old data set and a new set which is a composite of the new data [26]. The changes in $dE/dx = M_1$ for the two sets are small: for 2 GeV protons the values are $M_1 = 1.5405 \text{ MeV cm}^2/\text{g}$ for the old set, $1.5166 \text{ MeV cm}^2/\text{g}$ for the new set. They can be compared to $dE/dx = 1.521 \text{ MeV cm}^2/\text{g}$ from ICRU-49 [40]. The values of Σ_t differ by 3.5%. For the straggling functions shown in Figs. C.2 and C.3 the differences in Δ_p are 6% and in w they are 9% and 2%.

Data for Ne and methane were obtained from the same sources. The optical data for $h\nu < 100$ eV are important for thin absorbers, thus X-ray data tables [76] may not be sufficiently accurate. Data for solids may be found in Refs. [49,94]. Data tables [26] of df/dE are used rather than the polynomials described e.g. in Ref. [53].

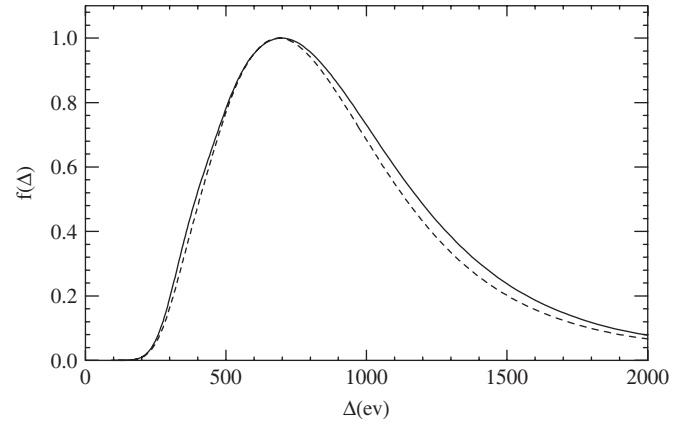


Fig. C.3. Same as Fig. C.2, but for $x = 12$ mm. Values of Δ_p are 1.416 and 1.342 keV, for w they are 1.499 and 1.526 keV. The increase in w is related to the changes in shape seen in Fig. G.2.

Appendix D. Corrections to calculations and data analysis

The inclusion of the Fano and multiplication fluctuations described in Section 10 results in a broadening of the straggling functions $f(\Delta)$. An example with the largest contribution ($B_n = 1.0$) given by Eq. (39) is shown in Fig. D.1.

The value and validity of the data analysis given in Section 14 depends on the variance of the corrections described in Section 10 and discussed in detail in Ref. [87]. An evaluation of a large data set for tracks measured during STAR Running Period 4 (2004) for 48 “runs” (usually lasting a few hours) is given in Fig. D.2. The truncated mean C_x for each track ($60 < t < 76$ cm, momentum p) was used. In each run of the order of 300 tracks for each p were measured. The average value $\langle C_x \rangle$ for each p and each run was calculated (this was obtained from the result box of the ROOT graph). In Fig. D.2 these values are shown as a function of the run number. The various symbols correspond to data taken for the pc given on the right side. The RMS values of $\langle C_x \rangle$ averaged for each momentum are $(0.7 \pm 0.2)\%$. Some of the fluctuations may be due to the truncation fluctuations seen in Fig. 21.

For a track in a magnetic field the curvature must be considered in assigning segment lengths. The radius of curvature R (m) for a particle track with momentum pc (GeV) is given by

$$R = 3.34 pc / B \quad (\text{D.1})$$

where B is measured in Tesla. The deflection for a track of length t is Θ (rad) = t/R . For STAR the first pad-row is at a radial distance of 0.6 m from the center of the TPC. With $B = 0.5$ Tesla the segment lengths along a track with $t = 0.8$ m will change by 20% or more for $pc < 0.2$ GeV. This problem must be studied for the data evaluation. As a corrective measure, scaling for segment lengths according to angle might be used.

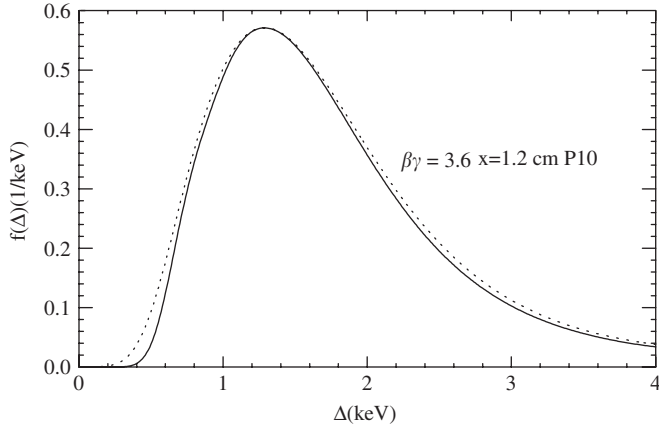


Fig. D.1. Straggling functions with and without Fano and multiplication fluctuations. The solid line is the energy loss spectrum, the dotted line includes the fluctuations. The functions are normalized to the same peak-height. FWHM w increases by about 5.

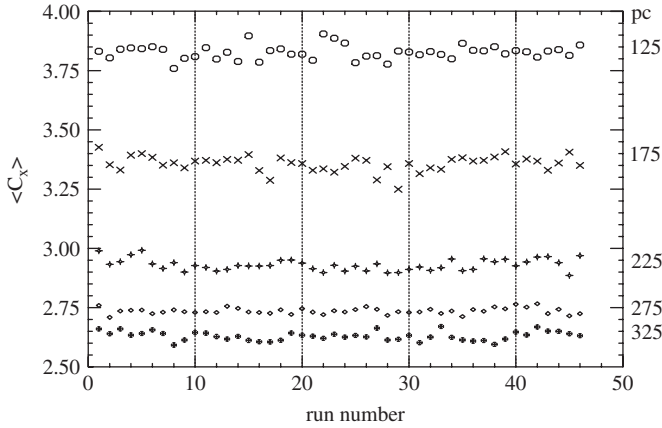


Fig. D.2. Average experimental values $\langle C_x \rangle$ for tracks of length $60 < t < 76$ cm for momentum pc as a function of run number. The symbols correspond to the values of pc (MeV) at right. This shows the quality and stability of the corrections described in Section 10.

In the primary analysis of STAR data with ROOT [91] there were two analytic algorithms which I used to get fits to straggling functions for segments: “Landau function” and “polynomials”. The Landau function never gave a close fit to experimental data, as anticipated from Fig. D.3, but the five parameter polynomials gave a good fit to the upper half of $h(Q)$, i.e. the part of the spectrum which did not include the tails. The “Mean” and “RMS” given in the result box exceeded the most probable value Δ_p and FWHM w by up to 25%, depending on the value of x and the largest Q (= “ dE/dx ” in ROOT) included in the spectra, see Figs. 18 and 19.

Appendix E. Electron ranges and energy deposition in Ar, P10 and Si

The energy deposition by low energy electrons is a complex process [98]. Even for mono-energetic parallel beams of electrons ($T < 50$ keV) the energy deposition

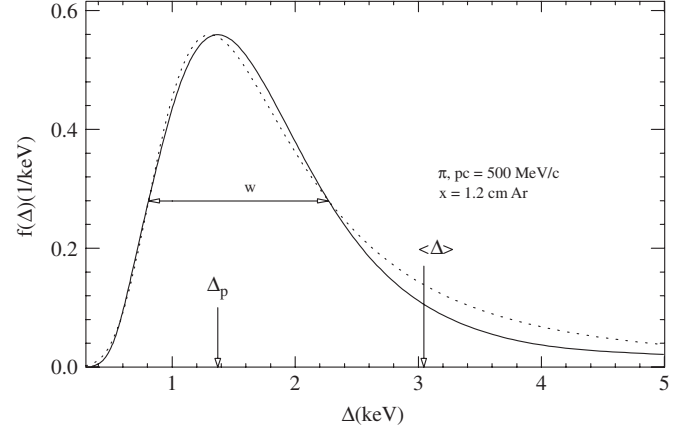


Fig. D.3. The solid line is the straggling function $f(\Delta)$ of Fig. 1, the dotted line is a “Landau function” [2] scaled to have the same width w as $f(\Delta)$ and to coincide at Δ_ℓ . Clearly the attempt to “fit” experimental straggling functions with a Landau function will be an unreliable approximation. Functions available at Ref. [26] could be used instead.

Table E.1

Practical ranges R (cm for gases, μm for Si) of electrons with kinetic energy T in P10 gas, Si and Ne

T (keV)	R (P10)	R_c	R (Ne)	R (Si)
0.1	0.0002	–	0.0003	0.004
0.2	0.0004	–	0.0007	0.008
0.4	0.0010	–	0.0017	0.015
0.7	0.0018	–	0.0030	0.030
1.0	0.0031	–	0.0053	0.04
2.0	0.01	–	0.017	0.10
4.0	0.03	–	0.05	0.24
7.0	0.08	–	0.13	0.55
10	0.14	0.25	0.24	0.96
20	0.42	0.83	0.9	3.0
40	1.5	2.74	2.6	10
70	4.0	7.20	6.7	27
100	7.3	13.1	12	50
200	22	40.4	38	160
400	63	115	112	450
700	136	244	248	960
1000	215	381	396	1520

The density, $\rho = 1.56$ mg/cm³ for the P10 mixture (90% Ar, 10% CH₄), for Ne $\rho = 0.91$ mg/cm³ at 740 torr and 293 K is used. Ranges R_c calculated with CSDA for P10 are also given [39]. For $E > 50$ keV, effective ranges were calculated with the algorithm given in Ref. [99]. For $E < 10$ keV, experimental effective ranges measured for nitrogen [98,100] were assumed to be the same for argon (with an uncertainty of 10%). Between 10 and 50 keV, calculated ranges [99] were reduced smoothly to the experimental value at 10 keV. The uncertainty of R is about 20%.

extends over a spherical volume tangent to the point of entrance into the absorber. The diameter of the sphere is of the order of the “practical range,” considerably smaller than the path-length (“continuous-slown-down-approximation” or CSDA range) calculated with the stopping power. Table E.1 gives practical and CSDA ranges [39]. A useful reference is [99].

Appendix F. Collision cross-sections for electrons and heavy ions

Some particle physicists believe that because there is a difference in the stopping power $S = dT/dx$ for electrons and protons [39,40] there should also be a difference in the straggling functions. For example, for minimum ionizing particles, $\beta\gamma = 3.6$, in P10 gas, we have for pions [40], the kinetic energy $T = 382$ MeV, $E_{\max} = 12.9$ MeV and $dT/dx = 2.431$ MeV/cm, for electrons [39], $T = 1.4$ MeV, $E_{\max} = 0.7$ MeV and $dT/dx = 2.202$ MeV/cm. The explanation for the difference in dT/dx is mostly that the single collision spectrum for pions extends to 13 MeV, that for electrons only to 0.7 MeV.

The single collision spectra are compared in Fig. F.1. For $E < 300$ keV, the difference between the spectra is less than 2%. At $E = 0.7$ MeV, the electron cross-section exceeds the one for pions by a factor of 1.7. The straggling functions for heavy particles and electrons with the same speed in the same segment x will be the same until Δ exceeds E_{\max} of the electrons or until multiple scattering becomes important for electrons. The major reason for this similarity is that the $M_0(\beta\gamma) = \Sigma_t$ are the same.

Appendix G. Straggling functions for very thin absorbers

The structure of the single collision spectra, Figs. 5 and 6, will remain apparent in multiple collisions, as can be seen in Section 4.2, Figs. 11 and 12, and, and in straggling functions for thin absorbers, Figs. 2 and G.1. In straggling spectra (Eq. (20), Section 4.3), where the multiple collision spectra are weighted by the Poisson distribution, the prominent features in $\sigma(E)$, Figs. 2 and G.1, will only disappear for $m_c > 20$ for narrow structures such as the plasmon peak at 17 eV for Si, $m_c > 10$ for the broader peak in Ar and P10. The L-shell peak, e in Figs. G.1 and G.2 is always convoluted with the M-shell peaks, thus shifted to Δ

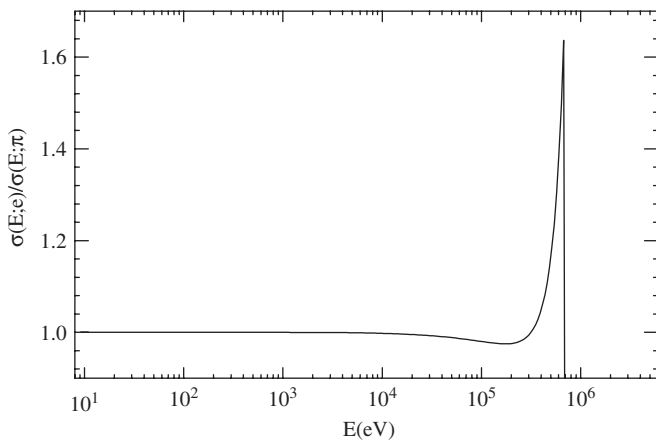


Fig. F.1. Ratio of single collision cross-sections for electrons and pions, with $\beta\gamma = 3.6$ in P10. Differences are: $dT/dx(\pi) = 2.431$ keV/cm, $dT/dx(e) = 2.202$ keV/cm, $\Sigma_t = 29.6911$ and 29.6908 collisions/cm. At $E = 10$ keV, $\sigma(E;e)/\sigma(E;\pi) - 1.0 = -0.3\%$, at 100 keV -2% , at 670 keV the ratio is 1.7. The function is practically the same for Si.

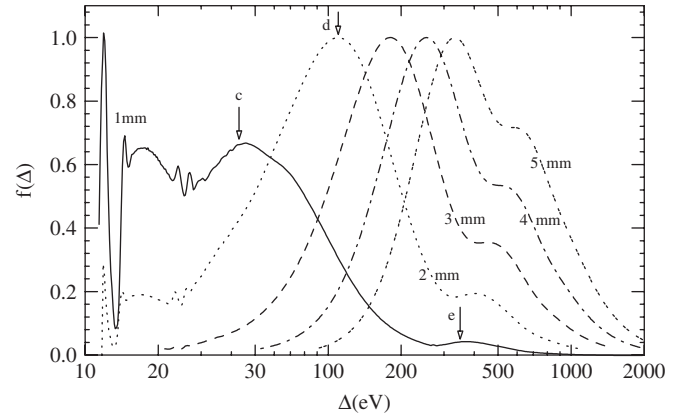


Fig. G.1. Straggling functions for singly charged particles with $\beta\gamma = 4.48$ traversing segments of length $x = 1$ –5 mm in Ar. The total single collision cross-section is 30 collisions/cm. The functions are normalized to 1.0 at the most probable value. The broad peak at 17 eV is due to single collisions, see Fig. 11. For two collisions it broadens and shifts to about 43 eV, marked c , and for $n = 3$ it can be seen at d . It may be noted that the peak at 11.7 eV (if the function is normalized to unit area) is exactly proportional to $m_c^{-m_c}$, as expected from Eq. (20). Energy losses to L-shell electrons of Ar, at 250 eV in Fig. 6, appear at e , for $x = 1$ mm they have an amplitude of 0.04. The δ -function at $\Delta = 0$, $n = 0$, Eq. (20), is not shown. For $x = 1$ mm, it would be $e^{-m_c} = 0.05$. For $x > 2$ mm peak c has disappeared, peak d is the dominant contribution and defines the most probable energy loss Δ_p . The buildup for peak e at 440 to 640 eV is the contribution from L-shell collisions. It appears roughly at 250 eV plus Δ_p . The total cross-section for collisions with $E > 250$ eV is only 1.7 collisions/cm, thus the amplitude of the peak e is roughly proportional to x . The Bethe–Bloch mean energy loss is 250 eV/mm.

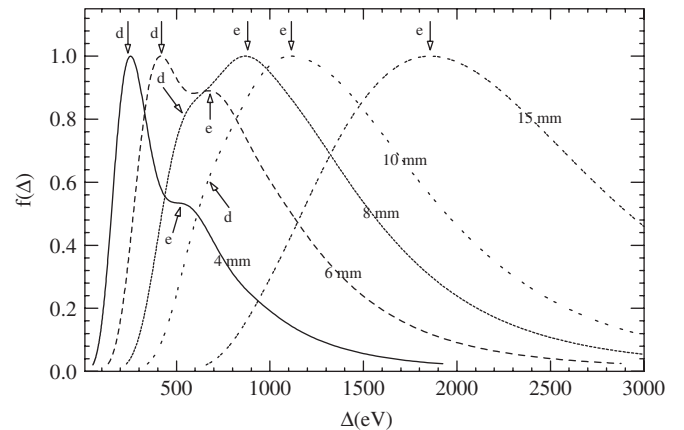


Fig. G.2. Similar to Fig. G.1, but for $x = 4$ –15 mm. Peak d is still dominant for $x = 4$ and 6 mm, but peak e due to L-shell collisions increases. It becomes the dominant feature at $x \geq 8$ mm, with a shift of the most probable energy loss Δ_p from 400 to 850 eV, see Fig. 15. A shoulder of peak d , for multiple collisions for $E < 40$ eV remains, and is just perceptible at $x = 10$ mm. For $x = 15$ mm, the peaks have merged and the straggling function has reached the Vavilov shape, but not its location and FWHM. The Bethe–Bloch mean energy loss is $250 \times x(\text{mm})$ eV.

larger than the L-shell ionization energy, $E_L = 250$ eV. About two collisions are needed to broaden it and merge it with the convolution of the M-shell peak d in Fig. G.2.

It would be interesting to see whether the structures can be discerned in experimental data, but see [73]. Collisions

with the K-shell electrons in P10 have a mean free path $\lambda_K \sim 28$ cm, but will influence the spectra very little, see Fig. 42. For Ne the presence of K-shell energy losses can be seen in Figs. 19 and J.3. The situation for Si is similar, see Ref. [28, Fig. 91.6]. A calculation for $1 \mu\text{m}$ is shown in Fig. 2. These effects usually cannot be measured with ionization chambers (but see Ref. [73,81]). They have been seen with energy loss measurements in e.g. electron microscopes [6,94].

Appendix H. Gas multiplication

Detailed discussions of ionization amplification can be found in Refs. [16,22]. The reader is urged to study at least one of these books in detail. The evaluation of measurements described here was made in 2002. I assumed then that the effects of diffusion described in Section 10 were negligible and that the effects found here were related mainly to gas multiplication. The problem of the distortion of $G(J)$ relative to $f(\Delta)$ by the small number of electrons produced in $x = 1.284$ cm segments (56 electrons at Δ_p) has not been explored. Also the electrons are collected over several pads and the signal on some may be below threshold.

About gas multiplication two aspects may be influential

- the proportionality of ionization J and ADC output Q ,
- changes of the shape of $g(J)$ into $H(J')$ and $h(Q)$ due to the multiplication variance.

The other effects described in Section 10 may also influence these data, and they should be considered as an inducement for more careful studies of the effects seen in Table H.1.

The sum of these effects as determined with data from the STAR TPC [90], is shown in Table H.1. No simple relations are seen except that the 50% change in w_x/Q_p with x is related to the narrowing of the Poisson distribution with increasing number of collisions. The 10% change in Q_p/Δ_p and in r_w with x could be caused by a non-proportionality of J and Q . Studies of these effects for ALICE test TPC have been made by Christiansen at ALICE [74].

Table H.1

Comparison at $\beta\gamma = 3.6$ of most probable ADC output Q_p to calculated most probable energy loss Δ_p and FWHM w_x and w for several segment lengths

x (cm)	Q_p/x	Δ_p/x	Q_p/Δ_p	w_x/Q_p	w/Δ_p	r_w (%)
1.284	1.849	1.190	1.554	1.050	1.024	2.5
2.117	1.912	1.305	1.465	0.804	0.804	0.0
3.004	1.996	1.369	1.458	0.760	0.694	9.5
4.055	2.014	1.417	1.421	0.686	0.625	9.8

The ratio Q_p/Δ_p is greater than 1.0 because of the choice of the calibration of the TPC with the BB dE/dx . The ratio $r_w = (w_x/Q_p)/(w/\Delta_p)$ is also given. It should be constant.

Appendix I. Bremsstrahlung

For thin detectors bremsstrahlung will rarely be seen. This is shown here on the basis of the description given by Evans [78]. The differential cross-section for production of Bremsstrahlung of energy E by electrons with kinetic energy T is given by

$$d\sigma_{\text{rad}} = \alpha r_0^2 B Z^2 \frac{T + m_0 c^2}{T} (dE/E) \text{ cm}^2/\text{nucleus}. \quad (\text{I.1})$$

Using the approximation $B = 18$ results in 2.0×10^{-24} $(dE/E) \text{ cm}^2/\text{nucleus}$ for Si or $d\sigma_{\text{rad}} = 0.10 (dE/E)/\text{cm}$, for Ar $d\sigma_{\text{rad}} \sim 10^{-4} (dE/E)/\text{cm}$. For Si the moments are $M_0(E_u) = 0.10 \cdot \ln(E_u/E_l)/\text{cm}$ where E_u is an upper energy under consideration, or if the full spectrum is to be considered, $E_u = T$. The lower limit E_l could be chosen e.g. as 1.1 eV (the bandgap of Si), in which case $M_0(1000 \text{ MeV}) \sim 2/\text{cm}$. For M_1 we get $M_1(E_u) = 0.102 \cdot (E_u - E_l) \text{ MeV}/\text{cm}$, and for $E_u = 1000 \text{ MeV}$, $M_1(1000 \text{ MeV}) = 102 \text{ MeV}/\text{cm}$, which is close to the value of 105 MeV/cm given in Ref. [39]. Note that the mean energy loss per photon is $100 \text{ MeV}/2 = 50 \text{ MeV}$. Clearly, in the usual $300 \mu\text{m}$ Si detectors ($\Delta_p \sim 80 \text{ keV}$), the probability of the production of any Bremsstrahlung photon is on the average only 0.06. For the production of photons with energy within the practical extent of $f(\Delta)$ ($60 < E(\text{keV}) < 120$, Fig. 34) it is 0.002. For small arrays of Si detectors, the “radiative stopping power” is a meaningless quantity, even if it is 20 times the electronic stopping power.

Pair production and photo nuclear loss which also contribute to dE/dx at $\beta\gamma > 500$ are described in Ref. [38]. For large arrays of Si detectors, e.g. GLAST, the effects must be considered.

Appendix J. ALICE TPC Monte Carlo method

In creating a program to calculate straggling functions for segments (Section 4.3 or 4.4), two functions are needed:

- the function describing the number of collisions per unit track length, such as $\Sigma_t(\beta\gamma) = M_0(\beta\gamma)$ shown in Figs. 24 and 25,
- the differential single collision cross-section $\sigma(\beta\gamma)$ shown in Figs. 5 and 6.

If *approximations* for these functions are chosen for simulations, the results should be compared with the results obtained with the above functions in order to assess the effect of the approximations.

As an example examine the procedure suggested for the Monte Carlo calculation of straggling functions for the ALICE TPC, described in Ref. [23, Section 7.2.1.1]. For the first function $\Sigma_t(\beta\gamma)$ two pieces of information are given: the first by Fig. 7.1 of [23], which corresponds to the Poisson distribution of Eq. (18) in Section 4.1. Its mean is given as $m_c/x = \Sigma_t \sim 15$ collisions/cm at $\beta\gamma \sim 3.6$. The

second piece is supposed to represent $\Sigma_t(\beta\gamma)/\Sigma_t(3.6)$ and is given in Fig. 7.2 in Ref. [23]. It is approximated by the function [16]

$$f(\beta\gamma) = \frac{P_1}{\beta^{P_4}} \left\{ P_2 - \beta^{P_4} - \ln \left[P_3 + \frac{1}{(\beta\gamma)^{P_5}} \right] \right\} \quad (J.1)$$

called the “Bethe–Bloch curve” in Ref. [23] with the value 1.0 at $\beta\gamma \sim 3.6$. It is given in Fig. J.1 and is the same function as that shown in Fig. 57. It differs *conceptually* from $\Sigma_t(\beta\gamma)$ because Eq. (J.1) was determined from experimental measurements of average values $\langle C \rangle$ for tracks. It also differs from the Bethe–Bloch function $M_1(\beta\gamma) = dE/dx(\beta\gamma)$.

In Ref. [23] the differential single collision cross-section is approximated by a modified Rutherford cross-section (Eq. (1)): the function κE^{-2} is replaced by $\kappa E^{-2.2}$ and κ is chosen to make the integral $\Sigma_t(\beta\gamma) = \int \kappa E^{-2.2} dE \sim 15/\text{cm}$ equal to the value given for Fig. 7.1 of [23]. This function is compared to the $\sigma(E)$ calculated with FVP theory (Eq. (7)) for Ne in Fig. J.2.

Monte Carlo calculations of straggling functions with the model of Ref. [23] are compared to the analytic calculation with $\sigma(E)$ in Fig. J.3. The differences seen are explained by the differences in the CCS. Predominant is the excess of $\sigma(E)$ over the approximation function for $30 < E(\text{eV}) < 300$ resulting in the shift to greater Δ of the analytic function. In addition the K-shell energy losses between 1.7 and 2.4 keV do not appear in the MC calculation, also see Fig. 19.

No major changes are needed for the simulations with AliRoot Monte Carlo with the proposed model:

- The function $f(\beta\gamma)$, Eq. (J.1), should be replaced by $\Sigma_t[\text{Ne}]$ of Fig. J.1 [26], for which an analytic function could readily be made.

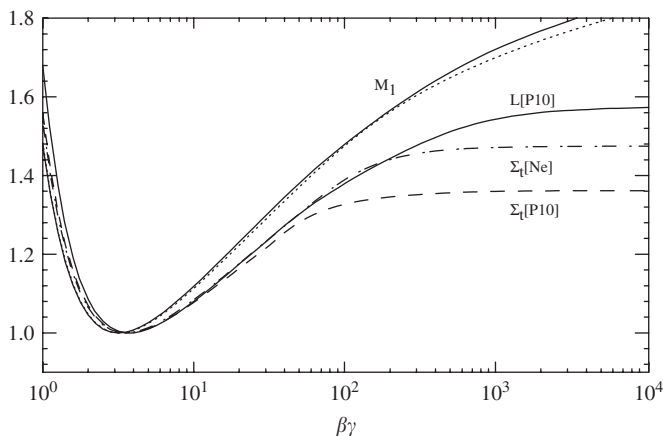


Fig. J.1. The dependence on $\beta\gamma$ of $\Sigma_t(v)$ in Ne and P10 gas. The Bethe–Bloch functions $M_1(v)$ are also given (dotted line for Ne). The function given by Eq. (J.1) is given by the solid line labeled L[P10]. All functions are normalized to 1.0 at minimum ionization. The function ${}_R M_0$ (Eq. (23)) for the Rutherford type cross-section is a horizontal line 1.0. For $\beta\gamma < 3$ they will follow the functions shown, then they will be horizontal lines at 1.0. The FVP $dE/dx = M_1$ differ little for the two gases, but $\Sigma_t[\text{Ne}]$ reaches saturation at a higher value than $\Sigma_t[\text{P10}]$.

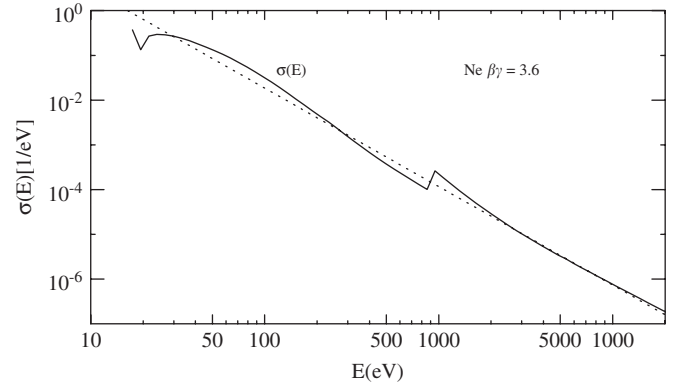


Fig. J.2. Inelastic collision cross-section $\sigma(E; \beta\gamma)$ for single collisions in ALICE Ne gas by ionizing particles with $\beta\gamma = 3.6$, calculated with FVP theory (Eq. (7)): solid line. The modified Rutherford cross-section is given by the dotted line. Its coefficient is chosen to give the same value of $\Sigma_t(\beta\gamma)$ as obtained with $\sigma(E; 3.6)$.

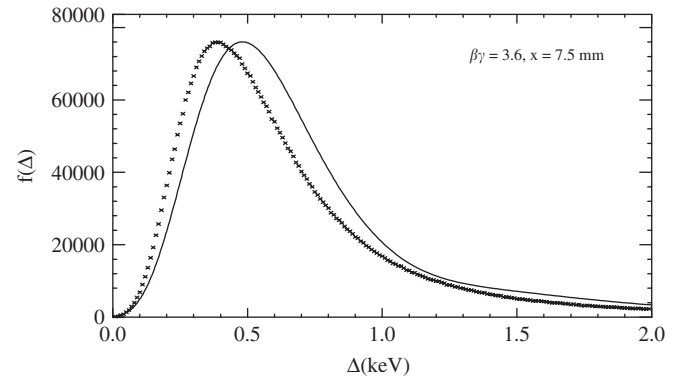


Fig. J.3. Straggling functions for particles with $\beta\gamma = 3.6$ traversing Ne segments with $x = 7.5$ mm. Solid line: analytic FVP calculation, $\Sigma_t = 13.2$ collisions/cm. Monte Carlo calculation with the ALICE TPC algorithm, with the CCS of Fig. J.2, $\Sigma_t = 15/\text{cm}$. The function is shown by \times . Even though the Σ_t are practically the same, the MC calculation has a smaller Δ_p . The difference in the shape of the curves corresponds to the difference in the CCS seen in Fig. J.2.

- For the energy losses in single collisions use the *inverted energy loss spectrum for 10 values of bq* in Ref. [26].

A single analytic expression for these functions would result in errors of the order of 10% in FWHM.

References

- [1] S. Eidelman, et al., Phys. Lett. B 592 (2004) 1. (<http://pdg.lbl.gov>).
- [2] W. Börsch-Supan, J. Res. Nat. Bur. Stand.—B 65B (1961) 245.
- [3] B. Rossi, High-Energy Particles, Prentice-Hall, Inc., Englewood Cliffs, NJ, 1952.
- [4] E.J. Williams, Proc. Roy. Soc. A 125 (1929) 420.
- [5] H. Bichsel, R.P. Saxon, Phys. Rev. A 11 (1975) 1286.
- [6] J.Ph. Perez, J. Sevely, B. Jouffrey, Phys. Rev. A 16 (1977) 1061.
- [7] H.W. Lewis, Phys. Rev. 125 (1962) 937.
- [8] F.S. Goulding, D.A. Landis, J. Cerny, R.H. Pehl, Nucl. Instr. and Meth. 31 (1964) 1.

- [9] H. Bichsel, Nucl. Instr. and Meth. 78 (1970) 277.
- [10] W.W.M. Allison, J.H. Cobb, Ann. Rev. Nucl. Part. Sci. 30 (1980) 253.
- [11] M. Anderson, et al., Nucl. Instr. and Meth. A 499 (2003) 659.
- [12] K.H. Ackerman, et al., Nucl. Instr. and Meth. A 499 (2003) 624.
- [13] M. Anderson, et al., Nucl. Instr. and Meth. A 499 (2003) 679.
- [14] M. Brigida, et al., Nucl. Instr. and Meth. A 533 (2004) 322.
- [15] H. Bichsel, Phys. Rev. A 9 (1974) 571.
- [16] W. Blum, L. Rolandi, Particle Detection with Drift Chambers, Springer, Berlin, 1994 (second printing).
- [17] L. Landau, J. Phys. VIII (1944) 201.
- [18] H. Bichsel, Rev. Mod. Phys. 60 (1988) 663.
- [19] A. Rubach, H. Bichsel, Phys. Med. Biol. 27 (1982) 893.
- [20] H. Bichsel, Monte Carlo calculation of energy deposition by fast protons in a Rossi Counter, Proceedings of the Ninth Symposium on Microdosimetry, May 1985, Radiation Protection Dosimetry, vol. 13, 1985, p. 91.
- [21] P.H. Heintz, M.A. Robkin, H. Bichsel, Health Phys. 21 (1971) 598.
- [22] G.F. Knoll, Radiation Detection and Measurement, third ed., Wiley, New York, 2000.
- [23] ALICE Technical Design Report of the Time Projection Chamber, CER/LHCC 2000-001, ALICE TDR 7 (7 January 2000) and ALICE-INT-2005-030.
- [24] P. Glaessel, J. Phys. G 30 (2004) S1083.
- [25] H.G. Fischer, CERN, private communications, 2001.
- [26] Data and functions are given at (<http://faculty.washington.edu/hbichsel>) and (<http://www.star.bnl.gov/~bichsel/>).
- [27] J.F. Bak, et al., Nucl. Phys. B 288 (1987) 681.
- [28] H. Bichsel, Particle-matter interactions, in: G. Drake (Ed.), Atomic, Molecular and Optical Physics Handbook, Springer, Berlin, 2005 (Chapter 91).
- [29] H. Bichsel, Nucl. Instr. and Meth. B 52 (1990) 136.
- [30] Results have been given in H. Bichsel, Annual Reports, Nuclear Physics Laboratory, University of Washington, 1993–2005.
- [31] ICRU report 31, Average energy required to produce an ion pair, International Commission on Radiation Units, 7910 Woodmont Avenue, Washington, DC, 20014, 1979.
- [32] E. Fermi, Z. Phys. 29 (1924) 3157; E. Fermi, Nuovo Cimento 2 (1925) 143.
- [33] N. Bohr, Dan. Mat. Fys. Medd. 18 (8) (1948) (ed.2,1953).
- [34] U. Fano, Ann. Rev. Nucl. Sci. 13 (1963) 1.
- [35] Energy losses of electrons below 10 keV. H. Bichsel, Eighth Pfefferkorn Conference, Park City, May 1989, Scanning Microscopy Supplement, Scanning Microscopy International, AMF O'Hare, Chicago.
- [36] ICRU Report 55, Secondary electron spectra from charged particle interactions, International Commission on Radiation Units and Measurements, 7910 Woodmont Avenue, Washington, DC, 20014, 1996.
- [37] P.V. Vavilov, Sov. Phys. JETP 5 (1957) 749.
- [38] D.E. Groom, N.V. Mokov, S.I. Striganoff, At. Data Nucl. Data Tables 78 (2001) 183.
- [39] ICRU Report 37, Stopping powers for electrons and positrons, International Commission on Radiation Units and Measurements, 7910 Woodmont Avenue, Washington, DC 20014, 1984.
- [40] ICRU Report 49, Stopping power and ranges for protons and alpha particles, International Commission on Radiation Units and Measurements, 7910 Woodmont Avenue, Washington, DC, 20014, 1993.
- [41] O. Blunck, S. Leisegang, Z. Phys. 128 (1950) 500.
- [42] P. Shulek, B.M. Golovin, L.A. Kulyukina, S.V. Medved, P. Pavlovich, J. Nucl. Phys. 4 (1967) 400.
- [43] R. Talman, Nucl. Instr. and Meth. 159 (1979) 189.
- [44] H. Bethe, Ann. Phys. 5 (1930) 325.
- [45] M. Inokuti, Rev. Mod. Phys. 43 (1971) 297; M. Inokuti, Rev. Mod. Phys. 50 (1978) 23.
- [46] H. Bichsel, Phys. Rev. A 65 (2002) 052709.
- [47] D. Liljequist, J. Phys. D 16 (1983) 1567.
- [48] J.W. Gallagher, C.E. Brion, J.A.R. Samson, P.W. Langhoff, J. Phys. Chem. Ref. Data 17 (1988) 9.
- [49] E.D. Palik (Ed.), Handbook of Optical Constants of Solids, Academic Press, New York, 1997.
- [50] H. Raether, Excitation of Plasmons and Interband Transitions by Electrons, Springer, New York, 1980.
- [51] U. Fano, J.W. Cooper, Rev. Mod. Phys. 40 (1968) 441.
- [52] J. Berkowitz, Atomic and Molecular Photo Absorption, Academic Press (A division of Harcourt) 2002.
- [53] J. Apostolakis, et al., Nucl. Instr. and Meth. A 453 (2000) 597.
- [54] H. Bichsel, Phys. Rev. B 1 (1970) 2854.
- [55] H. Bichsel, Phys. Rev. A 46 (1992) 5761.
- [56] H. Bichsel, Passage of Charged Particles through Matter, American Institute of Physics Handbook, Section 8d, third ed., McGraw-Hill, New York, 1972.
- [57] P. Sigmund, U. Haagerup, Phys. Rev. A 34 (1986) 892.
- [58] C. Tschalär, Nucl. Instr. and Meth. 61 (1968) 141.
- [59] B.L. Jhanwar, Wm.J. Meath, J.C.F. MacDonald, Radiat. Res. 96 (1983) 20.
- [60] E. Shiles, T. Sasaki, M. Inokuti, D.Y. Smith, Phys. Rev. B 22 (1980) 1612.
- [61] H. Bichsel, R.F. Mozley, W. Aron, Phys. Rev. 105 (1957) 1788.
- [62] H. Bichsel, R.F. Mozley, Phys. Rev. 94 (1954) 764(A).
- [63] S. Agostinelli, et al., Nucl. Instr. and Meth. A 506 (2003) 250.
- [64] J. Va'vra, Nucl. Instr. and Meth. A 453 (2000) 262.
- [65] O. Blunck, K. Westphal, Z. Phys. 130 (1951) 641.
- [66] K.A. Ispirian, A.T. Margarian, A.M. Zverev, Nucl. Instr. and Meth. 117 (1974) 125.
- [67] Y. Fisyak, BNL, private communications, 2000–2005.
- [68] N.L. Johnson, Biometrika 36 (1949) 149.
- [69] I. Lehraus, R. Matthewson, W. Tejessy, IEEE Trans. Nucl. Sci. NS-30 (1983) 50.
- [70] R.M. Sternheimer, R.F. Peierls, Phys. Rev. B 3 (1971) 3681.
- [71] H. Bichsel, Comparison of Bethe–Bloch and Bichsel functions, STAR Note SN 0439 (3.3.2002). (<http://www.star.bnl.gov/Notes>).
- [72] A.H. Walenta, J. Fischer, H. Okuno, C.L. Wang, Nucl. Instr. and Meth. 161 (1979) 45.
- [73] H. Bichsel, Adv. Quantum Chem. 46 (2004) 329.
- [74] ALICE TPC, P. Christiansen, CERN, see (<http://alicetpctest.web.cern.ch/alicetpctest/bichsel/>).
- [75] Wm.H. Press, et al., Numerical Recipes, Cambridge University Press, Cambridge, 1986.
- [76] E.B. Saloman, J.H. Hubbell, X ray Attenuation Coefficients, NBSIR 86-3431, NBS (now NIST) July 1986.
- [77] W. Bambynek, et al., Rev. Mod. Phys. 44 (1972) 716.
- [78] R.D. Evans, The Atomic Nucleus, McGraw-Hill, New York, 1967 (eleventh printing).
- [79] F. Lapique, F. Piuz, Nucl. Instr. and Meth. 175 (1980) 297.
- [80] R. Bossingham, TPC: Algorithms, gain and R- ϕ resolution with P10, STAR Note 247. Available at: (<http://www.star.bnl.gov>).
- [81] IAEA-TECDOC-799, Atomic and molecular data for radiotherapy and radiation research, Final report of a co-ordinated research programme, IAEA Vienna, May 1995.
- [82] D. Combecher, Radiat. Res. 84 (1980) 189.
- [83] R.C. Alig, Phys. Rev. B 27 (1983) 968.
- [84] M. Winter, private communication, Zürich, October 2005.
- [85] W.B. Atwood, et al., Nucl. Instr. and Meth. A 306 (1991) 446.
- [86] J. Abele, et al., Nucl. Instr. and Meth. A 499 (2003) 692.
- [87] A. Tang, Elliptic flow in Au + Au collisions., Dissertation, Kent State University, May 2002. Available at: (<http://www.star.bnl.gov/central/publications/thesis>).
- [88] F. Harris, et al., Nucl. Instr. and Meth. 107 (1973) 413.
- [89] H. Bichsel, “Resolution” in particle identification with TPC, STAR Note SN 0441 (31.8.2002).
- [90] H. Bichsel, Theory of Particle Identification (PID) for TPCs, Poster presented at Quark Matter 2002, Nantes, June 2002.

- [91] R. Brun, F. Rademacher, Nucl. Instr. and Meth. A 389 (1997) 81 (See also (<http://root.cern.ch>)).
- [92] H. Bichsel, Calculated and experimental Landau spectra in a TPC, STAR Note SN 0440 (24.6.2002).
- [93] I. Lehrs, R. Matthewson, W. Tejessy, Nucl. Instr. and Meth. 196 (1982) 361.
- [94] C.C. Ahn, O.L. Krivanek, EELS Atlas, GATAN Inc., 780 Commonwealth Drive, Warrendale PA 15086, 1983.
- [95] G.V. Marr, J.B. West, At. Data Nucl. Data Tables 18 (1976) 497.
- [96] W.F. Chan, G. Cooper, C.E. Brion, Chem. Phys. 168 (1992) 375.
- [97] J.A.R. Samson, W.C. Stolte, J. Electron Spectrosc. Relat. Phenom. 122 (2002) 265.
- [98] E. Waibel, B. Grosswendt, Stopping power and energy range relation for low energy electrons in nitrogen and methane, 7th Symposium on Microdosimetry, 8–12 September 1980, Oxford/UK EUR 7147 (Commission of European Communities).
- [99] E.J. Kobetich, R. Katz, Phys. Rev. 170 (1968) 391.
- [100] B.G.R. Smith, J. Booz, Experimental results on W-values and transmission of low energy electrons in gases, 6th Symposium on Microdosimetry, Brussels, Belgium, May 22–26, 1978, EUR 6064 (Commission of European Communities).